

Air Force Institute of Technology

**AFIT Scholar**

---

Theses and Dissertations

Student Graduate Works

---

3-1998

## Forecasting Wet Microbursts Associated with Summertime Airmass Thunderstorms over the Southeastern United States

James B. Mackey

Follow this and additional works at: <https://scholar.afit.edu/etd>



Part of the [Meteorology Commons](#)

---

### Recommended Citation

Mackey, James B., "Forecasting Wet Microbursts Associated with Summertime Airmass Thunderstorms over the Southeastern United States" (1998). *Theses and Dissertations*. 5705.

<https://scholar.afit.edu/etd/5705>

This Thesis is brought to you for free and open access by the Student Graduate Works at AFIT Scholar. It has been accepted for inclusion in Theses and Dissertations by an authorized administrator of AFIT Scholar. For more information, please contact [AFIT.ENWL.Repository@us.af.mil](mailto:AFIT.ENWL.Repository@us.af.mil).

**FORECASTING WET MICROBURSTS ASSOCIATED  
WITH SUMMERTIME AIRMASS THUNDERSTORMS  
OVER THE SOUTHEASTERN UNITED STATES**

**THESIS**

**James Bryan Mackey, Captain, USAF**

**AFIT/GM/ENP/98M-06**

19980409046

AFIT/GM/ENP/98M-06

**FORECASTING WET MICROBURSTS ASSOCIATED WITH SUMMERTIME AIRMASS  
THUNDERSTORMS OVER THE SOUTHEASTERN UNITED STATES**

**THESIS**

**Presented to the Faculty of the Graduate School of Engineering of the**

**Air Force Institute of Technology**

**Air University**

**Air Education and Training Command**

**In Partial Fulfillment of the Requirements for the**

**Degree of Master of Science in Meteorology**

**James Bryan Mackey, B.S.**

**Captain, USAF**

**March 1998**

**Approved for public release, distribution unlimited**

**The views expressed in this thesis are those of the author and do not reflect the official policy or position of the Department of Defense or the U. S. Government**

AFIT/GM/ENP/98M-06


FORECASTING WET MICROBURSTS ASSOCIATED WITH SUMMERTIME AIRMASS  
THUNDERSTORMS OVER THE SOUTHEASTERN UNITED STATES

James Bryan Mackey, B.S.  
Captain, USAF


Approved:

 Askue  
Lt Col Cecilia A. Askue  
Chair, Advisory Committee

25 Feb 98  
date

 Dungey  
Maj Clifton E. Dungey  
Member, Advisory Committee

4 Mar 98  
date

 Reynolds  
Professor Daniel E. Reynolds  
Member, Advisory Committee

3 March 98  
date

 Trell  
Dr. Jason P. Trell  
Member, Advisory Committee

28 Feb 98  
date

## Acknowledgments

I would like to express my sincere appreciation to my advisors, Lt Col Cecilia Askue and Dr. Jason Tuell, for all their insights, support, and input throughout this research. I greatly appreciate the knowledge and ideas you have given me. I would like to thank Maj Dungey for his inputs regarding radar issues. I would also like to thank Professor Reynolds for contributing his expertise in statistics to this research effort; we all learned a tremendous amount from your classes. I am also grateful to the folks at AETC AOS/AOW for your inputs and questions.

I am also extremely grateful to MSgt Pete Rahe for his never-ending efforts to keep the workstations alive and the hard drives available. Your devotion and willingness to take the extra time to make sure all was well went a long way.

Most importantly, I wish to express my sincere appreciation to my wife, Sonja, and my daughters, Kalyn and Ryan. Your patience, love, support, and sacrifice have allowed me to devote myself to this endeavor and see it through. Without your understanding this project would not have been possible.

James Bryan Mackey

## Table of Contents

	Page
Acknowledgments . . . . .	ii
List of Figures . . . . .	vii
List of Tables . . . . .	ix
Abstract . . . . .	x
I. Introduction . . . . .	1
1.1 Background . . . . .	1
1.2 Problem Statement . . . . .	4
1.3 Importance of Research . . . . .	4
1.3.1 Aircraft Performance During a Wet Microburst . . . . .	5
1.3.2 Illustrative Example . . . . .	6
1.4 Objectives . . . . .	7
1.5 Overall Approach . . . . .	8
1.6 Summary of Results . . . . .	9
1.7 Organizational Overview . . . . .	9
II. Literature Review . . . . .	10
2.1 NIMROD . . . . .	10
2.2 JAWS . . . . .	10
2.3 Results of NIMROD and JAWS . . . . .	11
2.4 MIST . . . . .	12
2.5 Eilts and Oakland . . . . .	14
2.6 Roberts and Wilson . . . . .	15

2.7 Isaminger .....	16
2.8 Srivastava .....	17
2.9 Microburst Intensity Predictors .....	18
2.9.1 VIL/TOP .....	18
2.9.2 WINDEX.....	19
2.9.3 Wolfson's Technique.....	20
2.9.4 Rose's Technique .....	21
2.10 Radars .....	21
2.10.1 Terminal Doppler Weather Radar.....	21
2.10.2 Dual Polarization .....	23
2.10.3 NEXRAD Damaging Downburst Prediction and Detection Algorithm.....	24
III. Fundamental Theory and Methodology.....	25
3.1 Theory .....	25
3.1.1 First Law of Thermodynamics and Latent Heat Release.....	26
3.1.2 Boussinesq form of the Vertical Momentum Equation.....	27
3.1.3 Radar Theory.....	29
3.1.3.1 Radar Reflectivity .....	32
3.1.3.2 Doppler Derived Velocity.....	34
3.2 Identification of Microbursts .....	35
3.2.1 Screening of Surface Observations.....	36
3.2.2 Reduction of Sample Size.....	37
3.3 Radar and Thermodynamic Variables.....	39
3.4 Data Collection Equipment .....	40
3.5 Data Processing .....	40



3.5.1 Analysis of Radar Data .....	40
3.5.2 Analysis of Upper Air Data .....	43
3.5.3 Calculation of Microburst Intensity Predictors.....	45
3.6 Development of Proposed Technique .....	45
IV. Data Analysis .....	46
4.1 Description of Data Set .....	46
4.1.1 Description of the Upper Air Data Set .....	46
4.1.2 Description of the Radar Data Set .....	46
4.2 Analysis of Thermodynamic Variables .....	47
4.2.1 Thermodynamic Variables with a Normal Distribution .....	50
4.2.2 Thermodynamic Variables with a Lognormal Distribution ..	52
4.3 Thermodynamic Regression Equation .....	54
4.4 Analysis of Radar Variables .....	58
4.4.1 Radar Variables with a Normal Distribution .....	62
4.4.2 Radar Variables with a Lognormal Distribution.....	63
4.5 Radar Regression Equations .....	65
4.6 Distribution of Microburst Velocity.....	71
4.7 Development of Microburst Forecasting Technique.....	72
4.7.1 Identifying the Microburst Threat .....	72
4.7.2 Predicting the Microburst Intensity .....	75
4.7.3 Identifying Radar Precursors .....	79
4.7.3.1 Radar Signature Examples.....	80
4.7.3.2 Radar Precursor Leadtimes .....	86
4.7.4 Summary of Microburst Forecasting Technique.....	87

V. Conclusions and Recommendations .....	89
5.1 Overview.....	89
5.2 Microburst and Problem Statement Review.....	89
5.3 Review of Methodology.....	90
5.4 Forecasting Technique.....	91
5.5 Possible Sources of Variance .....	91
5.6 Recommendations.....	92
Appendix A: Acronyms .....	94
Appendix B: Wakimoto Screening Criteria .....	96
Appendix C: Example Weather Maps.....	97
Appendix D: Fortran Program READ.....	99
Appendix E: Radar Worksheet.....	104
Appendix F: Upper Air Worksheet.....	112
Bibliography.....	126
Vita.....	128

List of Figures

Figure	Page
1. Schematic Model of a Surface Microburst .....	3
2. Lift as a Function of Velocity for Constant Attack Angle of $9^\circ$ .....	6
3. Illustration of Takeoff Scenario .....	7
4. Vortex Ring Associated with Microbursts .....	12
5. Sine Wave .....	28
6. Wilk-Shapiro Plot for the Height of the Melting Level .....	51
7. Normal Probability Density Function for the Height of the Melting Level .....	52
8. Wilk-Shapiro Plot for LN(CAPE). .....	53
9. Lognormal Distribution of Convective Available Potential Energy .....	53
10. Predicted vs. Observed Plot for Equation (37) .....	56
11. Residual Plot for Equation (37) .....	57
12. Wilk-Shapiro/Rankit Plot of the Residuals from Equation (37) .....	57
13. Wilk-Shapiro Plot of the Aspect Ratios .....	62
14. Normal Distribution of the Aspect Ratios .....	63
15. Wilk-Shapiro Plot of the LN(Maximum Mid Level Convergence) .....	64
16. Lognormal Distribution of Maximum Mid Level Convergence .....	64
17. Predicted vs. Observed Plot for Equations (38) and (39) .....	68
18. Residual Plot for Equation (38) .....	68
19. Residual Plot for Equation (39). .....	69
20. Wilk-Shapiro/Rankit Plot of the Residuals for Equation (38) .....	69

Figure	Page
21. Wilk-Shapiro/Rankit Plot of the Residuals for Equation (39) . . . . .	70
22. Gamma Distribution for Microburst Outflow Velocities . . . . .	72
23. Distribution of $\Delta\theta_e$ with the Critical Temperatures Annotated . . . . .	73
24. Mean Skew-T, Log-p Diagram for Environment Conducive to Microbursts . . . . .	74
25. Mean $\theta_e$ Plot for all 39 Upper Air Soundings . . . . .	75
26. Scatter Plot of Rose's and VIL/TOP Equations vs. Observed Wind Speed . . . . .	77
27. Scatter Plot of Regression Equations vs. Observed Wind Speed . . . . .	78
28. Scatter Plot of WINDEX and Wolfson's Equations vs. Observed Wind Speed . . . . .	79
29. 4-Panel Display of a Rapidly Descending Reflectivity Core Associated with the . . . . .	81
6/23/97 Microburst at Meridian, Mississippi	
30. 3-Panel Display Depicting a Microburst Impacting the Surface Near . . . . .	83
Robbins AFB GA on 8/3/95 with Observed Outflow Velocity of $28.8 \text{ m s}^{-1}$	
31. Reflectivity Notch in Storm Producing Microburst of $18.5 \text{ m s}^{-1}$ Near Macon GA . . . . .	84
32. Divergent Radar Signature Associated with Observed Microburst near Jacksonville FL . . . . .	85
Producing an Outflow of $18 \text{ m s}^{-1}$	
33. Weak Echo Trench Associated with Storm Producing an $18 \text{ m s}^{-1}$ Microburst . . . . .	86
Near Atlanta GA on 8/24/96	
34. Schematic Steps of Proposed Microburst Forecasting Technique. . . . .	88
35. Microburst in Charleston Discounted Due to Hurricane Bertha . . . . .	97
36. Microburst in Birmingham Discounted Due to Cold Front . . . . .	97
37. Surface Map Depicting No Synoptic Features and Favorable to . . . . .	98
Airmass Thunderstorms	

## List of Tables

Table	Page
1. Fujita Scale .....	2
2. Precursor Reliability from 1985-1986 Lincoln Laboratory Study .....	17
3. Comparison of Observation Networks .....	35
4. Radar Microburst Parameters Studied .....	38
5. Sounding Microburst Parameters Studied .....	39
6. Descriptive Statistics of the Thermodynamic Variables .....	48
7. Correlations and P-values of Thermodynamic Variables .....	50
8. Analysis of Variance for Equation (37) .....	56
9. Descriptive Statistics of the Radar Variables .....	59
10. Correlations and P-values of Radar Variables .....	61
11. Analysis of Variance for Equation (38) .....	67
12. Analysis of Variance for Equation (39) .....	67
13. Predicted and Observed Microburst Velocities .....	76
14. RMSE and MAE Table for the Six Intensity Prediction Equations .....	77
15. Occurrence Rate of the 8 Selected Radar Precursor Signatures .....	80
16. Descriptive Statistics for Precursor Leadtimes .....	87

Abstract

Microbursts are intense downbursts from thunderstorms that affect an area less than 4 km and have a lifespan less than 10 minutes. Wet microbursts are associated with heavy precipitation and are common in the eastern and southeastern part of the country. The greatest threat from microbursts is to low flying aircraft, where the rapid fluctuations in horizontal and vertical airflow create tremendous shear zones. Microbursts have been determined to be the causal factor behind at least three major aircraft accidents resulting in numerous fatalities. Due to the short lifespan of microbursts, they often strike without warning and pose a serious challenge to operational forecasters trying to protect Air Force assets.

This thesis seeks to develop a technique to forecast wet microbursts using currently operational technology, including upper air soundings and WSR-88D products. The technique developed is comprised of three distinct phases. First, recognize the potential threat for given environmental conditions. Second, predict the maximum outflow velocities from microbursts using predictive equations. Third, highlight key NEXRAD radar products that demonstrate a strong potential to serve as precursors to microburst formation. Using the technique developed, warning leadtimes on the order of 10 to 20 minutes appear to be reasonable in operational applications.

# FORECASTING WET MICROBURSTS ASSOCIATED WITH SUMMERTIME AIRMASS THUNDERSTORMS OVER THE SOUTHEASTERN UNITED STATES

## I. Introduction

### 1.1 Background

Dr. T. Theodore Fujita first identified downbursts as a culprit in aircraft accidents following the tragic accident of Eastern flight 66 at JFK airport on 24 June 1975. The Federal Aviation Administration asked Fujita to study the incident to determine the cause of the accident. His result was Satellite and Mesometeorology Research Project (SMRP) Paper number 137, first published in 1976 titled, "Spearhead Echo and Downdraft Near the Approach End of John F. Kennedy Airport Runway, New York City," which was later refined into a University of Chicago monograph (Fujita, 1985:45). This paper invigorated the meteorology community and alerted the aviation community to the devastating potential of this deadly phenomenon. In his report Fujita, defined the term downburst as "a strong downdraft that induces an outburst of damaging wind on or near the surface" (Fujita, 1985:8).

Following publication of his report, Fujita headed two major field studies to improve the understanding of downbursts. The projects were the Northern Illinois Meteorological Research on Downbursts (NIMROD), conducted near Chicago in 1978, and the Joint Airport Weather Studies (JAWS), conducted near Denver in 1982 (Fujita, 1985:Ch 5). Analysis of the data collected led Fujita to distinguish two scales of downbursts: the macroburst, a mesoscale event, and the microburst, a misoscale event, horizontal extent between 4 km and 0.04 km (Fujita, 1981: 1514). A macroburst is a downburst that covers an area  $> 4$  km, has a lifespan up to 30 minutes, and can produce winds of  $60 \text{ m s}^{-1}$  (134 mph). A microburst covers an area  $< 4$  km, has a lifespan of up to

10 minutes, and can produce winds of  $75 \text{ m s}^{-1}$  (168 mph) (Fujita, 1985:8). A microburst is capable of producing F3 scale damage relative to a tornado.

**Table 1. Fujita Scale (Fujita, 1981:1517-1518)**

<u>Fujita Scale Value</u>	<u>Wind Velocity</u>	<u>Damage Classification</u>
F0	18-32 $\text{m s}^{-1}$ (40-72 mph)	Light
F1	33-49 $\text{m s}^{-1}$ (73-112 mph)	Moderate
F2	50-69 $\text{m s}^{-1}$ (113-157 mph)	Considerable
F3	70-92 $\text{m s}^{-1}$ (158-206 mph)	Severe
F4	93-116 $\text{m s}^{-1}$ (207-260 mph)	Devastating
F5	117-142 $\text{m s}^{-1}$ (261-318 mph)	Incredible

Following the loss of Pan American flight 759 at New Orleans International airport in 1982 and Delta flight 191 at Dallas-Ft. Worth International airport in 1985, microbursts attracted even greater attention from the aviation and meteorology communities. The Microburst and Severe Thunderstorm (MIST) project was conducted in 1986 over northern Alabama, a more humid climate than Denver where JAWS was conducted. Following the results of this project, microbursts were further categorized as wet or dry (Kingsmill, 1991:262; Wakimoto, 1985:1136).



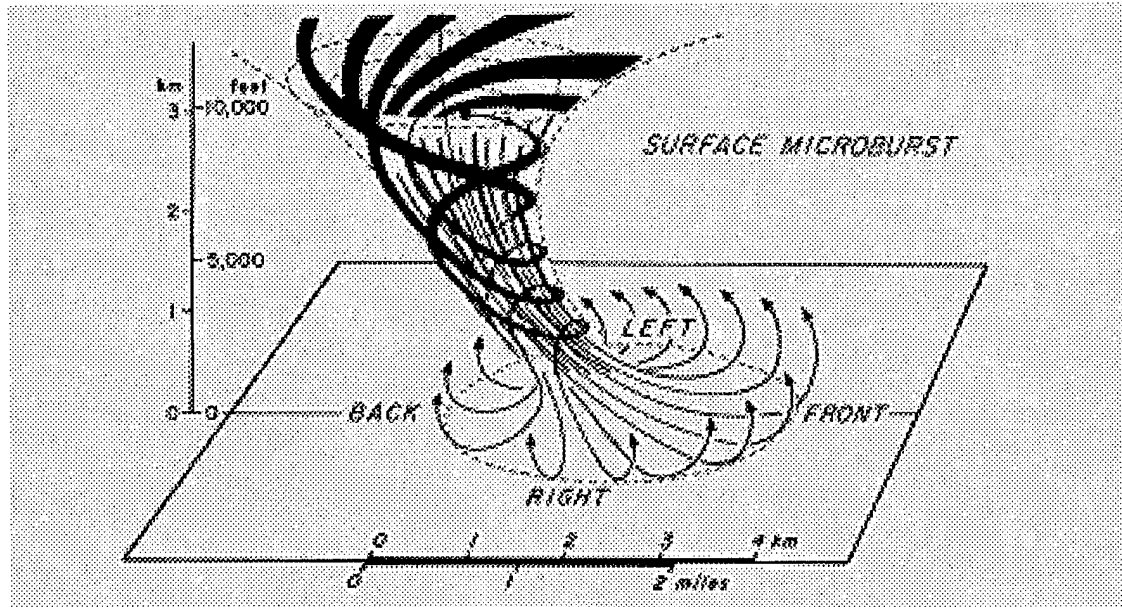


**Figure 1. Schematic Model of a Surface Microburst (Fujita, 1985).  
Reprinted with permission of Univ. of Chicago.**

Dry microbursts in the United States are generally found in the Plains and Rocky Mountain regions. Characteristics of dry microbursts are as follows: less than 0.01 inches of precipitation reaching the ground, a maximum radar reflectivity of 35 dBZ, and a deep, dry, subcloud layer extending up to 500 hPa (Wakimoto, 1985:1131-1135). The formation of dry microbursts occurs as follows. A moist layer is typically present near 500 hPa with a deep dry layer extending from the surface to 500 hPa. As the surface temperature rises through the day, the lower layer becomes super adiabatic and the convective temperature is reached. Shortly after, high-based cumulus clouds form and precipitation is initiated; however, due to the extreme dryness and depth of the subcloud layer the precipitation begins to evaporate immediately and the encompassing parcel cools due to latent heat of evaporation. The temperature of the parcel becomes cooler than the environment; thus, the parcel becomes negatively buoyant and accelerates downward. This process continues as the parcel descends until all moisture evaporates, by which time the parcel has experienced significant downward acceleration, giving rise to a dry microburst.

It is important to note that the evaporation of moisture in the deep, dry, subcloud layer is the physical forcing mechanism driving a dry microburst (Wakimoto, 1985:1131).

Wet microbursts in the United States are generally found in the East and Southeast. Characteristics of a wet microburst are precipitation greater than 0.01 inches and radar reflectivity greater than 35 dBZ. Characteristics of the morning sounding are as follows: the dry, subcloud layer is significantly shallower, extending only up to near 850 hPa, and is capped by a substantial moist layer up to 650 hPa. At the mid level, 650-500 hPa, a dry pocket is present. Besides differing from dry microbursts in terms of formation environment, wet microbursts also have different physical forcing mechanisms. During afternoon heating as the convective temperature is reached, convection is initiated that pushes through the mid-level dry pocket. Falling precipitation, upon reaching the dry pocket begins to evaporate and evaporative cooling begins. Additional cooling is supplied via the latent heat of fusion as frozen hydrometeors, graupel and hail, begin to melt. An additional factor contributing to negative buoyancy in wet microbursts is precipitation loading, which occurs when the weight of water present exceeds the upward vertical acceleration. These factors combine to give rise to a wet microburst. The important forcing mechanisms behind a wet microburst are melting of frozen precipitation, evaporation of precipitation in the dry pocket, and precipitation loading (Atkins and Wakimoto, 1991:472-475).

### 1.2 Problem Statement

Is there a way to reduce the threat to Air Force aviators from wet microbursts associated with summertime, airmass thunderstorms by providing Air Force meteorologists with improved tools and techniques for forecasting wet microbursts over the southeastern United States?

### 1.3 Importance of Research

Wet microbursts were identified as the cause behind three recent major airline accidents: Eastern flight 66, 1975, at JFK International, 112 fatalities; Pan American flight 759, 1982, at

New Orleans International, 152 fatalities; and Delta flight 191, 1985, at Dallas-Ft. Worth International, 130 fatalities (Wolfson, 1990:341). Clearly this phenomenon poses a significant threat to aircraft operating in the humid, summertime environment of the southeastern United States. The greatest hazards associated with wet microbursts are encountered during landings and takeoffs. This threat is compounded by pilot inexperience. Air Education and Training Command's (AETC) mission includes training pilots, and a portion of that training takes place in the Southeast. The ability of weather units supporting operations in this region to advise aviators of the potential danger prior to microburst occurrence will aid in preventing accidents.

1.3.1 Aircraft Performance During a Wet Microburst. There are seven variables that influence aircraft performance during flight. They are configuration geometry, angle of attack, vehicle size, free-stream velocity, density of the undisturbed air, Reynolds number, and Mach number (Bertin, 1989:181). The amount of lift provided to an aircraft can be estimated as:

$$F = \frac{1}{2} \rho V^2 A C_L(\alpha) \quad (1)$$

where

F is the lift force (Newtons),

$\rho$  is the density of air at flight level ( $\text{kg m}^{-3}$ ),

V is aircraft velocity ( $\text{m s}^{-1}$ ),

A is the plan surface area of the wing ( $\text{m}^2$ ), and

$C_L(\alpha)$  is the coefficient of lift as a function of attack angle (non-dimensional).

Making the following assumptions: symmetrical airfoil, air density at sea level, no turbulence, and sub-sonic aircraft speed, equation (1) can be simplified as:

$$F = \frac{1}{2} \rho V^2 A 2\pi\alpha \quad (2)$$

where

$\alpha$  is the angle of attack (radians).

Using equation (2) the lift for two aircraft with wing surface areas of a T-1A and C-17 respectively, with varying velocities is shown in Figure 2 (Jackson, 1995:588,638).

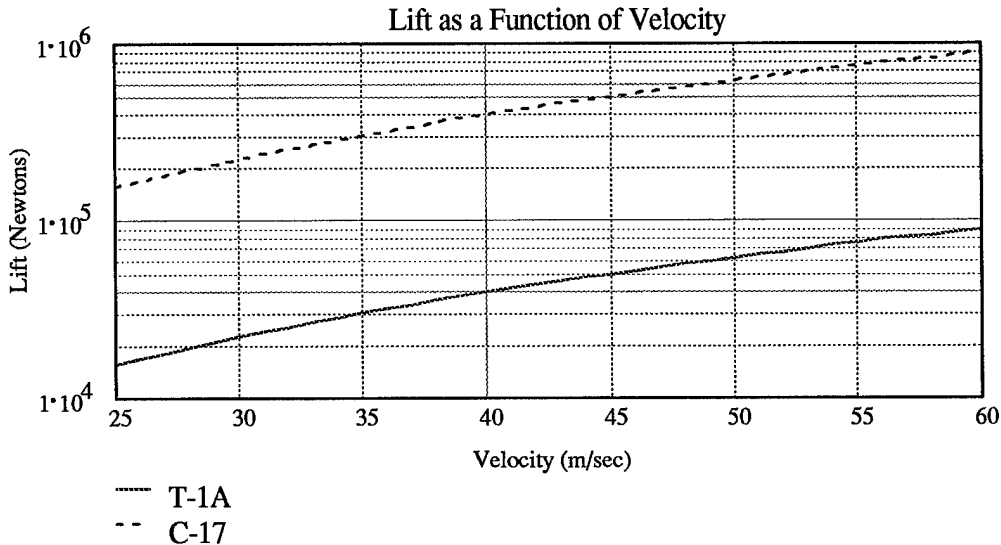


**Figure 2. Lift as a Function of Velocity for Constant Attack Angle of 9°.**

This figure demonstrates that rapid fluctuations in speed, such as experienced while transiting a microburst, would result in similarly radical changes in lift provided. For example, a T-1A maintaining a constant attack angle of 9° and experiencing a relative airspeed decrease from 40 m s<sup>-1</sup> to 30 m s<sup>-1</sup> would subsequently experience a loss of lift of approximately 47%. Such dramatic loss of lift during takeoff or landing could result in an accident.

**1.3.2 Illustrative Example.** A theoretical example better illustrates the potential threat to aircrews. An aircraft taking off in a microburst developing at the takeoff end of the runway could experience the following scenario. At initial point, brake release, the aircraft accelerates down the runway and experiences an increase in lift due to the sudden increase in headwind; at this time the microburst is still developing and has yet to reach maximum divergence. When the aircraft nears

liftoff, the microburst is still developing and the aircraft experiences a continuously increasing headwind, increasing lift above that to be expected from the indicated aircraft speed reading. Takeoff proceeds and the pilot assumes an attack angle of  $15^\circ$ . Immediately following liftoff, the aircraft is located in the center of the now mature microburst and experiences  $0 \text{ m s}^{-1}$  of headwind and  $40 \text{ m s}^{-1}$  of downward directed airflow, dramatically decreasing the lift force in a matter of seconds. To compensate for the loss of lift, the pilot increases power and decreases attack angle to gain airspeed and lift. The aircraft then enters the opposite side of the microburst and is subjected to a sudden strong tailwind. The tailwind reduces airflow over the wing surface further decreasing lift. To compensate for the loss of lift, the pilot positions the aircraft in a negative attack angle in an attempt to gain airspeed and lift. The microburst begins to decay and the aircraft loses its tailwind; however, the aircraft is now positioned nose down and very near the ground. If the aircraft is unable to compensate for these rapid fluctuations in lift and airspeed, impact results.

Figure 3 summarizes this scenario.

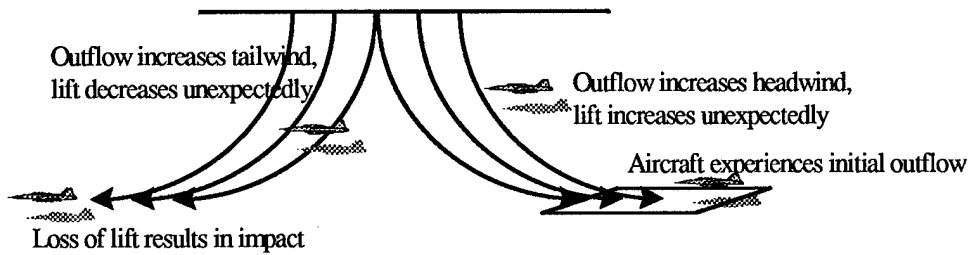


**Figure 3. Illustration of Takeoff Scenario.**

#### 1.4 Objectives

This thesis seeks to meet several key objectives. The first objective is to improve the abilities of Air Force forecasters to predict and warn supported customers of the occurrence of wet microbursts associated with summertime, airmass thunderstorms over the southeastern United States. The second objective is to identify and correlate the environmental conditions favorable for

the formation of wet microbursts. The most important objective is to identify WSR-88D (Weather Surveillance Radar 88-Doppler or NEXRAD) signatures associated with wet microbursts, and develop techniques using the NEXRAD as the primary tool for operational forecasters to provide warning prior to wet microburst occurrence.

### 1.5 Overall Approach

There were four main tasks to be accomplished to achieve the objectives outlined in the previous section. The first task was to identify possible microburst events by screening surface observations. Using a set of six simultaneous criteria modeled after those used during previous studies, possible microbursts were selected from over 450,000 surface observations (Fujita, 1985:53-54; Wakimoto, 1985:1133). The number of events considered was further refined based upon the proximity of a NEXRAD and any synoptic features affecting the development of thunderstorms. The second task was to collect upper air and radar data corresponding to the previously identified possible microburst events. This was done by selecting the available archive level II and upper air soundings for the locations and times closest to the events and requesting the data from the Air Force Combat Climatology Center. The third task was data processing. This was accomplished using the Weather Algorithm Testing and Display System (WATADS) software for radar data and plotted upper air soundings and equivalent potential temperature, or  $\theta_e$ , plots. Using different precursors suggested by numerous authors, key radar (Radio Detection and Ranging) and thermodynamic variables were identified. The last task was to perform a statistical analysis of the processed data. The goal of this statistical analysis was to determine the likelihood and intensity of wet microbursts and the development of an operational microburst forecasting technique.

## 1.6 Summary of Results

A proposed forecasting technique entailing three steps was developed to reliably predict wet microbursts. First, identify the threat of microbursts occurring during the period and in the area of interest. Second, estimate the maximum outflow velocity to be expected for the day and area of interest. Finally, actively watch the NEXRAD Primary User Position (PUP) display for precursor radar signatures.

## 1.7 Organizational Overview

Chapter 2 is a summary of the literature review conducted. It highlights some of the results from previous field studies as well as tools and techniques used to attempt to predict the behavior of wet microbursts. The chapter encompasses the early work of Fujita through recent advances in Doppler radar algorithms.

Chapter 3 covers some of the basic principles of Doppler radar and reviews the first law of thermodynamics and the physics behind wet microburst formation. Also discussed in Chapter 3 are the equipment and techniques employed to study radar and thermodynamic data.

Chapter 4 covers the data that was studied and highlights the most significant variables that preceded wet microburst events. Examples of prominent radar precursors are presented. The results of statistical analyses performed are also part of Chapter 4. Lastly, a proposed forecasting technique is presented.

Chapter 5 provides the overall results of the conducted research. The most important results are highlighted and suggested tools and techniques are described for use by operational forecasters. Lastly, conclusions regarding the research and suggestions for future ventures are presented.

## II. Literature Review

### 2.1 NIMROD

The first concerted, major field study of microbursts was the Northern Illinois Meteorological Research on Downbursts which took place in 1978 in the Chicago area under the leadership of Fujita and Srivastava (Fujita, 1985:45). Using images from the LANDSAT satellite, supplied by NASA, a network of 27 Portable Automated Mesonet (PAM) stations, spaced approximately 4 km from each other, and three research Doppler radars was designed. This network maintained continuous observations from 19 May through 1 July. In addition to surface and radar observations, hourly upper air soundings were taken, profiling the changing vertical structure of the atmosphere in the test area (Fujita, 1985:45-48). During this period researchers counted 61,766 wind peaks associated with thunderstorms in the observation network. Using an algorithm developed to identify microbursts using observations from the PAMs this number was reduced to 143 possible microbursts. Lastly, examination of the 143 possible microbursts by meteorologists reduced the final number of microburst events to 50 (Fujita, 1985:53-55).

### 2.2 JAWS

Independent observations by operational forecasters in the Denver area indicated that numerous microbursts developed from high based cumulus clouds. To investigate these events as well as increase the understanding of microbursts, the Joint Airport Weather Studies project, led by Fujita, McCarthy, and Wilson, took place in the Denver area from 15 May to 9 August 1982 (Fujita, 1985:49-53). The field study included 27 PAMs with an average spacing of 2 km, and three Doppler research radars from NCAR. As with NIMROD, hourly atmospheric soundings were also taken (Fujita, 1985:50-53). During JAWS 123,956 wind peaks were recorded; screening these events using the same algorithm used in NIMROD reduced the number of possible



microburst occurrences to 436. Final screening by meteorologists further reduced the sample size to 186 microburst events (Fujita, 1985:54-55).

### 2.3 Results of NIMROD and JAWS

The high density of PAMs, human observers, upper air soundings, and radars yielded copious amounts of data that immensely increased the meteorological community's understanding of microbursts. Both projects recorded surface observations every minute on the mesoscale and provided triple Doppler analysis of microburst-producing storms, giving researchers highly detailed data on the evolution of microbursts (Fujita, 1985: Ch 5; Wilson et al., 1984:898-900,905-906). Considering the behavior, development, and environment in which microbursts formed, the two projects' microbursts were further categorized as wet or dry (Fujita, 1985:Ch 6). Based on observations taken during these projects some of the following characteristics of microbursts were determined. First, the presence of a horizontal vortex ring at the surface was observed by both radar and photography, especially visible during JAWS, due to the lack of precipitation and the greater quantity of dust; see Figure 4 (Fujita, 1985:16). Also, observations of Doppler derived velocity fields indicated that wet microbursts often accelerate when descending through the melting level (Fujita, 1985:16). Finally, results from both projects showed a high frequency of microbursts associated with non-severe thunderstorms and high based cumulus or altocumulus clouds (Fujita, 1985:47,70).

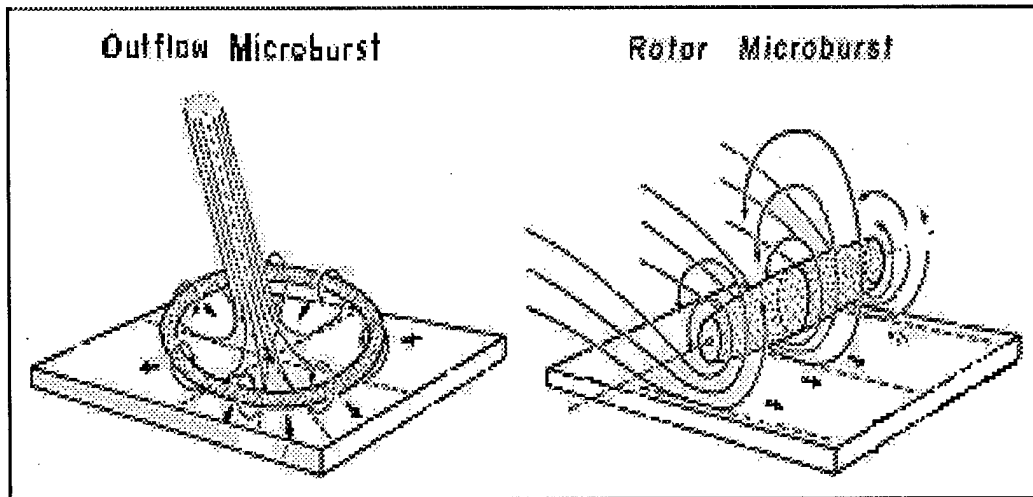


**Figure 4. Vortex Ring Associated with Microbursts (Fujita, 1985).  
Reprinted with permission of Univ. of Chicago.**

Results also indicated that there was no apparently favorable vertical wind profile for microburst formation; however, a strong correlation was drawn to the thermodynamic environment between days producing microbursts and days without microbursts (Wakimoto, 1985:1135-1139). Surface based observations showed microbursts demonstrated no preference for temperature or pressure changes; some microbursts raised surface temperatures while others lowered temperatures; some raised the surface pressure, while others lowered surface pressure. However, macrobursts showed a clear preference to lower temperatures and raise surface pressures (Fujita, 1985:61,66). The last significant finding from these two projects was the frequent presence of rotation aloft in the lower levels of a microburst-producing storm while the microburst flow at the surface was generally irrotational (Fujita, 1985:72-74).

#### 2.4 MIST

During the summer of 1986 a very detailed study of wet microbursts was conducted over northern Alabama titled Microburst and Severe Thunderstorm (MIST). MIST included a mesonet system of 71 automated observation stations spaced approximately 2 km apart, similar to those

used in NIMROD and JAWS. Also included were two upper air observing sites, and five Doppler research radars, one of which was dual polarized (Atkins and Wakimoto, 1991:471).

Post analysis of the results agreed with theory; wet microbursts are physically different from dry microbursts. The thermodynamic environment favorable to the development of wet microbursts was identified and shown to have the following characteristics: widespread instability due to surface heating or mesoscale forcing; a shallow surface-based radiation inversion on the morning soundings, which limits early thunderstorm development, with a near-dry adiabatic layer up to near 850 hPa; a substantial moist layer from 850 hPa up to mid levels with a dry pocket above the moist layer; and high surface relative humidity values. Moderate values of Convective Available Potential Energy (CAPE) and large values of Bulk Richardson Number (BRN) were also noted. The most significant thermodynamic feature observed was a critical value for  $\Delta\theta_e$  of 20 K, where  $\Delta\theta_e$  is defined as the difference between the near-surface equivalent potential temperature and the minimum equivalent potential temperature at the mid levels (Atkins and Wakimoto, 1991:472-479). Equivalent potential temperature is defined as:

$$\theta_e = \theta \cdot \exp\left[\frac{Lw}{c_p T}\right] \quad (3)$$

where

$$\theta = T \cdot \left[\frac{p_o}{p}\right]^{\frac{R}{c_p}} \quad (4)$$

and

$\theta_e$  is equivalent potential temperature (Kelvin),

$\theta$  is potential temperature (Kelvin),

L is latent heat of evaporation ( $\text{J kg}^{-1}$ ),

w is the mixing ratio ( $\text{kg kg}^{-1}$ ),

$c_p$  is the specific heat of air at constant pressure ( $J K^{-1} kg^{-1}$ ),

T is temperature (Kelvin),

R is the gas constant for dry air ( $J K^{-1} kg^{-1}$ ),

$p_0$  is the reference pressure 1000 hPa, and

p is the pressure at the level where T is measured (hPa).

Using the multiple Doppler radar network several key findings were discovered. Several precursors to microburst occurrence were identified based upon observed storm reflectivity and velocity fields.

Some of the following reflectivity signatures were identified as possible event precursors: a reflectivity core with a maximum of 55 dBZ ascending to or above the level of the minimum  $\theta_e$  value, storm tops reaching an altitude of 10 km, and a rapidly descending reflectivity core (Atkins and Wakimoto, 1991:480-481). Also observed with some events was the presence of a weak echo trench on the Plan Position Indicator (PPI) view of the mid levels of microburst producing storms (Kingsmill and Wakimoto, 1991:262).

Other than distinct reflectivity signatures, several key velocity signatures were also observed. Convergence aloft, especially near the level of minimum  $\theta_e$ , was noted on numerous occasions preceding microbursts (Atkins and Wakimoto, 1991:470,480; Kingsmill and Wakimoto, 1991:278). Counter-clockwise rotation near the cloud base was also frequently present (Kingsmill and Wakimoto, 1991:277; Isaminger, 1988:5). The last velocity feature observed was divergent storm tops seen in 90% of the cases (Isaminger, 1988:5).

## 2.5 Eilts and Oakland

Building on the results from MIST, Eilts and Oakland collected data from a single Doppler on central Oklahoma, summertime, microburst-producing thunderstorms during the summers of 1987 and 1988 (Eilts and Oakland, 1989:190). The aim of this project was to determine

precursors to severe microbursts in central Oklahoma. Rawinsonde analysis showed the most favorable environment characterized by lifted indices of -1 to -4, weak vertical shear, and nearly dry adiabatic lapse rates in the lowest 3 km (Eilts and Oakland, 1989:191). Using 8 sample cases, an attempt was made to determine the strength of the microburst based upon convergence in the mid levels. The magnitude of the mid level convergence had a correlation factor of  $r = 0.89$  with the magnitude of the radar-measured, near-surface divergence (Eilts and Oakland, 1991:191).

Observations made with the radar also showed that stronger downbursts required weak convergence over a deeper layer or stronger convergence over a shallow layer. Lastly, based upon radar observations only, three precursors to microburst events were identified: a strong core aloft ( $> 55$  dBZ), detectable rotation in the lower levels of the storm, and convergence in the mid levels when the storm core began descending. The detection of mid level convergence demonstrated the greatest promise for use as a nowcasting precursor (Eilts and Oakland, 1991:192).

## 2.6 Roberts and Wilson

In 1988 Roberts and Wilson used data from JAWS and CLAWS (Classify, Locate and Avoid Wind Shear) to examine 31 microburst-producing storms over northeastern Colorado (Roberts and Wilson, 1989:285). The primary purpose of their research was to determine possible precursors to microburst events. Evaluation of the rawinsonde soundings indicated good agreement with earlier studies with a  $\theta_e$  minimum at mid levels and near-dry adiabatic lapse rate below cloud base (Roberts and Wilson, 1989:285). Based upon the available radar data, four possible precursors were identified. In order of precedence they were descending reflectivity core, increasing convergence within cloud and near cloud base, a reflectivity notch on PPI scans, and rotation (Roberts and Wilson, 1989:299). The presence of a reflectivity notch and rotation were deemed as not necessary and sufficient for a microburst event; however, when observed in conjunction with a descending core or convergence aloft, presence of those characteristics was

associated with increased probability of a microburst (Roberts and Wilson, 1989:299). Convergence aloft was observed in 25 of 31 cases. Also, 24 of 31 had rotation, and 50% possessed a reflectivity notch (Roberts and Wilson, 1989:296). The presence of a reflectivity notch seemed to indicate strong influx of drier air from the level of  $\theta_e$  minimum. In addition to these four precursors, two other reflectivity features were associated with microbursts. First, the horizontal location of the main reflectivity core coincided with the location of the surface microburst in 30 of 31 events. Second, convergence near the melting level was associated with a rapidly accelerating downdraft, likely due to cooling from melting graupel, hail, or ice crystals (Roberts and Wilson, 1989:291,296).

### 2.7 Isaminger

Lincoln Laboratory conducted wet microburst research in the summers of 1985 and 1986 using Terminal Doppler Weather Radar (TDWR) S-band radars located in Memphis and Huntsville. The goal of this research effort was to develop automated algorithms for use by the Federal Aviation Administration to warn aviators of impending microburst events (Isaminger, 1988:i). Research focused on the four following precursors: descending reflectivity core, convergence aloft, rotation near cloud base, and the presence of a distinct reflectivity notch (Isaminger, 1988:iii). Doppler analyses were conducted on 34 microburst-producing storms and 23 null events where thunderstorms were present, but no microbursts occurred (Isaminger, 1988:6,10). Due to radar elevation scan limitations the tops of all storms were not interrogated. A storm core was defined as possessing reflectivity > 50 dBZ extending at least 5.2 km vertically (Isaminger, 1988:1).

Based upon the data recorded the four precursors proved to be highly reliable in predicting microburst events as summarized in Table 2 below.

**Table 2. Precursor Reliability from 1985-1986 Lincoln Laboratory Study (Isaminger, 1988).**

Precursor	Microburst Storms	Non-Microburst Storms
Descending core	95%	9%
Rotation in mid levels	59%	4%
Convergence in mid levels	41%	4%
Divergent storm tops	93%	Not Available

At least one precursor was present in over 90% of the microburst producing storms (Isaminger, 1988:10). The author also concluded that weaker convergence aloft was associated with weaker outflow at the surface with a nearly one-to-one ratio of velocity magnitudes (Isaminger, 1988:12).

Isaminger also quantified warning lead-times based on the identified precursors and his sample. The median warning lead-time for first, second, and third precursors were 7, 4, and 1 minute, respectively. In order to minimize false alarms while maintaining reliability he suggests warnings be issued on the occurrence of the second precursor (Isaminger, 1988:14).

### 2.8 Srivastava

While the physical forcing mechanism driving dry microbursts is generally agreed to be evaporation in the deep, dry, subcloud layer, much less agreement exists regarding the driving forces of wet microbursts. In an effort to improve meteorologists' understanding of wet microbursts Srivastava developed a wet microburst model that incorporates several features. The first feature was a favorable pressure perturbation in the lowest levels of a downdraft-producing thunderstorm. This perturbation is created by rotation near the cloud base (Srivastava, 1987:1753). Other researchers have also identified the presence of counter-clockwise rotation in the lowest levels of microburst producing storms, believed to funnel mass inward and downward. Incorporating the fact that evaporation is crucial in wet microburst formation and smaller water

and ice particles evaporate more quickly than larger ones, Srivastava's model includes such factors as rain drop collision rates, drop size distribution, terminal velocity, and rainfall rate when determining downburst formation and intensity (Srivastava, 1987:1753).

## 2.9 Microburst Intensity Predictors

During 1990-1991 non-tornadic winds from thunderstorms resulted in 71 fatalities, 1093 injuries, and \$719 million in damages (Eilts et al., 1996:541). Clearly, being able to predict the intensity of downbursts is of interest to both aviators and ground personnel. Several theoretically and empirically derived equations have been developed to achieve accurate forecasts of microburst intensity, four of which are discussed.

2.9.1 VIL/TOP. An equation for predicting maximum downdraft speed based on the equations of conservation of mass, momentum, heat, and water was used by Stewart (Stewart, 1996:324).

This equation was further refined through empirical observations as:

$$-W_{\max} = ((20.628571 \text{ m s}^{-2} l_c H) - (3.125 \times 10^{-6} \text{ s}^{-2} H^2))^{1/2} \quad (5)$$

where

$-W_{\max}$  is the maximum velocity ( $\text{m s}^{-1}$ ),

$l_c$  is the liquid water content ( $\text{g g}^{-1}$ ), and

$H$  is the maximum penetrative depth of cloud above ground level (m).

The liquid water content of clouds is estimated using radar reflectivity regularly. For VIL/TOP the transformation is (Stewart, 1996:324):

$$l_c \approx 3.44 \times 10^{-3} Z^{A/7} \quad (6)$$

where

$Z$  is radar reflectivity factor ( $\text{mm}^6 \text{ m}^{-3}$ ).

Stewart then assumes 1 kg of dry air has a volume of  $1 \text{ m}^3$  and  $H$  can be approximated by the echo tops derived from current NEXRAD algorithms to yield:



$$-W_{\max} = ((20.628571 \text{ VIL}) - (3.125 \times 10^{-6} \text{ TOP}^2))^{1/2} \quad (7)$$

where

VIL is vertically integrated liquid computed by the NEXRAD ( $\text{kg m}^{-2}$ ), and

TOP is the height above sea level of the storm computed by the NEXRAD (100's ft).

The final wind velocity is estimated by adding 1/3 of the mean wind speed in the lowest 5000 feet, yielding the VIL/TOP technique (Stewart, 1996:324). Using 11 microburst events from Oklahoma and Florida Stewart achieved a correlation factor of  $r = 0.95$  between predicted and observed outflow velocities (Stewart, 1996:3258). Sources of error include possible overestimation of VIL due to hail contamination and location of microburst event relative to recording instrument (Stewart, 1996:327).

2.9.2 WINDEX. A second proposed downburst predictor is the wind index (WINDEX) developed by McCann. WINDEX was derived from the vertical momentum equation and vertical soundings from environments known to have produced microbursts (McCann, 1994:533). The WINDEX computes a measure of downdraft instability and an estimate of outflow velocity; high WINDEX values are generally associated with significant microbursts (McCann, 1994:535). The WINDEX equation is:

$$\text{WI} = 5(H_M R_Q (\Gamma^2 - 30 + Q_L - 2Q_M))^{1/2} \quad (8)$$

where

WI is the computed WINDEX value,

$H_M$  is the height of the melting level above ground (km),

$Q_L$  is the mixing ratio in the lowest 1 km above ground level ( $\text{g kg}^{-1}$ ),

$Q_M$  is the mixing ratio at the melting level ( $\text{g kg}^{-1}$ ),

$\Gamma$  is the mean lapse rate from the surface to the melting level ( $^{\circ}\text{C km}^{-1}$ ), and

$R_Q = Q_t/12$ , but must be less than 1.

When using WINDEX the following considerations must be made. First, WI is set to zero if  $\Gamma^2 < 30$ . Next, if  $R_Q > 1$ , then  $R_Q$  is set to 1. Lastly, WINDEX is highly sensitive to changes in the mean lapse rate (McCann, 1991:533,535).

2.9.3 Wolfson's Technique. Given that microbursts develop in a non-hydrostatic environment, Wolfson has developed two predictive equations for downburst velocity and outflow velocity using the Boussinesq form of the vertical momentum equation and the shallow density current equation. Her equations are based on both thermodynamic considerations and radar observations, as radar reflectivity factor alone is not sufficient to predict microburst potential (Wolfson, 1996:340). By combining the vertical momentum and density current equations with results from earlier microburst studies Wolfson's empirical equations for downdraft velocity and outflow velocity are:

$$W^2 = (7.3\Gamma^2 + 9.75LD - 480)Tr/3.3 \quad (9)$$

$$U/W = (0.75/A + 0.65)\Gamma/9 \quad (10)$$

respectively (Wolfson, 1996:344), where

W is the maximum downdraft velocity ( $m\ s^{-1}$ ),

U is the maximum outflow velocity ( $m\ s^{-1}$ ),

$\Gamma$  is the mean environmental lapse rate up to the melting level ( $K\ km^{-1}$ ),

L is the peak mixing ratio ( $g\ kg^{-1}$ ),

D is the depth of the precipitation core (km),

Tr is the transition level, the level AGL where the sounding becomes neutral or stable (km), and

A is the aspect ratio or ratio of core height to core width (dimensionless).

Correction is required if U/W is less than 1; then U/W is set equal to one. Using four sample cases

Wolfson's equations had a mean error of  $2.35\ m\ s^{-1}$  and  $2.075\ m\ s^{-1}$  for W and U respectively.

2.9.4 Rose's Technique. Building on the hypothesis that the conversion of horizontal momentum to downward momentum plays a key role in determining the intensity of microbursts, Rose has developed an equation of downward transport and refined that equation using regression techniques and 22 microburst events in the Nashville area from 1995 and 1996 (Rose, 1996:11-14). He defines the shear layer as the depth at which winds cease to display increases in velocity with height (Rose, 1996:14). The equation of downward transport is:

$$V_{\max} = (V_d \cdot V_{\text{avg}} g z)^{\frac{1}{4}} \quad (11)$$

where

$V_{\max}$  is the maximum potential downdraft velocity ( $\text{m s}^{-1}$ ),

$V_d$  is the wind speed at the top of the shear layer less the surface wind speed ( $\text{m s}^{-1}$ ),

$V_{\text{avg}}$  is the mean wind speed in the shear layer ( $\text{m s}^{-1}$ ),

$z$  is the depth of the shear layer (m), and

$g$  is the acceleration due to gravity ( $\text{m s}^{-2}$ ).

Based upon the 22 cases considered the modified downward transport equation is:

$$V_{\max} = (0.296) \cdot (V_d \cdot V_{\text{avg}} g z)^{\frac{1}{4}} + 20.6. \quad (12)$$

## 2.10 Radars

Numerous Doppler radars have been used to study microbursts with very good success.

The three most likely to be encountered are discussed below with their merits and drawbacks.

2.10.1 Terminal Doppler Weather Radar. The TDWR was developed as a response from the FAA to increase the capability of meteorologists supporting airfield operations to detect wind shear events near major airports. This radar completes a scan sequence every 4 minutes, updating the lowest 4 elevation slices every minute, and scans a total of 16 elevation slices (Isaminger, 1988:2). The pulse repetition frequency of the TDWR can reach 2000 Hz yielding high resolution velocity

measurements (Rinehart, 1991:290). The range of the TDWR is limited to only near the airfield via the 'Doppler Dilemma', which says improvements in velocity come at the expense of sacrificed range since

$$V_{\max} \cdot r_{\max} = \frac{c\lambda}{8} \quad (13)$$

where

$V_{\max}$  is the maximum detectable velocity ( $\text{m s}^{-1}$ ),

$r_{\max}$  is the maximum range of the radar (m),

$c$  is the speed of light in vacuum ( $2.99792 \times 10^8 \text{ m s}^{-1}$ ), and

$\lambda$  is the wavelength (m).

Wilson et al. proposed three deployment schemes using the TDWR. These three schemes were the dual radar off airport, single radar off airport, and single radar at the airport (Wilson et al., 1984:907-909). Each of these is reviewed in the following paragraphs.

The first deployment concept is the dual Doppler off airport. This concept follows directly from experience gained during the JAWS project. Two TDWR radars are deployed approximately 14 km from the airport separated by a  $70^\circ$  azimuth. This positioning allows for more precise observations of velocity fields by combining information and reducing the probability of beam blockage from surface features or hydrometeors (Wilson et al., 1984:907). The requirement to maintain two radars compounds issues of maintenance, calibration, and communications.

A second proposed scenario positions a single radar within 40 km of the airport, situated along a major flight path. This allows direct sampling of inbound and outbound winds parallel to the runways. Drawbacks include the need for precise location of the radar and complications estimating low level near airfield features (Wilson et al., 1984:907-908).

The third deployment choice places a single radar at the airfield. This allows for greater coverage of flight paths near the airfield and resolution of low level near airfield wind fields. The main drawback to this choice is the lack of ability to interrogate the upper levels of storms near the airfield for precursors such as storm top divergence (Wilson et al., 1984:909).

2.10.2 Dual Polarization. During the Cooperative Huntsville Meteorological Experiment (COHMEX), conducted jointly with MIST, a dual horizontal/vertical polarized radar was used to evaluate the presence of ice within the core of microburst-producing storms. This radar measured radar reflectivity differential,  $Z_{DR}$ , by comparing the radar reflectivity factor for the horizontally polarized beam to the vertically polarized beam,  $Z_{DR}$  is computed as:

$$Z_{DR} = 10 \cdot \log\left(\frac{Z_H}{Z_V}\right) \quad (14)$$

where

$Z_{DR}$  is radar reflectivity differential (decibel),

$Z_H$  is the radar reflectivity factor from horizontally polarized beam (dBZ), and

$Z_V$  is the radar reflectivity factor from vertically polarized beam (dBZ).

Large raindrops typically register  $Z_{DR}$  near 4.5 dB while small raindrops usually register near 0 dB. The difference is due to the oblateness, or non-spherical nature, of falling raindrops, which is a function of gravity, surface tension, and aerodynamics (Bringi, 1984:1145). While hail is not symmetrical, it tumbles as it falls and registers nearly identical signatures when viewed with either a horizontally or vertically polarized radar. In addition, the probability of hail increases as radar reflectivity factor increases, while reflectivity differential decreases (Bringi, 1984:1145,1146). Applying this concept leads to a reflectivity differential or  $Z_{DR}$  holes within high reflectivity storm cores. On a dual polarized radar these appear as areas of low differential signal return surrounded by a region of higher differential signal return. These holes generally indicated

the presence of hail or ice within the storm cores. The presence of ice within the storm core was frequently noted during the MIST project in association with microburst-producing storms (Wakimoto and Bringi, 1988:1522).

2.10.3 NEXRAD Damaging Downburst Prediction and Detection Algorithm. The NEXRAD Operational Support Facility in conjunction with the National Severe Storms Lab (NSSL) is seeking to develop and implement the Damaging Downburst Prediction and Detection Algorithm (DDPDA) for use with the WSR-88D. This algorithm, while still in development, focuses on 5 precursors to microbursts: a rapidly descending reflectivity core, convergence at mid level, a reflectivity core that initially begins at an altitude greater than other storms that day, mid altitude rotation, and storm top divergence (Eilts et al., 1996:541-542). The DDPDA was built using a sample of 85 microbursts from Florida, Oklahoma, Arizona, and Colorado (Eilts et al., 1996:541). A prototype of this algorithm was tested in the summers of 1994 and 1995 in Phoenix, Arizona. The algorithm demonstrated prediction rates as high as 85% and as low as 30% with an average of 66% accuracy for all cases. During this proof of concept test the lead-time to maximum divergence signature ranged between 12.1 minutes to 7.2 minutes (Eilts et al., 1996:542,543). Additional proof of concept testing has occurred at Kansas City; Melbourne, Florida; Sterling, Virginia; and Salt Lake City, and the DDPDA is currently being evaluated at the NSSL's Weather Decision Support System; however, it is not scheduled to be fielded within the next several years (Smith, 1997).

### III. Fundamental Theory and Methodology

#### 3.1 Theory

A brief review of the first law of thermodynamics and latent heat release processes is presented. Following this review the Boussinesq form of the vertical momentum equation and its use as a model of downbursts is discussed. Lastly, a review of the basic principles of radar and Doppler radar is given.

3.1.1 First Law of Thermodynamics and Latent Heat Release. The first law of thermodynamics can be expressed in the following form

$$dq = c_p dT - \alpha dp \quad (15)$$

where

$dq$  is the incremental heat energy per unit mass ( $J\ kg^{-1}$ ),

$c_p$  is specific heat at constant pressure, intrinsic property of substance, ( $J\ kg^{-1}\ K^{-1}$ ),

$dT$  is the incremental temperature change (K),

$\alpha$  is the specific volume ( $m^3\ kg^{-1}$ ), and

$dp$  is the incremental pressure change (Pa).

In this form the first law states that the amount of heat energy exchanged in a system is equal to the product of the change in temperature and specific heat of a substance, less the product of the specific volume and incremental change in pressure. For an isobaric process, one in which pressure remains constant, equation (15) simplifies as

$$dq = c_p dT. \quad (16)$$

If an isobaric change of phase occurs, e.g., water to vapor, the amount of heat energy required is expressed as the product of the latent heat of the substance and the amount of mass change. For water this is expressed as

$$dq = l_v dw_1 \quad (17)$$

and

$$dq = l_f dw_i \quad (18)$$

where

$l_v$  is the latent heat of vaporization, a function of temperature (approximated as  $2.5 \times 10^6 \text{ J kg}^{-1}$ ),

$dw_1$  is the incremental change in mass of water condensed/evaporated per unit mass of air ( $\text{g kg}^{-1}$ ),

$l_f$  is the latent heat of fusion, a function of temperature (approximated as  $3.34 \times 10^5 \text{ J kg}^{-1}$ ), and

$dw_i$  is the incremental change in mass of water melted/fused per unit mass of air ( $\text{g kg}^{-1}$ ).

Combining equation (16) with equations (17) or (18), depending on which change of phase, states that the change in the temperature of the environment within which evaporation or melting occurs will be reduced accordingly. Once evaporation or melting occurs the parcel from which heat energy is drawn becomes more dense than the environment and therefore negatively buoyant.

3.1.2 Boussinesq form of the Vertical Momentum Equation. A basic model of the vertical acceleration experienced by a parcel during a microburst is given by the Boussinesq form of the vertical momentum equation (Wolfson, 1996:342), expressed as

$$\frac{dw}{dt} = g \left( \frac{\theta_e - \theta_p}{\theta_e} \right) - g(1+i) - \frac{p'_z}{\rho_o} \quad (19)$$

(a)                      (b)                      (c)

where

$\frac{dw}{dt}$  is the parcel acceleration ( $\text{m s}^{-2}$ ),

$g$  is the acceleration due to gravity ( $9.8 \text{ m s}^{-2}$ ),

$\theta_p$  is the potential temperature of the parcel, as given by equation (4), (K),

$\theta_e$  is the potential temperature of the environment (K),



$l$  is the mixing ratio of liquid water ( $\text{kg kg}^{-1}$ ),

$i$  is the mixing ratio of ice ( $\text{kg kg}^{-1}$ ),

$p'_z$  is the vertical pressure perturbation (Pa), and

$\rho_o$  is the density of the environment ( $\text{kg m}^{-3}$ ).

This simple model accounts for three distinct forces acting on the parcel denoted as  $a$ ,  $b$ , and  $c$  in equation (19). The first force,  $a$ , is the buoyancy force, due to the difference in temperature between the environment and the parcel. When evaporation or melting occurs latent heat must be supplied and the parcel cools. Using the ideal gas law

$$p = \rho R T \quad (20)$$

where

$p$  is pressure (Pa),

$\rho$  is density ( $\text{kg m}^{-3}$ ),

$R$  is the gas constant ( $\text{J kg}^{-1} \text{K}^{-1}$ ), and

$T$  is temperature (K).

Holding pressure constant, cooler temperatures, and thus cooler potential temperatures, imply more dense air and thus negative buoyancy. The second force is approximated by term  $b$ . This is the precipitation loading term, or the negative acceleration on the mass of both liquid water and ice. The last term,  $c$ , is due to the effects of vertical pressure perturbation on the mass of the air. This term is significant whenever the hydrostatic balance is disturbed, as is generally the case in thermal convection.

**3.1.3 Radar Theory.** Radar (Radio Detection and Ranging) converts electrical energy into electromagnetic energy. Electromagnetic energy is composed of both electrical and magnetic fields oscillating sinusoidally, in phase, but normal to each other. Electromagnetic fields are usually described by their frequency or wavelength. The frequency refers to the number of cycles an

electromagnetic wave experiences per second, expressed in Hertz (Hz). The wavelength of a wave is the distance between two successive crests or troughs, or the distance required for a wave to undergo a  $2\pi$  phase change; see Figure 5 (Rinehart, 1991:33).

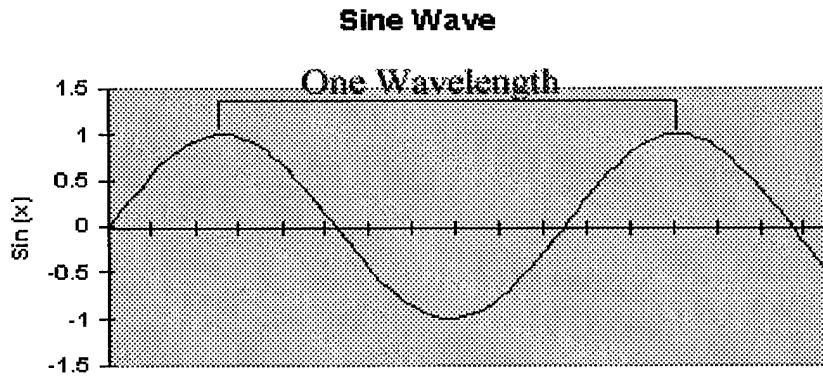


Figure 5. Sine Wave

Wavelength and frequency are related through the following relationship:

$$f = \frac{c}{\lambda} \quad (21)$$

where

$f$  is frequency (Hz),

$c$  is the speed of light in vacuum ( $\text{m s}^{-1}$ ), and

$\lambda$  is the wavelength (m).

NEXRAD uses a wavelength of approximately 10 cm ( $10^{-2}$  m). The inverse of the frequency is the period, the amount of time required for a single wave to be transmitted.

In addition to being characterized by wavelength or frequency, a radar is designated by its polarization. The polarization of a radar refers to the plane the electrical field oscillates in. Radar polarization is generally linear or circular.

Linear polarization implies the plane in which the electrical field oscillates remains fixed in time. A linearly polarized radar is typically either horizontally or vertically polarized. Most conventional weather radars and the NEXRAD are linearly horizontal polarized (NWS, 1990:7,8).

A circularly polarized radar beam uses an electrical field that rotates around the axis of the direction of propagation. Circularly polarized radars generally estimate the amount of water in a sample volume better than linearly polarized radars. Also, circularly polarized beams are more efficient energy users; however, circularly polarized electromagnetic energy suffers from significant attenuation, signal loss, when sampling raindrops with large diameters (NWS, 1990:8).

3.1.3.1 Radar Reflectivity. Whenever electromagnetic energy interacts with matter some of the energy is absorbed and some is scattered. The specific behavior of this interaction is governed by the characteristics of the matter and wavelength of the electromagnetic energy. If the particle diameter is small relative to the wavelength,  $diameter/\lambda < 0.1$ , the Rayleigh approximation for backscattering applies (Ray, 1986:89; Rinehart, 1991:51).

$$\sigma = \frac{\pi^5 \cdot (|K|)^2 \cdot D^6}{\lambda^4} \quad (22)$$

where

$\sigma$  is the backscatter cross section area ( $m^2$ ),

$K$  is a constant determined from the complex index of refraction of the material (0.93 for water),

$D$  is the diameter of the particle (m), and

$\lambda$  is the wavelength of the electromagnetic wave (m).

This is the area 'visible' to a particular wavelength of electromagnetic energy; thus, the amount of energy scattered back towards the emitter is proportional to the 6<sup>th</sup> power of the particle diameter.

Radars use a parabolic shaped antenna to focus electromagnetic energy. This focusing results in an increase in energy density. The ratio of the energy density with the antenna to that of

an isotropic emitter/receiver is termed the gain (Ray, 1986:89; Rinehart, 1991:48). The effective area of an antenna is given by

$$A_e = \frac{g\lambda^2}{4\pi} \quad (23)$$

where

$A_e$  is the effective antenna area ( $m^2$ ), and

$g$  is the gain (dimensionless) (Rinehart, 1991:50).

When a radar emits electromagnetic energy and the Rayleigh approximation applies, the power received at the radar is given by

$$p_r = \frac{p_t g l A_t A_e}{16\pi^2 r^4} \quad (24)$$

where

$p_r$  is the power received (Watts),

$p_t$  is the power transmitted (Watts),

$l$  is the attenuation factor (dimensionless,  $\sim 1.0$ ),

$A_t$  is the area of the target, comprised of numerous smaller targets ( $m^2$ ), and

$r$  is the range (m).

Since the interaction of electromagnetic energy for meteorological radars and targets falls into the Rayleigh regime, equation (24) can be simplified as

$$p_r = \frac{p_t g^2 \lambda^2 l \sum_i \sigma_i}{64\pi^3 r^4} \quad (25)$$

where

$\sigma_i$  is the back scattering cross-sectional area of the  $i^{\text{th}}$  particle ( $m^2$ ).

The power returned for weather radar is given by the sum of the back scattering cross-sectional areas in the volume sampled by each radar pulse. Accounting for a circular radar antenna and Gaussian shaped radar beam equation (25) is simplified as

$$P_r = \frac{p_i g^2 \lambda^2 1 \theta \phi h \sum_i \sigma_i}{1024 \ln(2) \pi^2 r^2} \quad (26)$$

where

$\theta$  is the vertical beam width (radians, 0.95 degree for NEXRAD),

$\phi$  is the horizontal beam width (radians, 0.95 degree for NEXRAD), and

$h$  is the pulse length (m).

This equation is also known as the Probert-Jones equation (Ray, 1986:89; Rinehart, 1981:64).

Defining the radar reflectivity factor as

$$z = \sum_i N_i D_i^6 \quad (27)$$

where  $N_i$  is the number of drops whose diameter is between  $D_i$  and  $D_i + \delta D_i$ , equation (27) can be simplified to

$$P_r = \frac{\pi^3 p_i g^2 \theta \phi (|K|)^2 1z}{1024 \ln(2) \lambda^2 r^2} \quad (28)$$

which is the general radar equation for any radar target system that meets the Rayleigh criteria (Rinehart, 1991:66).

Generally, when applying this equation operationally all variables in equation (28) are known except  $z$ , radar reflectivity factor. Solving for  $z$  in equation (28) for meteorological targets typically yields values of  $10^{-2} \text{ mm}^6 \text{ m}^{-3}$  to  $10^6 \text{ mm}^6 \text{ m}^{-3}$ . To ease the operational application of the radar reflectivity factor, a logarithmic scale is used in which  $z$  is normalized by  $1 \text{ mm}^6 \text{ m}^{-3}$ . This new factor is  $Z$  and is defined as

$$Z = 10 \cdot \log_{10} \left( \frac{Z}{1 \text{ mm}^6 \text{ m}^{-3}} \right) \quad (29).$$

Using this new parameter the reflectivity returns of meteorological targets are expressed in dBZ, or decibels relative to  $1 \text{ mm}^6 \text{ m}^{-3}$  (Rinehart, 1991:70).

3.1.3.2 Doppler Derived Velocity. The Doppler shift is the change in frequency of electromagnetic energy a moving object will produce relative to a stationary object. In other words, the frequency shift measured is related to the velocity of the target. Using this shift in frequency, Doppler radar can determine the radial velocity of a target. In order to measure the changes in frequency, Doppler radar must send out multiple radar pulses. The rate at which these pulses are emitted is called the Pulse Repetition Frequency (PRF), given in number per unit time.

The initial phase of an emitted electromagnetic wave is known and the phase upon returning from a target is measured. By repeating this process several times over a short period, the change in phase between the returning signals can be computed. The rate of change in phase with respect to time is the angular frequency

$$\omega = \frac{d\phi}{dt} \quad (30)$$

where

$\omega$  is angular frequency ( $\text{rad s}^{-1}$ ) and

$d\phi/dt$  is the time rate of change of phase ( $\text{rad s}^{-1}$ ).

Angular frequency ( $\omega$ ) and frequency ( $f$ ) are related by

$$\omega = 2\pi f. \quad (31)$$

The distance an electromagnetic wave must travel to and back from a target is  $2r$  where  $r$  is the range from the emitter to the target. Dividing the  $2r$  distance by  $\lambda$  gives the number of wavelengths from emitter to target to emitter. Recall that there are  $2\pi$  radians in one wavelength; therefore, the

product of  $2r/\lambda$  and  $2\pi$  gives the distance from emitter to target to emitter in radians. The velocity of an object is defined as the time rate of change of position or

$$V = \frac{dr}{dt} \quad (32)$$

where  $V$  is velocity. Furthermore, the time rate of change of phase is

$$\frac{d\phi}{dt} = \frac{d}{dt} \left( \frac{2\pi \cdot 2r}{\lambda} \right) = \frac{4\pi}{\lambda} \cdot \frac{dr}{dt} \quad (33)$$

Combining equations (31), (32), and (33) and simplifying yields

$$V = \frac{f\lambda}{2} \quad (34)$$

Velocity can easily be solved for knowing  $\lambda$  and measuring the shift in  $f$ . Using this principle Doppler radar measures the shift in frequency from several returns to determine the velocity of a target (Ray, 1986:93; Rinehart, 1991:74-75). Since only phase shifts  $\leq \pi$  radians are discernible, the maximum velocity measurable is restricted by

$$V_{\max} = \frac{\text{PRF} \cdot \lambda}{4} \quad (35)$$

where  $V_{\max}$  is the maximum unambiguous velocity ( $\text{m s}^{-1}$ ).  $\pm V_{\max}$  is called the Nyquist interval.

The inverse of the PRF is the interval between pulses. Recalling that distance is the product of velocity and time, the maximum distance an electromagnetic wave can travel before the

next pulse is  $d = \frac{c}{\text{PRF}}$ , where  $d$  is distance (m). The maximum range a radar could

unambiguously measure is half this distance, accounting for emit, backscatter, and receive. The maximum range is thus related to the PRF by

$$r_{\max} = \frac{c}{2 \cdot \text{PRF}} \quad (36)$$

where  $r_{\max}$  is the maximum range (m). Combining equations (35) and (36) leads to equation (13)

$$V_{\max} \cdot r_{\max} = \frac{\lambda c}{8}, \text{ the 'Doppler Dilemma'.$$

Recall from Chapter 2 that the 'Doppler Dilemma' states that an increase in the maximum resolvable velocity comes at the expense of a decrease in the maximum range of the radar, and vice versa as can be seen from equation (13).

### 3.2 Identification of Microbursts

Following several consultations with AETC AOS/AOW an agreement was achieved regarding the scope of research to be conducted. AETC originally requested exploration of microburst forecasting techniques for the U.S. that incorporated NEXRAD as a primary forecast tool. This topic was deemed too broad given the differences between geography and associated wet or dry microbursts. Priority was given to developing wet microburst forecasting techniques for the Southeast.

The geographic region considered in this study included Mississippi, Alabama, Georgia, South Carolina, and Florida north of Gainesville or approximately 29° North. This region includes the following AETC installations: Columbus AFB, Maxwell AFB, Keesler AFB, and Tyndall AFB. Other major military installations in this region supported by Air Force forecasters are Eglin AFB, Moody AFB, Ft McPherson AIN, Ft Stewart AIN, Ft Benning AIN, and Charleston AFB. This grouping ensured all microbursts occurred in a geographic region with similar topography and summertime climates. These summer climates are characterized by high surface humidity, infrequent frontal passage, and moderate, widespread convective instability.

The occurrence of high surface winds associated with supercells and squall lines due to frontal passage and tropical storms are understood to be an inherent part of these phenomena. Much less is understood about microbursts associated with airmass thunderstorms, and it is here



that the abilities of operational forecasters are most taxed. For this reason research was restricted to thunderstorms without synoptic forcing occurring during the hours 1100-0500 UTC, from 1 June - 31 August.

The final consideration included was the availability of NEXRAD data. To ensure adequate radar coverage of microburst-producing thunderstorms, research was limited to 1994 - present. Few NEXRAD systems were operational in the Southeast prior to 1994.

3.2.1 Screening of Surface Observations. During projects NIMROD, JAWS, and MIST a set of six simultaneous criteria were used to screen surface observations recorded by the PAMs to identify microburst events; see Appendix B (Fujita, 1985:54; Wakimoto, 1985:1133). During these studies, observations were recorded every minute by up to 71 stations only kilometers apart. Synoptic observations, on the other hand, are only recorded once an hour unless a specified criterion warranting additional observations is met. Observation sites are generally spaced on order of 100 km apart. For the region studied here there were only 54 observing stations. Table 3 highlights the differences between observation networks of NIMROD, JAWS, MIST and this thesis.

**Table 3. Comparison of Observation Networks (Fujita, 1985; Wakimoto, 1988)**

Project	Number of Stations	Station Spacing	Observation Freq.	Area of Coverage	Number of Radars
MIST	71	~ 2 km	60 hr <sup>-1</sup>	~ 1610 km <sup>2</sup>	5
JAWS	27	~ 2km	60 hr <sup>-1</sup>	~ 1350 km <sup>2</sup>	3
NIMROD	27	~ 4 km	60 hr <sup>-1</sup>	~ 6790 km <sup>2</sup>	3
Thesis	54	~ 100 km	1 hr <sup>-1</sup>	~ 560000 km <sup>2</sup>	14

To initially screen all surface observations from the synoptic network the criteria used in JAWS, NIMROD, and MIST were modified to the following 6 criteria:

1. A wind gust or peak wind  $\geq 35$  kts.
2. Wind gust or peak wind  $\geq 125\%$  of the three hour mean before wind gust or peak wind.
3. Wind gust or peak wind  $\geq 125\%$  of the three hour mean after wind gust or peak wind.
4. Wind gust or peak wind  $\geq$  the three hour mean before wind gust or peak wind plus 10 kts.
5. Wind gust or peak wind  $\geq$  the three hour mean after wind gust or peak wind plus 10 kts.
6. Wind gust or peak wind lasted less than 10 minutes.

The first criterion attempts to isolate only significant wind events. Initially the requirement for this criterion was  $\geq 20$  kts; however, this led to over 1600 data matches from the available 450,000 surface observations. Further refinement of this criterion to 35 kts reduced the number of data matches to fewer than 200. This refinement was also appropriate since the Air Force criteria for a moderate thunderstorm are winds  $\geq 35$  kts and/or hail less than 0.75 inches. Criteria 2 through 5 attempt to ensure the maximum wind event was a sudden and isolated event and not associated with a larger scale synoptic event. The final criterion attempts to restrict data hits to only events with short lifespans, since by definition microbursts last 10 minutes or less (Fujita, 1985:8).

3.2.2 Reduction of Sample Size. Using these six criteria over the designated geographic region, for the hours 1100-0500 UTC, during the months of June, July, and August, for the years 1994 - 1997 yielded 186 data matches. Each datum match indicated a possible microburst event. Next, eliminating all data matches that repeated a previously noted event slimmed the sample size down to 132 distinct events. Each of these were cross-checked with their corresponding observation to determine if a thunderstorm was present at the time of the event.

The primary tool available to the operational forecaster is the NEXRAD; therefore, research was restricted to only those events occurring within a 16-80 nautical mile (29.6-148.2 km) window of a Radar Data Acquisition (RDA) site were included. Using a programmed formula in the database the distance from the radar to the event location was

computed, and all events outside of the 16-80 nautical mile (29.6-148.2 km) window were discarded. Examining only storms within this distance interval maximized the volume of the storm interrogated. This left only 70 events to be investigated.

To ensure only airmass thunderstorms were considered, each possible microburst event was cross checked with the 0700 EST surface analysis from *Daily Weather Maps* (see Appendix C) for the date in question. Given the generally slower speeds of synoptic features during the summer, the author felt any event that occurred within 100 miles of the 0700 EST position of a surface front, cyclone, or tropical storm should be discarded as synoptically forced. This left only 49 events to be investigated.

Finally, all events for which no archive level II data was available were eliminated. An online search of the database at the National Climatic Data Center (NCDC) reduced the sample size to 18 events; however, three of the cases listed as available were not, and the final sample size was reduced to 15 radar cases. Vertical soundings were available for 39 cases.

### 3.3 Radar and Thermodynamic Variables

Following an extensive literature review, 28 variables related to microbursts were selected for study and possible inclusion into a forecasting technique. Of the 28 variables, 14 are radar derived and 14 are derived from vertical atmospheric soundings. Tables 4 and 5 highlight these variables, their relationship to microburst processes, and whether they are radar or sounding derived respectively.

**Table 4. Radar Microburst Variables Studied**

<b>Parameter</b>	<b>Relationship</b>
Maximum dBZ of storm	Presence of ice, hail, or large rain drops
Maximum height of the 50 dBZ central core	Past studies have indicated that microburst producing storms typically had core heights greater than non-microburst storms on the same day
Descent rate of storm core	Past studies have indicated that rapidly descending storm cores are frequently observed with microbursts
Time of core impact	Past studies have indicated the location and time of core impact relate to the location and strength of microbursts
Height of maximum convergence	Possibly an indicator of the initiation of entrainment of dry low $\theta_e$ air into the storm core
Time of maximum mid level convergence	Past studies indicate this is a possible precursor to microbursts
Convergence	Prior studies have indicated a close correlation between the magnitude of mid level convergence and microbursts
Rotation near cloud base	Indicator of a mesocyclone and more intense microburst
Intensity/Presence of storm top divergence	Often accompanies mid level convergence
Reflectivity notch near mid levels of storm	Indicator of low $\theta_e$ air entrainment
Maximum echo top	Used in VIL/TOP technique to predict microburst intensity
Maximum VIL value	Used in VIL/TOP technique to predict microburst intensity
Aspect ratio (depth of 50dBZ core to width of 50 dBZ core)	Used in Wolfson's technique to predict microburst intensity
Weak echo trench	Possible indicator of dry air entrainment

**Table 5. Sounding Microburst Variables Studied**

<b>Parameter</b>	<b>Relationship</b>
Height of the melting level	Higher melting levels may imply greater release of latent heat of fusion
Surface $\theta_e$ value	Used to compute $\Delta\theta_e$ values
Minimum mid level $\theta_e$	Used to compute $\Delta\theta_e$
$\Delta\theta_e$	Previous research indicates microbursts only occur on days where $\Delta\theta_e \geq 20$ K
Convective Available Potential Energy (CAPE)	Research by Atkins and Wakimoto indicated days with higher values were associated with days with a greater frequency of microbursts
Bulk Richardson Number (BRN)	Research by Atkins and Wakimoto indicated days with higher values were associated with days with a greater frequency of microbursts
Lifted Index (LI)	Research by Atkins and Wakimoto indicated days with higher values were associated with days with a greater frequency of microbursts
Depth of shear layer	Used in Rose's technique to predict microburst intensity
$\Delta$ wind speed at top of shear layer and bottom of shear layer	Used in Rose's technique to predict microburst intensity
Height of the transition level	Used in Rose's technique to predict microburst intensity
Average wind speed within shear layer	Used in Rose's technique to predict microburst intensity
Mean lapse rate up to 0°C isotherm level	Used in computing WINDEX to predict microburst
Mean mixing ratio in lowest 1 km	Used in computing WINDEX to predict microburst
Mixing ratio at the 0°C isotherm level	Used in computing WINDEX to predict microburst
Maximum mixing ratio	Used in computing WINDEX to predict microburst

### 3.4 Data Collection Equipment

Radar data was collected using the NEXRAD Radar Data Acquisition (RDA) sites located at the following locations: Jackson, Mississippi; Birmingham, Alabama; Mobile, Alabama; Atlanta, Georgia; Warner Robins, Georgia; Jacksonville, Florida; and Charleston, South Carolina. The collected data was digitized, and raw radar signal was stored at the RDA. This data was

forwarded to NCDC for storage. This data is then available for use by researchers and operational personnel. Once the required data was identified from the NCDC database it was transferred to 8 mm data tape and sent to AFIT.

Upper air soundings were collected using standard National Weather Service rawinsondes launched from the following upper air observation stations: Athens, Georgia; Atlanta, Georgia; Tallahassee, Florida; Jacksonville, Florida; Charleston, South Carolina; Slidell, Louisiana; and Jackson, Mississippi. These rawinsondes, composed of a balloon and instrument package, directly measure temperature, moisture, and pressure in the vertical. Horizontal wind direction and speed are inferred based on the movement of the rawinsonde. Vertical heights are computed using the time of release and known ascent rate of the instrument package. The measured variables are then transmitted back to the observation site where it is coded, transmitted, stored and disseminated. The soundings for time and observation site closest to the event occurrence were requested from AFCCC and sent to AFIT as ASCII format files on a 3.5" floppy diskette.

### 3.5 Data Processing

Once the archive level II data and raw code from the rawinsonde soundings were received extensive data processing was required. Radar data analysis was accomplished using the WATADS software mentioned in Chapter one. Analysis of vertical soundings was accomplished using a Fortran program written by the author (see Appendix D), the skew-T plotting program SHARP, and plots of equivalent potential temperature vs. pressure using Mathcad®.

3.5.1 Analysis of Radar Data. The WATADS software operates on a Sun Sparc® 20 workstation. WATADS, developed by the National Severe Storms Laboratory, uses archive level II data to simulate a real-time NEXRAD Primary User Position. The program allows the user to select which algorithms to use, and define data ranges and default settings. Since one of the goals of the research was to develop a technique for operational forecasters to predict microbursts, only

standard algorithms from build 9.0, the current software version on operational NEXRAD's, were used. Once all of the available cases were loaded onto the workstation hard-drives, each case was investigated extensively and the radar variables outlined in Table 4 were recorded onto a worksheet designed by the author (see Appendix E).

The first step in analyzing the radar data was to identify which cell was responsible for producing the recorded microburst. By knowing where the point of observation was located, a zoomed in time-lapse, combined with algorithm designated cell id's, identified the parent storm cell. All radar variables measured and recorded on the worksheet were from this parent cell.

One of the features of WATADS is the ability of the user to set the data range. Using the composite reflectivity product, combining the ability to change the range values for radar reflectivity, and examining the volume scans before, during, and immediately after the microburst, the maximum dBZ of the parent storm was observed. The time of the occurrence of the maximum radar reflectivity was also recorded. The maximum vertically integrated liquid (VIL) value of the parent storm was similarly observed and recorded.

Previous studies have established a 50 dBZ criterion for a storm core producing a microburst. Using this criterion, the maximum displayed value for radar reflectivity was set to 50 dBZ. Then, the maximum height of the central core and the times of occurrence were measured taking a series of radar cross-sections of the parent storm core during its evolution. Using this series of cross-sections the change in height per volume scan, one every 5 - 6 minutes, was used to determine the descent rate of the core and estimate the time of core impact. The core aspect ratio, the ratio of the core width to height, was computed by estimating the ratio of horizontal bins to the number of vertical bins in the cross-section used to determine the height of the central core.

To determine the height of maximum mid-level convergence, base velocity products for several layers during each volume scan were selected for study. Using WATADS' ability to

display several panels at once, these levels were displayed simultaneously and examined for convergent velocity fields. The data fields were displayed to the precision of one knot (to be converted to  $\text{m s}^{-1}$ ) by changing the data range for velocity. The radar displays the height where the cursor is located. The height of the maximum convergence, number of bins where convergence occurred, and maximum inbound/outbound velocities were measured by using this feature and visually selecting the velocity field with the maximum convergent velocities. These values were then recorded onto the worksheet. The length of the bins is approximately 470 m. The product of the number of convergent bins and this length yields  $\Delta r$ . Dividing the absolute value of the difference of the maximum convergent winds by the radial distance,  $\Delta V/\Delta r$ , yielded the approximate magnitude of the convergence. Storm top divergence was similarly computed for the upper levels of the parent storm.

To determine the presence of rotation near the storm base, base velocity fields for the lowest 4 levels of the volume scans preceding the microburst were displayed in the multi-panel format. These velocity fields were then evaluated for the presence of rotation. If rotation was observed the time of occurrence and maximum inbound/outbound velocities were recorded.

To determine the presence of a reflectivity notch near the mid-levels of the storm, base reflectivities for several levels were displayed in a multi-panel format. This view is similar to the Plan Position Indicator view used in previous radars and used in previous microburst studies. If a reflectivity notch was observed its time of occurrence was noted.

The top of a storm was defined as 10 dBZ or less. Using base reflectivity products for the upper levels of the storm, and cross-section views the top of the parent storm in 100's feet was recorded. The time of occurrence of the maximum storm top was likewise recorded.

The last feature evaluated was the presence of a weak echo trench in the radar cross-sections. This feature was not originally established as a possible microburst precursor; however,



after it was observed in two cases early into the analysis, this feature was studied for all cases. Using a series of vertical cross-sections of the parent storm during its evolution, the presence of a weak echo trench was determined and its approximate height and time of occurrence was recorded.

3.5.2 Analysis of Upper Air Data. The vertical sounding data provided by AFCCC was raw rawinsonde code downloaded onto 3.5" floppy diskette. In this form it was not user friendly or readily useable by SHARP or Mathcad<sup>®</sup>. To modify the sounding code to a useable format the author devised a Fortran program called Read (see Appendix D). To ready the rawinsonde code to a format readable by Fortran 77, not exceeding 72 characters per line, manual returns were inserted where appropriate. Read was used to read the rawinsonde code, determine the temperature, pressure, height, dewpoint depression, wind direction and speed. Read computed dewpoint temperature, vapor pressure, mixing ratio, potential temperature, and equivalent potential temperature at each level. The output from Read was then placed in column format in a designated output file to be used by SHARP and Mathcad<sup>®</sup>. In an effort to keep the research operationally focused the most recent sounding that would be available to operational forecasters was used. This meant using the sounding closest to the time of the microburst, unless the sounding was taken less than one hour prior to the microburst. As with the radar variables studied a worksheet was devised to record the values of the sounding variables for each sounding studied (see Appendix F).

Convective Available Potential Energy (CAPE), Bulk Richardson Number (BRN), and Lifted Index (LI) were all computed using SHARP, a research oriented skew-T plotting program on a Sun Sparc<sup>®</sup> 20 workstation. These instability parameters for each sounding were computed using the mean moisture present in the lowest 100 hPa. Once calculated these values were recorded on the sounding worksheet for the appropriate sounding.

All other sounding variables were determined by examining the column formatted data written to the output files, as computed by Read. The height of the melting level was determined

by locating the height value corresponding to 273 Kelvin. The minimum  $\theta_e$  value was determined by examining the equivalent potential temperature column, selecting the minimum value, and recording this value and its height. The  $\Delta\theta_e$  value was calculated by subtracting the minimum  $\theta_e$  value from the maximum  $\theta_e$  value from the lowest 100 hPa, which was then recorded onto the worksheet. The shear layer was defined as the depth at which winds cease to display large increases with height (Rose, 1996:14). Using this definition, the wind speed column for each sounding was examined and the height where the wind speed initially reached a maximum before decreasing in value was determined to the depth of the shear layer. This depth was then recorded for each sounding. The  $V_d$  value was determined by calculating the difference between the base and top of the shear layer. The shear layer average  $V_{avg}$  for each sounding was determined by summing the measured wind speeds in the shear layer and dividing by the number of recorded values. The distance from the upper air observation site to the location where the microburst was observed was calculated using the same formula used in the radar worksheet. The lapse rate from the surface to the 0° C isotherm was determined as follows. First, subtract 273.15 K from the surface temperature. Next, divide this difference by the height of the freezing level. This yields the lapse rate from the surface to the melting level. The transition level, the level AGL where the sounding becomes neutral or stable, was determined as follows. Starting with the lowest two sounding levels the lapse rate between the two levels was calculated. This process continued for the subsequent sounding levels until a lapse rate between the dry and moist lapse rates, 9.8 deg/km and 4.3 deg/km respectively, was found. The lowest of the two levels was established as the height of the transition level. This procedure continued for each sounding. The last three variables to be examined all regarded the mixing ratio. The first variable was the mean mixing ratio in the lowest kilometer. The mixing ratios calculated for each level within the lowest kilometer were summed and this sum was divided by the number of levels observed, yielding the mean mixing ratio in the

lowest kilometer. The mixing ratio at the melting level and the maximum mixing ratio were simply a matter of selecting the appropriate value from the column of mixing ratio values.

3.5.3 Calculation of Microburst Intensity Predictors. Once the radar and sounding worksheets had been completed the four microburst intensity predictors could be calculated. To determine the values of each predictor, the four corresponding predictive equations were programmed into Mathcad® as functions. Following this, the appropriate values for each variable were inserted into the correct function, if applicable, and the predicted outflow speed resulted. The results of these calculations were placed into a spreadsheet for comparison to the other techniques and the observed wind speed. A statistical analysis was then performed to determine which technique performed best.

### 3.6 Development of Proposed Technique

The development of an operational forecasting technique proceeded in three stages. First, distinguish the environment favorable for microburst formation from that not favorable. This would allow the forecaster to identify, before the initiation of convection, which days microbursts pose a threat to operations. Second, provide a means for the forecaster to predict how severe those microbursts could be. Selecting the two best performing intensity predictors following the statistical analysis provides two competent estimators of microburst intensity. The severity of the expected microbursts could then be relayed to all concerned personnel, heightening awareness to the threat. Third, recognize the radar signatures that demonstrate the greatest potential as precursors to the operational forecaster. These precursors must fulfill two requirements: be easily recognized and reliable. Once the likelihood and intensity of microbursts for a given day have been established, attention could be focused on radar interrogation of storm cells. Following the occurrence of these precursors aviators in the vicinity of the event could be forewarned and take precautionary measures.

## IV. Data Analysis

### 4.1 Description of Data Set

The data set studied during this research included 41 microburst events from the period and region specified in Chapter 3. These 41 cases included 39 upper air soundings and 15 radar cases. Thirteen cases had both radar and upper air sounding data available. Two cases had radar data only, and 26 had sounding data only. This sample size is larger than those from some previous studies; Isaminger's study consisted of 34 cases, Rose's study consisted of 22 cases, and Stewart's study consisted of 13 cases.

4.1.1 Description of the Upper Air Data Set. A total of 39 upper air soundings were analyzed for the 14 thermodynamic variables outlined in Chapter 3. These soundings were taken from eight different observation locations from 1994 to 1997. Thirty-five of the soundings were taken at 1200 UTC, the morning sounding, and four at 0000 UTC, the evening sounding. The mean and median distance from the upper air observation site to the location where the microburst was recorded was 146.2 km and 137 km, respectively. The minimum distance from the upper air site to the observation site was 6 km and the maximum distance was 589 km. Upper air observations taken more frequently and closer to the point of the microbursts would have been better; however, given the current network of CONUS upper air observation locations, no other options were available.

4.1.2 Description of the Radar Data Set. A total of 15 radar observations were analyzed for the 14 radar variables outlined in Chapter 3. These radar observations were taken from seven different RDA sites in Mississippi, Alabama, Georgia, Florida, and South Carolina. The radar observations were taken from 1995-1997; no data were available prior to 1995. The mean and median distance from the RDA site to the location where the microburst was recorded was

90.6 km and 123 km respectively. The minimum distance from the radar site to the observation site was 29.8 km and the maximum distance was 146.7 km. Radar observations within a range window of 20-50 km would have given better resolution of low level features; however, given the fixed NEXRAD network no other options were available. Research quality radars or multiple radar analysis of the parent storms would have provided more stringent interrogation techniques, but since the focus is in operational application, using an operational radar was reasonable.

#### 4.2 Analysis of Thermodynamic Variables

Analysis of the 14 thermodynamic variables typically entailed three steps. First, determine the values of the sample mean, median, standard deviation, minimum, and maximum. Second, correlate the variable under study to the other variables and determine the corresponding P-values. The focus of the correlation work was on the observed wind speed. Third, determine the distribution of the variable and 95% confidence interval. The confidence interval will help forecasters identify values of the variables associated with microbursts. All of the variables followed a normal or lognormal distribution. Tables 6 and 7 below present the descriptive statistics for each of the thermodynamic variables and the correlations of the variables.

**Table 6. Descriptive Statistics of the Thermodynamic Variables**

	BRN		CAPE (J/kg)		Delta Theta-e (K)
Sample Size	39		39		39
Mean	689.9		1369		25.1
Median	661.6		1115.3		24.5
Standard Deviation	3005.5		1104.2		8.9
Variance	9.0E+06		1.2E+06		78.5
Minimum Value	0		0		9.3
Maximum Value	18495		4272.1		50.7
95% CI Upper and Lower	71.8,148.4		1011.0,1726.9		22.2,27.9
	Melting Level Height (m)		Theta-e Minimum Height (m)		Lapse Rate (deg/km)
Sample Size	39		39		39
Mean	4303.1		3507.4		5.3
Median	4300		3658		5.6
Standard Deviation	385.9		971.3		0.9
Variance	148948		943350		0.8
Minimum Value	3100		1483		4.2
Maximum Value	5000		6096		5.57
95% CI Upper and Lower	4178.0,4428.2		3192.6,3822.3		5.2,5.8
	Lifted Index		Maximum Mixing Ratio (g/kg)		Mean Mixing Ratio (g/kg)
Sample Size	39		39		39
Mean	-3.4		17.9		15.5
Median	-3		17.7		15.6
Standard Deviation	2.8		2.3		1.9
Variance	7.8		5.2		3.5
Minimum Value	-8.4		12.7		11.3
Maximum Value	3.3		25.7		20.5
95% CI Upper and Lower	-4.3,-2.5		17.1,18.6		14.9,16.1

	Depth of the Shear Layer (m)	Theta-e Minimum Temp (K)	Transition Level (m)
Sample Size	39	39	39
Mean	1075.2	321.9	844.7
Median	749	321.6	797
Standard Deviation	1008	5.5	392.5
Variance	1.0E+06	30.6	154081
Minimum Value	123	310	163
Maximum Value	4267	333.3	1855
95% CI Upper and Lower	748.4,1401.9	320.1,323.7	717.5,972.0
	0°C Isotherm Mixing Ratio	Microburst Speed (m/s)	
Sample Size	39	39	
Mean	4.2	20.4	
Median	4.6	18.5	
Standard Deviation	1.4	3.7	
Variance	1.9	14.0	
Minimum Value	1.4	18	
Maximum Value	6.5	31.9	
95% CI Upper and Lower	3.7,4.6	19.2,21.6	

**Table 7. Correlations and P-values of Thermodynamic Variables**

Corr P-value	BRN	CAPE (J kg <sup>-1</sup> )	Delta Theta-e (K)	Height Melting Level (m)	Height Theta-e Min (m)	Lapse Rate (deg km <sup>-1</sup> )	Lifted Index	Max Mixing Ratio	Mean Mixing Ratio	Depth Shear Layer (m)	Theta-e Min Temp (K)	Transition Level (m)	0°C Mixing Ratio	Microb urst Speed (m s <sup>-1</sup> )
BRN		0.354 0.032	0.343 0.038	0.114 0.501	0.071 0.678	0.146 0.389	-0.350 0.034	0.239 0.154	0.238 0.155	0.118 0.485	-0.083 0.625	-0.312 0.060	-0.268 0.108	-0.071 0.676
CAPE (J kg <sup>-1</sup> )	0.354 0.032		0.511 0.001	0.004 0.981	0.247 0.130	0.153 0.349	-0.849 0.000	0.475 0.002	0.648 0.000	-0.091 0.584	-0.058 0.728	-0.268 0.099	-0.207 0.207	0.231 0.156
Delta Theta-e (J kg <sup>-1</sup> )	0.343 0.038	0.511 0.001		0.072 0.664	-0.105 0.523	0.350 0.029	-0.452 0.004	0.803 0.000	0.685 0.000	-0.114 0.489	-0.402 0.011	-0.249 0.127	-0.439 0.005	0.080 0.627
Height Melting Level (m)	0.114 0.501	0.004 0.981	0.072 0.664		0.066 0.690	-0.362 0.024	0.132 0.422	0.334 0.038	0.304 0.060	0.019 0.911	0.561 0.000	0.120 0.468	-0.104 0.528	0.081 0.624
Height Theta-e Min Temp (m)	0.071 0.678	0.247 0.130	-0.105 0.523	0.066 0.690		0.035 0.831	-0.252 0.121	-0.023 0.890	0.035 0.831	0.073 0.661	0.185 0.260	0.115 0.485	-0.139 0.398	-0.227 0.164
Lapse Rate (deg km <sup>-1</sup> )	0.146 0.389	0.153 0.349	0.350 0.029	-0.362 0.024	0.035 0.831		-0.151 0.359	0.240 0.141	0.227 0.165	-0.277 0.088	-0.058 0.725	0.057 0.730	0.004 0.980	0.191 0.244
Lifted Index	-0.350 0.034	-0.849 0.000	-0.452 0.004	0.132 0.422	-0.252 0.121	-0.151 0.359		-0.361 0.024	-0.509 0.001	-0.006 0.973	0.157 0.340	0.231 0.156	0.293 0.070	-0.216 0.186
Max Mixing Ratio	0.239 0.154	0.475 0.002	0.803 0.000	0.132 0.422	-0.023 0.890	0.240 0.141	-0.361 0.024		0.859 0.000	-0.253 0.120	0.122 0.458	-0.155 0.346	-0.239 0.143	0.141 0.393
Mean Mixing Ratio	0.238 0.155	0.648 0.000	0.685 0.000	0.334 0.038	0.035 0.831	0.227 0.165	-0.509 0.001	0.859 0.000		-0.204 0.214	0.201 0.221	-0.097 0.556	-0.177 0.280	0.227 0.164
Depth Shear Layer (m)	0.118 0.485	-0.091 0.584	-0.114 0.489	0.304 0.056	0.073 0.661	-0.277 0.088	-0.006 0.973	-0.253 0.120	-0.204 0.214		-0.091 0.583	0.231 0.157	-0.146 0.376	-0.219 0.180
Theta-e Min Temp (K)	-0.083 0.625	-0.058 0.728	-0.402 0.011	0.019 0.911	0.185 0.260	-0.058 0.725	0.157 0.340	0.122 0.458	0.201 0.221	-0.091 0.583		0.203 0.216	0.342 0.033	0.209 0.202
Transiti on Level (m)	-0.312 0.060	-0.268 0.099	-0.249 0.127	0.561 0.000	0.115 0.485	0.057 0.730	0.232 0.156	-0.155 0.346	-0.097 0.556	0.231 0.157	0.203 0.216		0.105 0.526	0.042 0.798
0°C Mixing Ratio	-0.268 0.108	-0.207 0.207	-0.439 0.005	0.120 0.468	-0.139 0.398	0.004 0.980	0.293 0.070	-0.239 0.143	-0.177 0.280	-0.146 0.376	0.342 0.033	0.105 0.526		0.126 0.442
Microb urst Speed (m s <sup>-1</sup> )	-0.071 0.676	0.232 0.156	0.080 0.627	0.081 0.624	-0.227 0.164	0.191 0.244	-0.216 0.186	0.141 0.393	0.227 0.164	-0.219 0.180	0.209 0.202	0.042 0.798	0.126 0.442	

4.2.1 Thermodynamic Variables with a Normal Distribution. The first step in determining the distribution of the n = 39 samples of melting level height (m) was to perform a Wilk-



Shapiro/Rankit plot to check for normality (see figure 6). Statistix<sup>®</sup> yielded a Wilk-Shapiro value of 0.9394, indicating a normal distribution provided an excellent fit. Figures 6 and 7 below illustrate the Wilk-Shapiro/Rankit plot and probability distribution function of the height of the melting level. The probability density function for the height of the melting level was determined to be normal with a  $\mu = 4303.1$  and  $\sigma = 385.9$ .

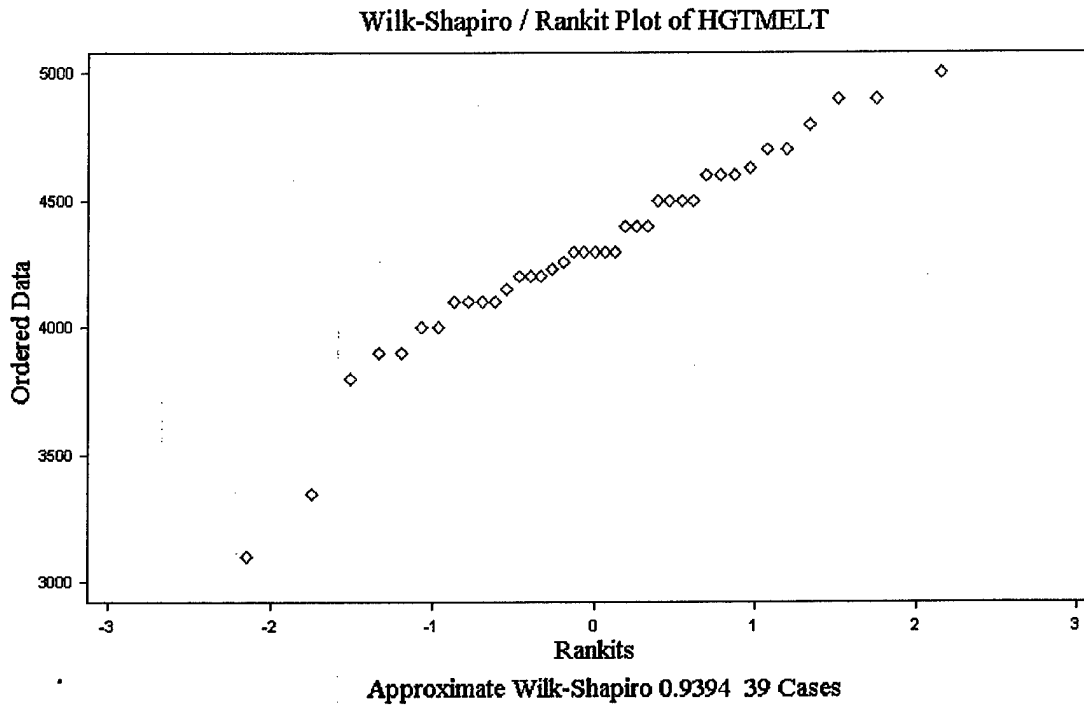


**Figure 6. Wilk-Shapiro Plot for the Height of the Melting Level.**

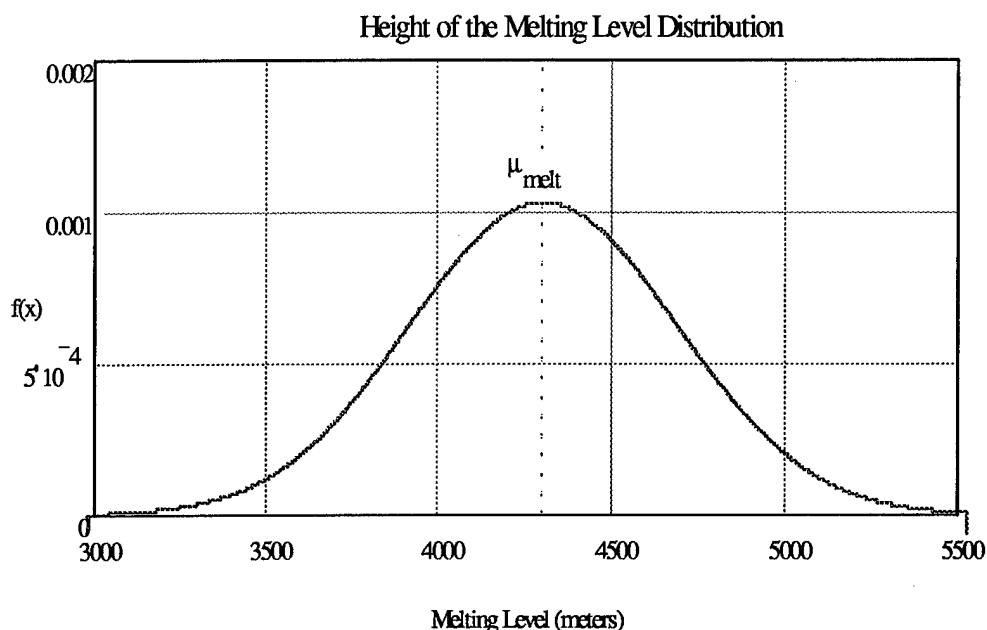


**Figure 7. Normal Probability Density Function for the Height of the Melting Level.**

The distributions of the minimum  $\theta_e$  (K), height of the minimum  $\theta_e$  (m),  $\Delta\theta_e$  (K), Lifted Index, mean mixing ratio ( $\text{g kg}^{-1}$ ), mixing ratio at the  $0^\circ\text{C}$  isotherm ( $\text{g kg}^{-1}$ ), and height of the transition level (m) were similarly determined to be normally distributed with their respective means and standard deviations as listed in Table 6.

**4.2.2 Thermodynamic Variables with a Lognormal Distribution.** Initial data plots of Convective Available Potential Energy, CAPE, ( $\text{J kg}^{-1}$ ) indicated a closely normal distribution for this variable. Using Statistix<sup>®</sup> a Wilk-Shapiro/Rankit plot was created, yielding a Wilk-Shapiro value of 0.9172.

Physical constraints prevent  $\text{CAPE} < 0$ ; therefore, a logarithmic transformation of CAPE was used yielding a Wilk-Shapiro value of 0.9211, indicating a lognormal distribution provided a better fit. The probability density function for CAPE was assumed to be lognormal with a

$\mu = 6.8$  and  $\sigma = 1.1$ . Figures 8 and 9 depict the Wilk-Shapiro/Rankit plot and probability distribution function of the CAPE values.

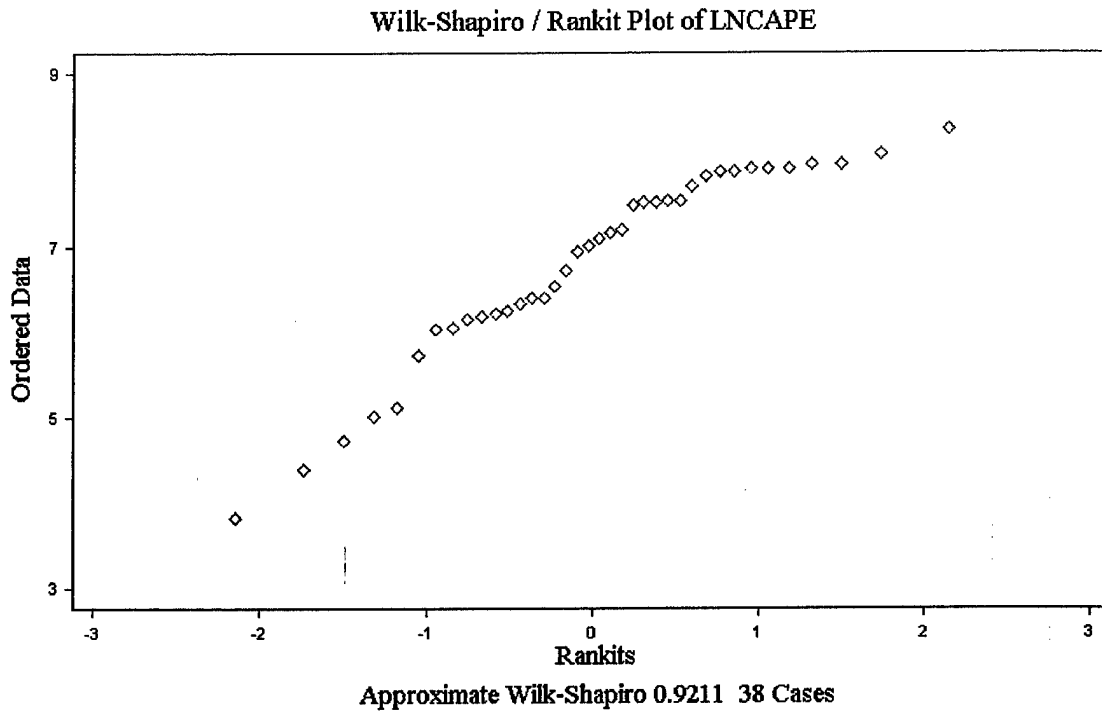


**Figure 8. Wilk-Shapiro Plot for LN(CAPE).**

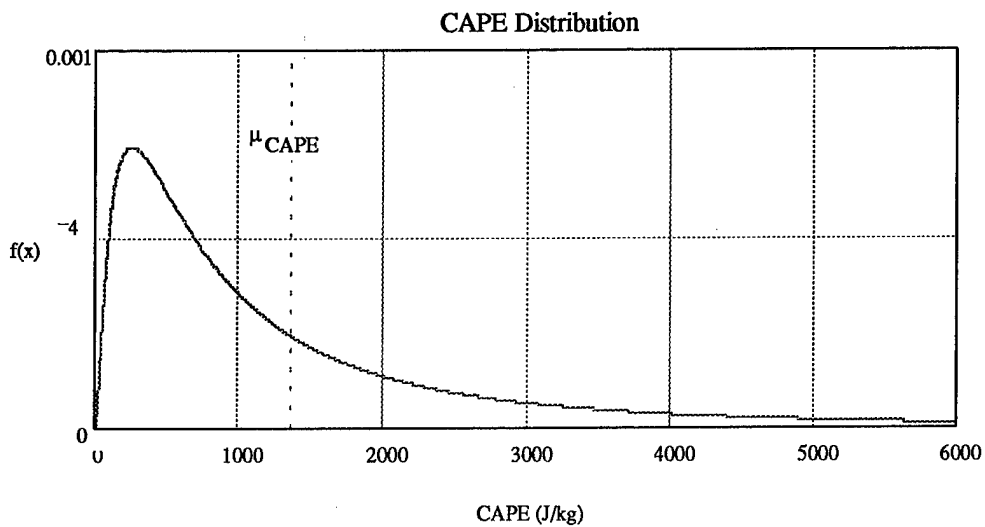


**Figure 9. Lognormal Distribution of Convective Available Potential Energy.**

The thermodynamic variables depth of the shear layer (m), lapse rate up to the 0°C isotherm and Bulk Richardson Number were similarly determined to be lognormally distributed with their respective means and standard deviations as listed in Table 6.

#### 4.3 Thermodynamic Regression Equation

The three most important physical factors influencing the development and evolution of a microburst are transfer of momentum/mass, thermodynamics or energy transfer, and buoyancy. Six of the thermodynamic variables studied, which incorporated these factors, were selected for inclusion in a non-linear regression equation to model microburst outflow speed. These variables were selected based on the ability of an operational forecaster to quickly and easily compute. The variables selected were the BRN, CAPE,  $\Delta\theta_e$ , height of the melting level, height of the  $\theta_e$  minimum temperature, and mean mixing ratio in the lowest 1 km. BRN is related to momentum transfer since it contains a shear term. CAPE is a measurement of potential energy per unit mass and often indicates how severe a thunderstorm might be.  $\Delta\theta_e$  is an indicator of how much evaporation could occur and is indirectly related to the latent heat release which acts to cool air in the mid levels of a microburst producing storm. The height of the melting level indicates the depth in which an ice particle would be subjected to melting and latent heat release. The height of the  $\theta_e$  minimum temperature gives an indication of the location where rapid evaporation is expected. The higher the  $\theta_e$  minimum the greater the distance over which a descending parcel may experience negative buoyancy and downward acceleration. The mean mixing ratio in the lowest 1km indicates how much water mass is present; greater quantities of mass are subject to greater momentum. Using a statistical analysis program called Data Fit<sup>®</sup> these six variables were set as the independent variables while microburst outflow velocity was set as the dependent variable. Data Fit<sup>®</sup> produced the following nonlinear regression equation.

$$V_{mb} = \exp(a \text{ BRN} + b \text{ CAPE} + c \Delta\theta_e + d \text{ Hgtmelt} + e \text{ Hgtmin}\theta_e + f \text{ Meanmix} + g) \quad (37)$$

where

$V_{mb}$  is the predicted outflow velocity ( $m\ s^{-1}$ ),

$a = 1.863E-5$ ,

$b = 1.8715E-5$ ,

$c = -0.003$ ,

$d = 3.064E-5$ ,

$e = -3.902E-5$ ,

$f = 0.019$ ,

$g = 2.744$ ,

BRN is the Bulk Richardson Number (non-dimensional),

CAPE is the Convective Available Potential Energy ( $J\ kg^{-1}$ ),

$\Delta\theta_e$  is the difference between the maximum  $\theta_e$  in the lowest 100 hPa and the minimum  $\theta_e$  in the mid levels (K),

Hgtmelt is the height of the melting level (m),

Hgtmin $\theta_e$  is the height of the minimum  $\theta_e$  (m), and

Meanmix is the mean mixing ratio in the lowest 1 km ( $g\ kg^{-1}$ ).

This regression equation was selected from the others produced by Data Fit<sup>®</sup> because it provided the largest  $R^2 = 0.299$ , where  $R^2$  is the amount of variation between the observed and predicted dependent variable that is explained by the regression model (Devore, 1995:489). For meteorological phenomena an  $R^2$  value between 0.2 and 0.5 is reasonable considering the highly non-linear nature of meteorological events. Table 8 presents an analysis of variance for equation (37).

**Table 8. Analysis of Variance for Equation (37)**

	Degrees of Freedom	Sum of Squares	Mean Square	F-value	P-value
Regression	6	373.163	62.194	2.271	0.066
Error	32	876.259	27.383		
Total	38	1249.422			

The next step in evaluating the adequacy of this regression model was to check the model usefulness and validity. This was accomplished by constructing three plots: a predicted vs. observed velocity plot, a residual plot, and a Wilk-Shapiro/Rankit plot of the residuals. These three plots are depicted below as figures 10, 11, and 12.

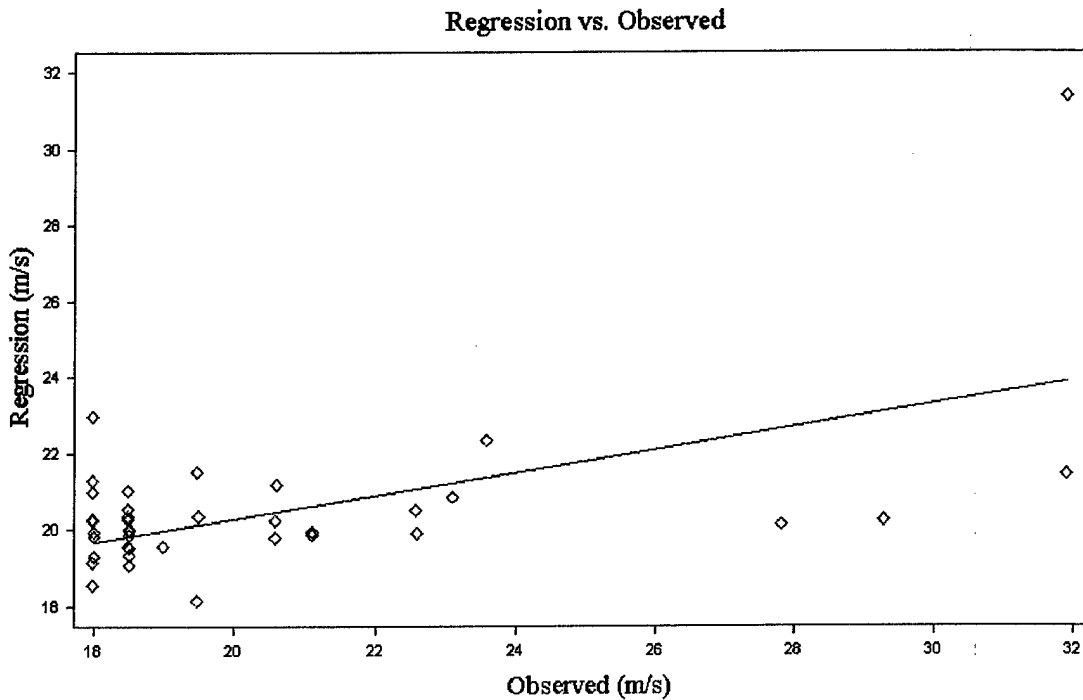


**Figure 10. Predicted vs. Observed Plot for Equation (37).**

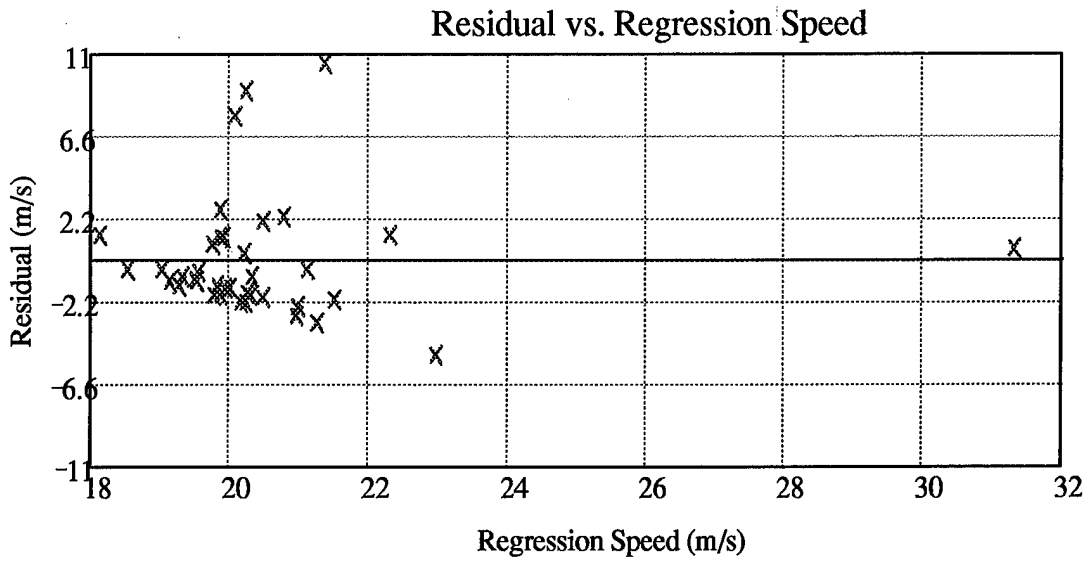


Figure 11. Residual Plot for Equation (37).

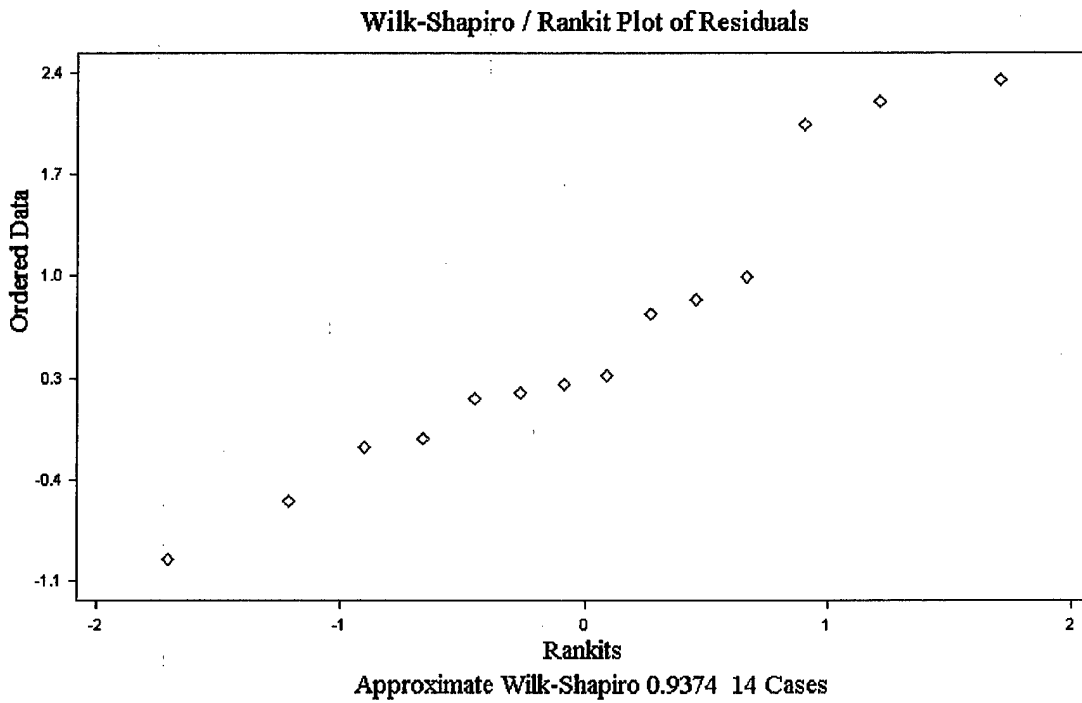


Figure 12. Wilk-Shapiro/Rankit Plot of the Residuals from Equation (37).

Assuming an ideal relationship, the regression line in figure 10 should demonstrate a slope of  $45^\circ$ ; for equation (37) the slope was  $19.5^\circ$ , indicating the model provides a good fit. The residual plot

depicted in figure 11 shows a slight fanning out of the residuals; however, given the smallness of the sample size, homoscedasticity, which is favorable for model aptness, can not be discounted. Figure 12 indicates a Wilk-Shapiro value of 0.9374, strongly arguing for a normal distribution of the residuals, which favors model aptness. These factors indicate equation (37) is not an ideal model, but is an apt model. Further support for model adequacy can be drawn from computed P-value of 0.066 which demonstrates that equation (37) does have statistical significance and is worthy of further exploration using a new data set.

#### 4.4 Analysis of Radar Variables

Analysis of the 14 radar variables proceeded in the same manner as with the thermodynamic variables. The three steps were: determine the values of the sample mean, median, standard deviation, minimum, maximum and confidence interval; correlate the variable under study to the other variables; and determine the distribution of the variable. Distributions were determined for 11 of the variables. The sample size of the heights of the weak echo trench and reflectivity notch were  $n = 6$ , too small to reliably determine a distribution, and the presence of rotation was noted as yes or no. Tables 9 and 10 present the descriptive statistics for each of the analyzed radar variables and the correlations of the variables. While the sample sizes for the radar variables fall short of the  $\approx 30$  sample size recommended for the Central Limit Theorem, the CLT can applied since the distributions of each of the analyzed variables are normal or lognormal (Devore, 1995:79).



**Table 9. Descriptive Statistics of the Radar Variables**

	Aspect Ratio		Convergence ( $s^{-1}$ )		Descent Rate ( $m\ min^{-1}$ )
Sample Size	15		14		15
Mean	0.6		3.8E-03		170.2
Median	0.5		3.7E-03		168
Standard Deviation	0.2		2.0E-03		69.8
Variance	0.04		4.0E-06		4871
Minimum Value	0.3		1.6E-03		61
Maximum Value	1.0		8.4E-03		320
95% CI Upper and Lower	0.4,0.7		2.6E-03,4.9E-03		131.6,208.9
	Height of the Central Core (m)		Height of the Echo Trench (m)		Height of Maximum Convergence (m)
Sample Size	15		6		14
Mean	5831.6		4763		2685.2
Median	6400		4724.5		2149
Standard Deviation	2438		691.0		1256.1
Variance	5.9E+06		477468		1.6E+06
Minimum Value	2134		3657		884
Maximum Value	9754		5486		5120
95% CI Upper and Lower	4481.5,7181.7		4037.8,5488.2		1959.9,3410.5
	Height of the Reflectivity Notch (m)		Maximum dBZ of the Parent Storm (dBZ)		Storm Top Divergence ( $s^{-1}$ )
Sample Size	6		15		12
Mean	3169.8		56.3		3.7E-03
Median	3200		57		2.9E-03
Standard Deviation	1855.8		4.4		2.3E-03
Variance	3.4E+06		19.7		5.5E-06
Minimum Value	1341		47		1.1E-03
Maximum Value	4968		62		8.4E-03
95% CI Upper and Lower	1222.3,5117.3		53.9,58.8		2.2E-03,5.2E-03

	Time Difference of Core Impact and Observed Wind Maximum (min)		Time Difference of Maximum Convergence and Observed Wind Maximum (min)		Maximum Storm Top (100's ft)
Sample Size	15		14		15
Mean	9.0		18.3		398.2
Median	8.0		19.5		399.0
Standard Deviation	6.9		7.3		70.0
Variance	48		53.8		4902.2
Minimum Value	-1.0		5.0		232.0
Maximum Value	20.0		30.0		500.0
95% CI Upper and Lower	5.2,12.8		14.1,22.5		359.4,436.9
	VIL ( $\text{kg/m}^2$ )		Microburst Speed ( $\text{m s}^{-1}$ )		
Sample Size	15		39		
Mean	24.5		20.4		
Median	23.0		18.5		
Standard Deviation	12.1		3.7		
Variance	146.1		14.0		
Minimum Value	5.0		18		
Maximum Value	45.0		31.9		
95% CI Upper and Lower	17.8,31.2		18.6,23.3		

**Table 10. Correlations and P-values of Radar Variables**

Corr	Aspect Ratio	Convergence (s <sup>-1</sup> )	Descent Rate (m min <sup>-1</sup> )	Height of the Central Core (m)	Height of Max Convergence (m)	Maximum dBZ	Storm Top Divergence (s <sup>-1</sup> )	Maximum Storm Top (TOP) (100 ft)	Max VIL	Δ Time Core Impact/Observed (min)	Δ Time Max Convergence/Obs Wind (min)	Microburst Speed (m s <sup>-1</sup> )
P-value												
Aspect Ratio		-0.385 0.174	-0.211 0.450	-0.408 0.131	0.277 0.338	-0.518 0.048	-0.027 0.934	-0.238 0.393	-0.248 0.373	0.305 0.269	0.096 0.744	-0.140 0.619
Convergence (s <sup>-1</sup> )	-0.385 0.174		-0.076 0.797	-0.049 0.867	-0.041 0.889	0.378 0.183	0.665 0.026	-0.082 0.782	0.217 0.457	-0.283 0.328	-0.232 0.424	0.498 0.070
Descent Rate (m min <sup>-1</sup> )	-0.211 0.450	-0.076 0.797		0.504 0.056	-0.098 0.740	0.189 0.500	-0.144 0.655	0.523 0.045	0.318 0.248	-0.198 0.480	0.219 0.453	0.104 0.713
Hgt of Central Core (m)	-0.408 0.131	-0.049 0.867	0.504 0.056		-0.326 0.256	0.699 0.004	-0.063 0.847	0.535 0.040	0.606 0.017	-0.454 0.089	0.553 0.040	0.135 0.633
Height of Max Convergence (m)	0.277 0.338	-0.041 0.889	-0.098 0.740	-0.326 0.256		-0.328 0.252	-0.434 0.183	0.281 0.331	-0.104 0.723	0.372 0.190	0.139 0.636	-0.093 0.752
Maximum dBZ	-0.518 0.048	0.378 0.183	0.189 0.500	0.699 0.004	-0.328 0.252		-0.055 0.865	0.216 0.440	0.867 0.000	-0.270 0.331	0.465 0.094	0.205 0.463
Storm Top Divergence (s <sup>-1</sup> )	-0.027 0.934	0.665 0.026	-0.144 0.655	-0.063 0.847	-0.433 0.183	-0.055 0.865		0.078 0.811	-0.113 0.727	-0.479 0.115	-0.234 0.489	0.100 0.758
Max Storm Top (TOP) (100 ft)	-0.238 0.393	-0.082 0.782	0.523 0.045	0.535 0.040	0.281 0.331	0.216 0.440	0.078 0.811		0.253 0.361	-0.311 0.259	0.446 0.110	-0.035 0.902
Max VIL	-0.248 0.373	0.217 0.457	0.318 0.248	0.606 0.017	-0.104 0.723	0.867 0.000	-0.113 0.727	0.254 0.361		-0.121 0.667	0.574 0.032	-0.047 0.868
Δ Time Core Impact/Obs Wind (min)	0.305 0.269	-0.283 0.328	-0.198 0.480	-0.454 0.089	0.372 0.190	-0.270 0.331	-0.479 0.115	-0.311 0.259	-0.121 0.667		-0.182 0.535	0.051 0.856
Δ Time Max Convergence/Observed Wind (min)	0.096 0.744	-0.232 0.424	0.219 0.453	0.553 0.040	0.139 0.636	0.465 0.094	-0.234 0.489	0.446 0.110	0.574 0.032	-0.182 0.535		-0.229 0.431
Microburst Speed (m s <sup>-1</sup> )	-0.140 0.619	0.498 0.070	0.104 0.713	0.135 0.633	-0.093 0.752	0.205 0.463	0.100 0.758	-0.035 0.902	-0.047 0.868	0.051 0.856	-0.229 0.431	

4.4.1 Radar Variables with a Normal Distribution. As with the thermodynamic variables, the first step in determining the distribution of the  $n = 15$  samples of aspect ratio was to perform a Wilk-Shapiro/Rankit plot to check for normality. Statistix<sup>®</sup> yielded a Wilk-Shapiro value of 0.9135 for the aspect ratios, indicating a normal distribution provided a good fit. Figures 13 and 14 below show the Wilk-Shapiro/Rankit plot and normal probability distribution function of the aspect ratios with a  $\mu = 0.6$  and  $\sigma = 0.2$ .

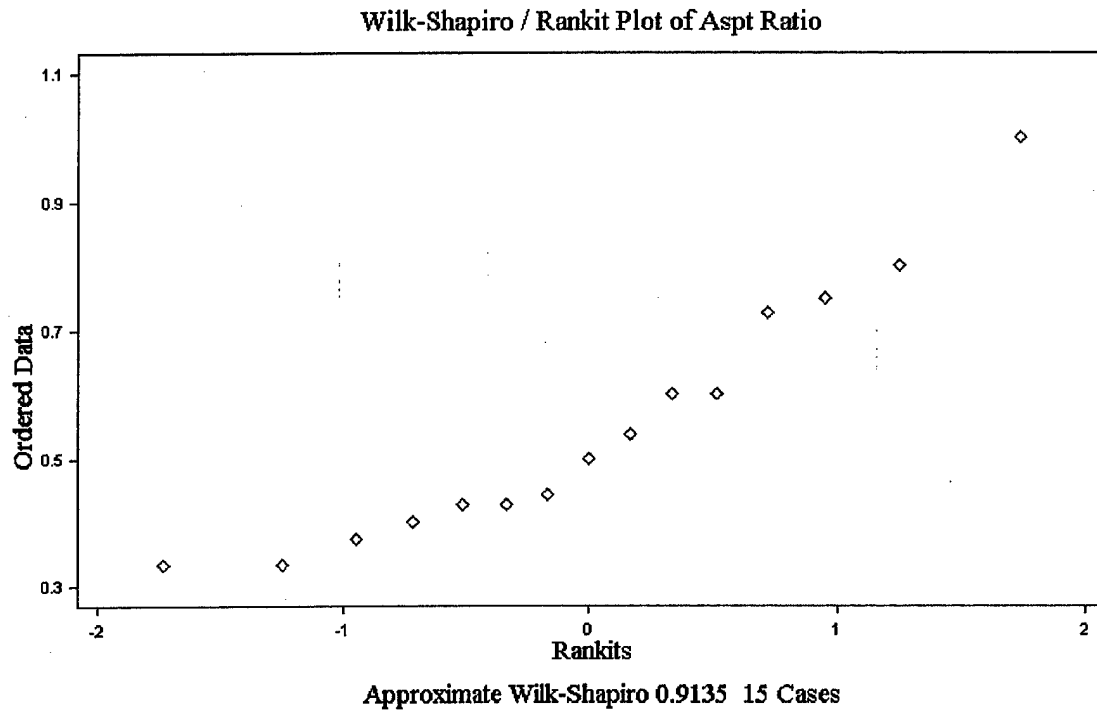


**Figure 13. Wilk-Shapiro Plot of the Aspect Ratios.**

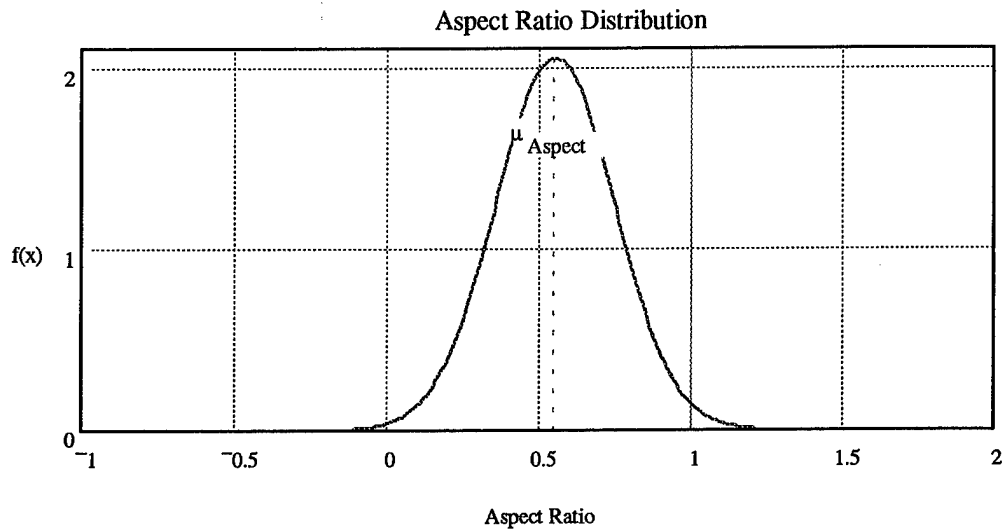


**Figure 14. Normal Distribution of the Aspect Ratios.**

The distributions of the descent rate ( $\text{m min}^{-1}$ ), maximum height of the central core (m), maximum dBZ,  $\Delta$  time core impact and microburst observed (min),  $\Delta$  time maximum mid level convergence and microburst observed (min), maximum storm tops (100's feet), and maximum vertically integrated liquid ( $\text{kg m}^{-2}$ ) were similarly determined to be normally distributed with their respective means and standard deviations as listed in Table 6.

**4.4.2 Radar Variables with a Lognormal Distribution.** To determine the distribution of the  $n = 14$  samples of maximum convergence ( $\text{s}^{-1}$ ), Statistix<sup>®</sup> performed a Wilk-Shapiro/Rankit plot to check for normality. The resulting Wilk-Shapiro value was 0.8868, indicating a less than ideal normal distribution fit. A logarithmic transformation was computed and this transformed data set was subjected to a Wilk-Shapiro/Rankit plot. The Wilk-Shapiro value of the transformed sample was 0.9272, denoting lognormal distribution. The probability density function for the convergence was therefore estimated as lognormal with a  $\mu = -5.7$  and  $\sigma = 0.5$ . Figures 15 and 16 are the Wilk-Shapiro/Rankit plot and lognormal distribution for the maximum mid-level convergence.

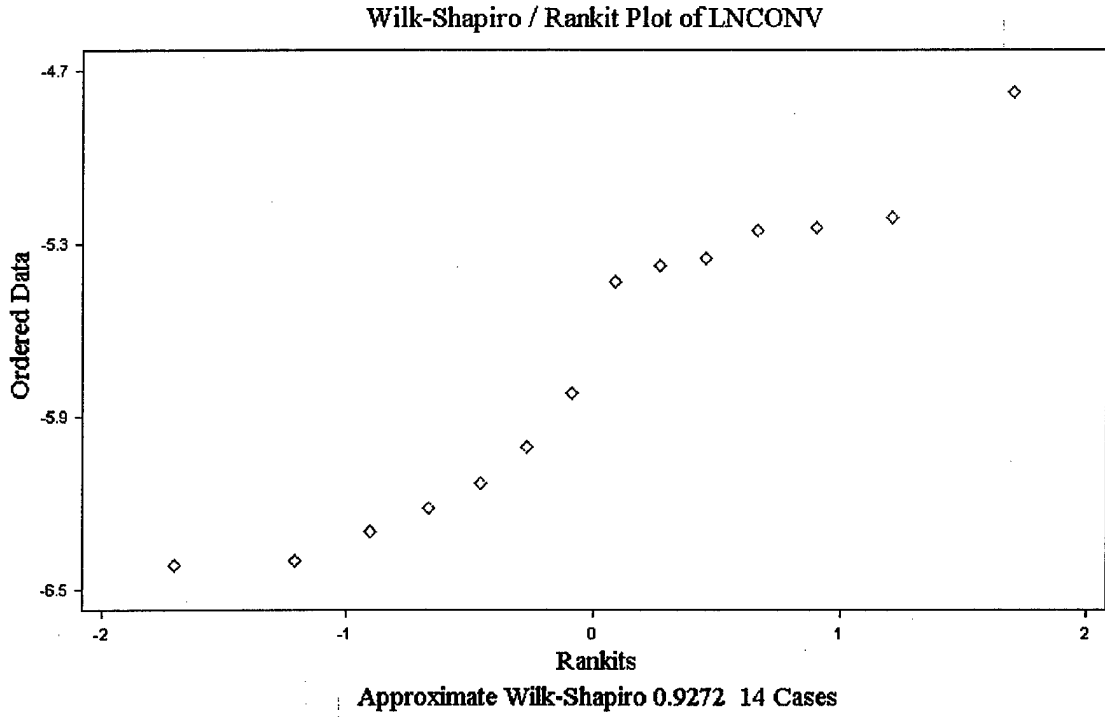


**Figure 15. Wilk-Shapiro Plot of the LN(Maximum Mid Level Convergence).**

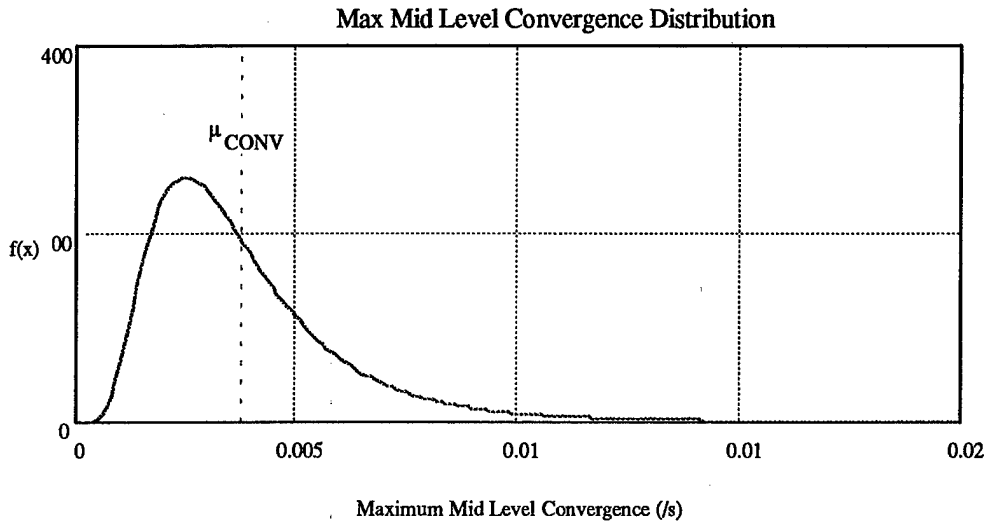


**Figure 16. Lognormal Distribution of Maximum Mid Level Convergence.**

The distributions of the storm top divergence ( $s^{-1}$ ) and the height of maximum convergence (m) were similarly determined to be lognormal.

#### 4.5 Radar Regression Equations

Returning to the physical forces influencing the development and evolution of a microburst, two regression equations using radar variables to model microburst outflow velocity were developed. The transfer of momentum and mass are discernible on the NEXRAD. Six of the radar variables studied which incorporate momentum and mass transfer, were selected for inclusion into the non-linear regression equations to model microburst outflow speed. All of the variables are easily deduced by an operational forecaster; however, three can not be computed quickly enough for operational employment. The selected variables were the descent rate, maximum height of the central core, height of maximum convergence, maximum dBZ, maximum storm top, and maximum VIL. The descent rate is the downward velocity of the storm core and therefore related to momentum. The maximum height of the central core gives the distance over which the core can descend and is associated with momentum. The height of maximum convergence gives an estimate of where horizontal velocity is transformed into downward velocity. The maximum dBZ and VIL value give an estimate of the quantity of mass aloft that will be subjected to downward transport. The greater storm top values have been associated with stronger mid-level convergence, and have been correlated to stronger outflows (Stewart, 1996:324). The descent rate, height of maximum convergence, and maximum height of the central core are too time consuming to determine given the lifespan of a microburst and are therefore not included in the second regression equation. The two regression equations are:

$$V_{\text{maxrad}} = \exp(a \cdot \text{Desrate} + b \cdot \text{hgtcencore} + c \cdot \text{hgtmaxconv} + d \cdot \text{dBZ} + e \cdot \text{TOP} + f \cdot \text{VIL} + g) \quad (38)$$

$$V_{\text{maxrad}} = \exp(\alpha \cdot \text{dBZ} + \beta \cdot \text{TOP} + \chi \cdot \text{VIL} + \delta) \quad (39)$$

where

$V_{\text{maxrad}}$  is the predicted maximum microburst outflow velocity ( $\text{m s}^{-1}$ ),

$a = 0.001$ ,

$b = -1.720\text{E-}05$ ,

$c = 1.350\text{E-}05$ ,

$d = 0.067$ ,

$e = -0.001$ ,

$f = -0.021$ ,

$g = -0.177$ ,

$\alpha = 0.047$ ,

$\beta = 2.503\text{E-}05$ ,

$\chi = -0.016$ ,

$\delta = 0.761$ ,

Desrate is the core descent rate ( $\text{m min}^{-1}$ ),

hgtcencore is the maximum height of the central core (m),

hgtmaxconv is the height of the maximum mid level convergence (m),

dBZ is the maximum dBZ value of the microburst producing cell,

TOP is the maximum storm top of the microburst producing cell (100's ft), and

VIL is the maximum vertically integrated liquid of the microburst producing cell ( $\text{kg m}^{-2}$ ).

These regression equations were selected from several produced by Data Fit<sup>®</sup> because each produced the largest respective  $R^2$  value;  $R^2 = 0.374$  for equation (38) and  $R^2 = 0.266$  for equation (39). Tables 11 and 12 present analysis of variance for equations (38) and (39) respectively.



**Table 11. Analysis of Variance for Equation (38)**

	Degrees of Freedom	Sum of Squares	Mean Squares	F-value	P-value
Regression	6	161.594	26.932	0.7957	0.599
Error	8	270.765	33.846		
Total	14	432.359			

**Table 12. Analysis of Variance for Equation (39)**

	Degrees of Freedom	Sum of Squares	Mean Squares	F-value	P-value
Regression	3	189.364	63.121	1.329	0.315
Error	11	522.263	47.478		
Total	14	711.626			

As with equation (37), the next step in evaluating the adequacy of the regression models was to check the model usefulness and validity. A predicted vs. observed velocity plot, a residual plot, and a Wilk-Shapiro/Rankit plot of the residuals were constructed for both models. These plots are depicted below.

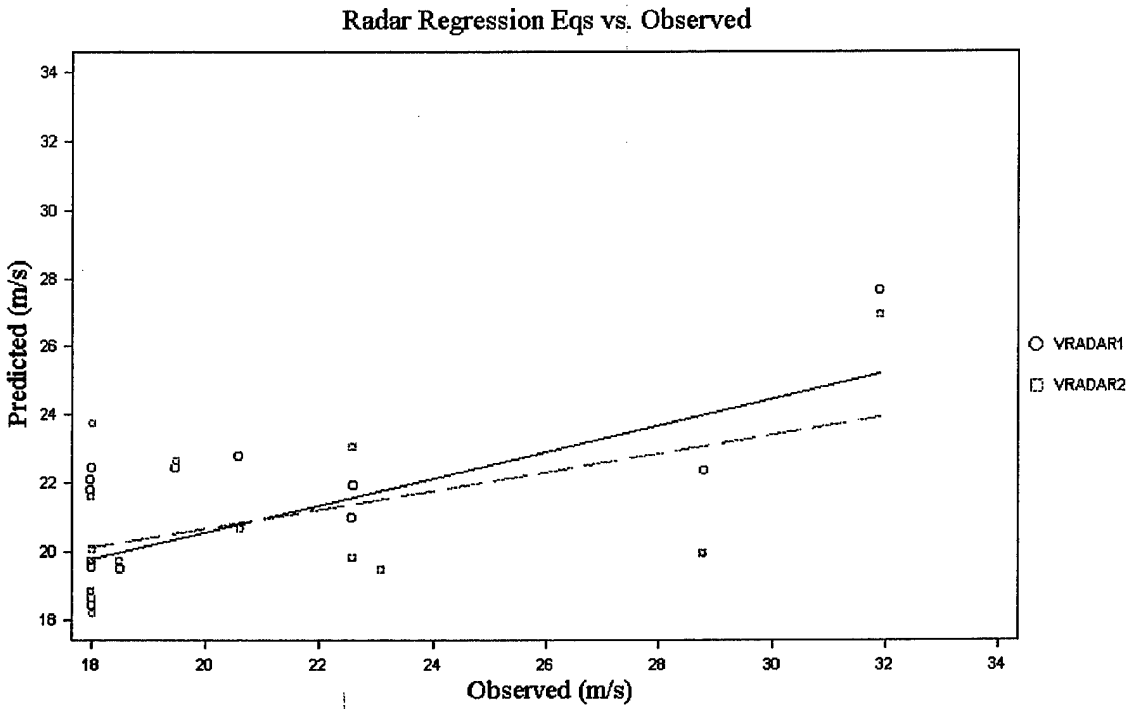


Figure 17. Predicted vs. Observed Plot for Equations (38), solid line, and (39), dashed line.

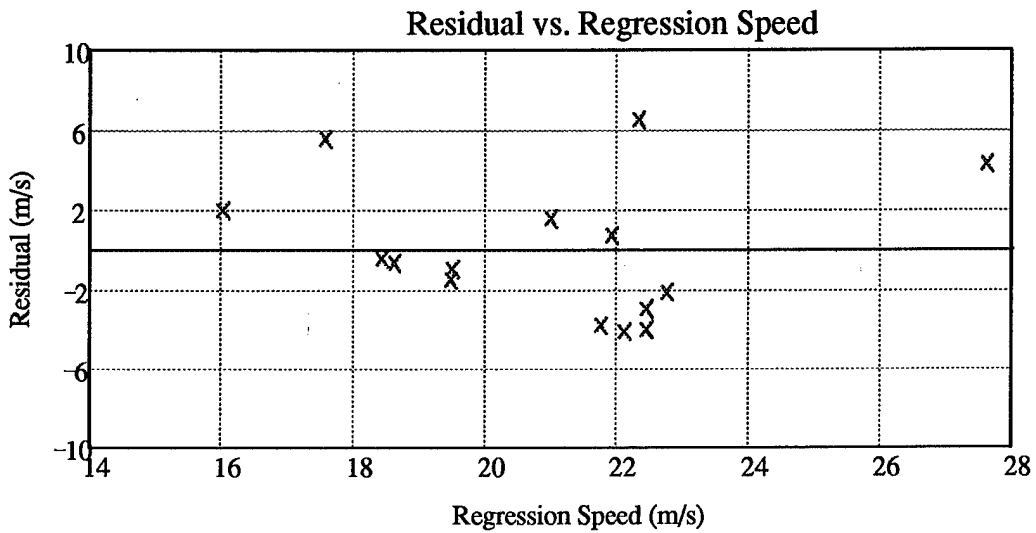


Figure 18. Residual Plot for Equation (38).

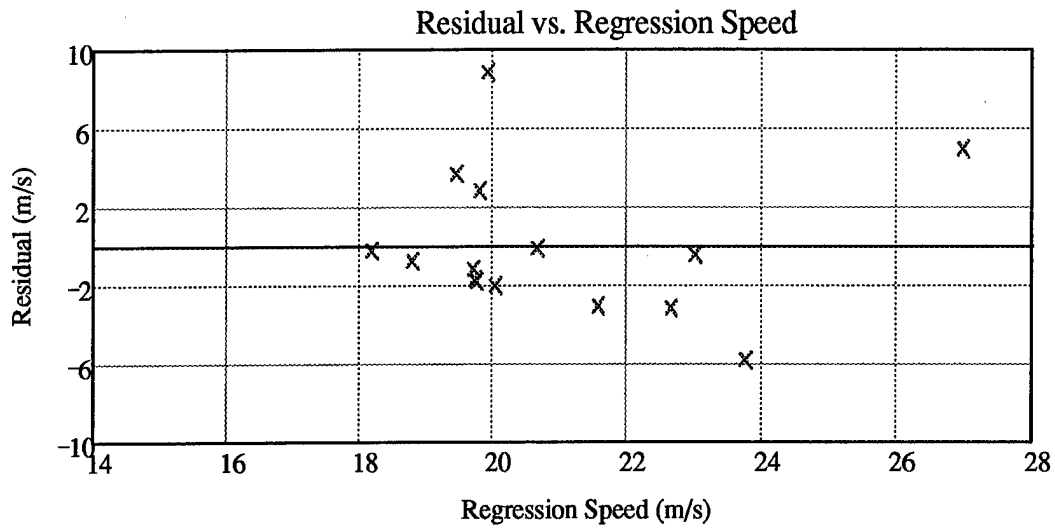


Figure 19. Residual Plot for Equation (39).

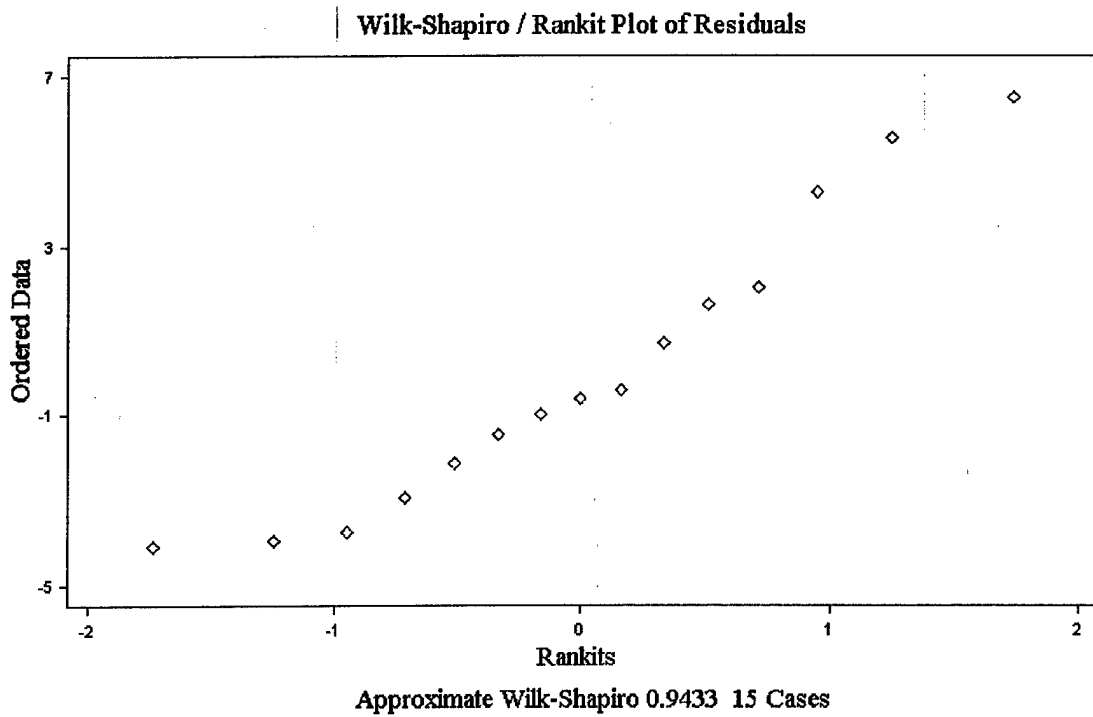
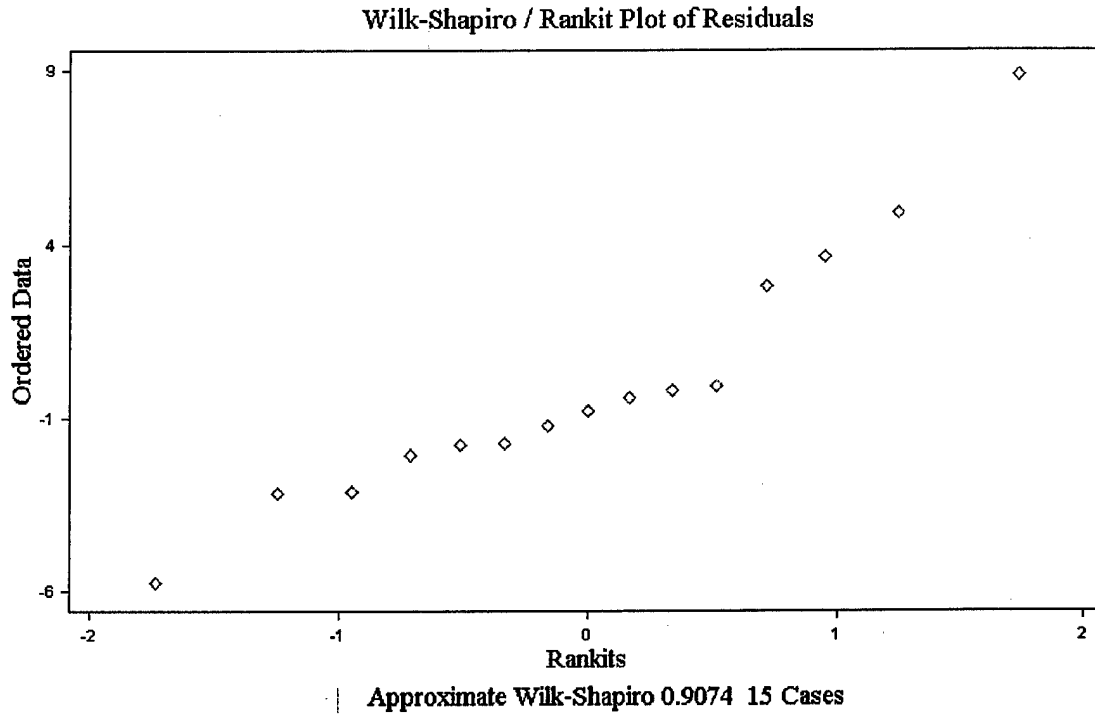


Figure 20. Wilk-Shapiro/Rankit Plot of the Residuals for Equation (38).



**Figure 21. Wilk-Shapiro/Rankit Plot of the Residuals for Equation (39).**

The slopes of the regression lines are  $22.2^\circ$  and  $15.9^\circ$  for equations (38) and (39) respectively, indicating equation (38) provides a good fit to the observed data while equation (39) provides a fair fit to the observed data. The residual plots shown in figures 18 and 19 do not readily demonstrate a fanning out of the residuals, indicating the variance possesses homoscedasticity and favors model aptness. Figures 20 and 21 indicate a Wilk-Shapiro value of 0.9435 and 0.9074 for the residuals of equations (38) and (39), indicating normal distributions of the residuals, which favors model aptness. These factors indicate equations (38) and (39) are both fairly apt models: however, the computed P-values for equations (38) and (39) are 0.599 and 0.315. Based on these P-values, clearly neither equation possesses statistical significance and can not reliably be applied.

#### 4.6 Distribution of Microburst Velocity

Atmospheric variables are often bounded by a physical limit and strongly skewed to the right (Wilks, 1995:86). Due to the skewness of these distributions a normal distribution does not provide a good fit to the data, such as windspeed; however, a gamma distribution does provide a very good fit. Using this premise, the microburst outflow velocities were fit to a gamma distribution with the parameters  $\alpha$  and  $\beta$  estimated using the technique suggested by Thom (Wilks, 1995: 89).  $\alpha$  is estimated as

$$\alpha_{\text{est}} = \frac{1 + \left(1 + \frac{4D}{3}\right)^{\frac{1}{2}}}{4D} \quad (40)$$

where

$$D = \ln(x_{\text{mean}}) - \frac{1}{n} \sum_{i=1}^n \ln(x_i) \quad (41)$$

and

$x_{\text{mean}}$  is the mean of the sample, and

$x_i$  is the  $i^{\text{th}}$  element.

$\beta$  is estimated as

$$\beta_{\text{est}} = \frac{x_{\text{mean}}}{\alpha_{\text{est}}} \quad (42)$$

Using the Thom estimators the following values for  $\alpha_{\text{est}}$ ,  $\beta_{\text{est}}$ , and D were computed,

$\alpha_{\text{est}} = 37.078$ ,  $\beta_{\text{est}} = 0.551$ , and  $D = 0.014$ . Figure 22 below illustrates the approximate gamma distribution for the microburst outflow velocities.

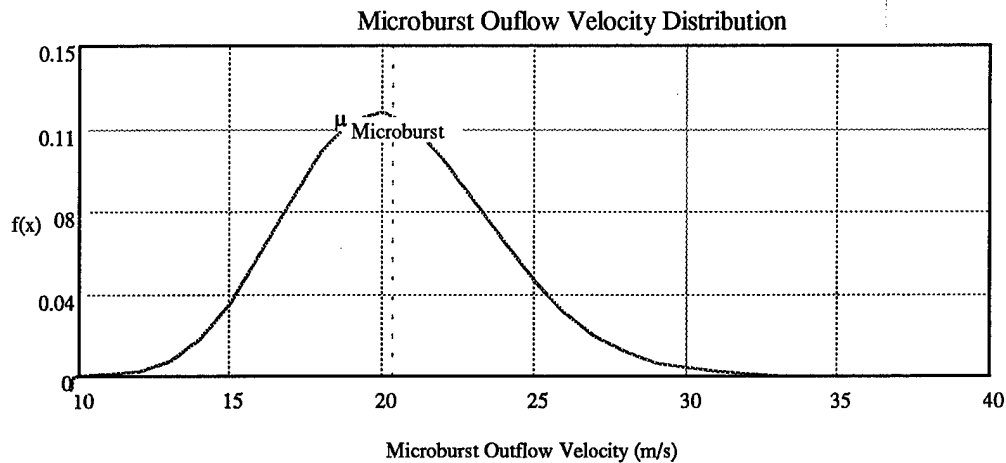


**Figure 22. Gamma Distribution for Microburst Outflow Velocities.**

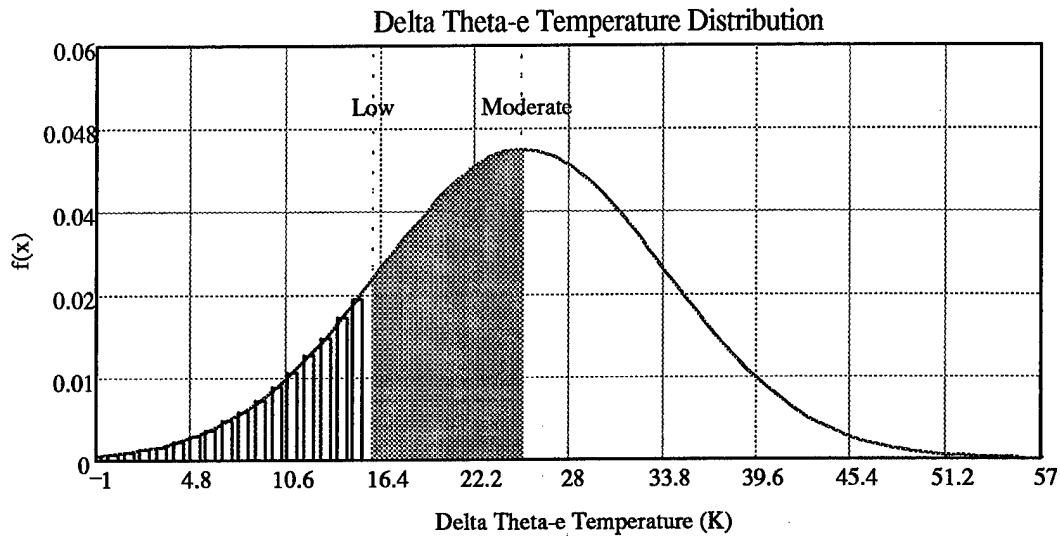
#### 4.7 Development of Microburst Forecasting Technique

The development of the proposed microburst forecasting technique proceeded in three steps. First, identify the threat potential of a microburst occurring. Second, predict the intensity of any microbursts that develop. Third, identify the key radar signatures from the NEXRAD that serve as reliable precursors of imminent microbursts.

4.7.1 Identifying the Microburst Threat. The primary means of identifying the potential for microburst formation is by evaluating the most representative vertical sounding for the region of interest. Following the precedence established by Wakimoto and others, the most important thermodynamic variable for predicting the occurrence or non-occurrence of microbursts is  $\Delta\theta_e$  (see Section 2.4 for definition of  $\Delta\theta_e$ ). Wakimoto determined the threat of microbursts using the following criteria:  $\Delta\theta_e \leq 13$  K implies microbursts are unlikely,  $13 \text{ K} < \Delta\theta_e < 20$  K implies microbursts are possible, and  $\Delta\theta_e \geq 20$  K implies microbursts are likely.

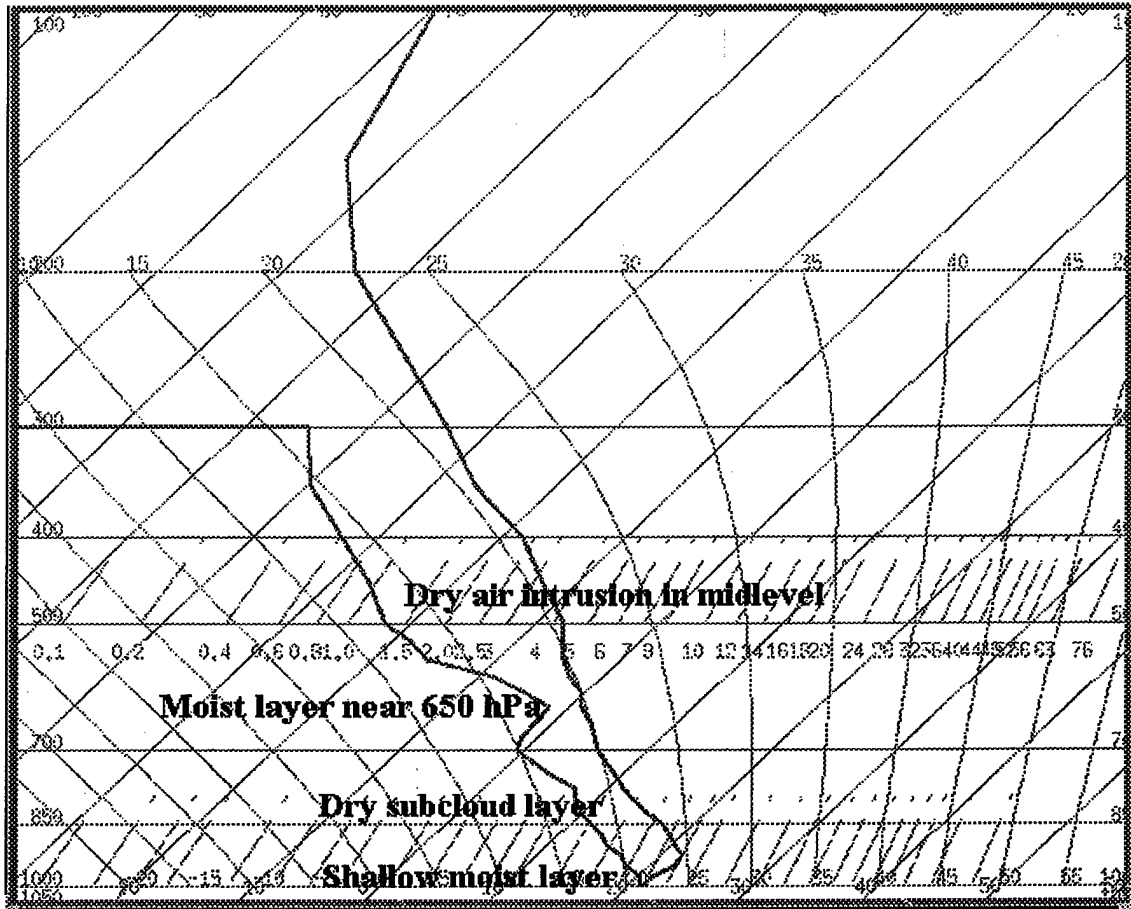
Using the sample of 39 vertical soundings associated with microburst events and the determined normal distribution of  $\Delta\theta_e$ , the threat of microbursts occurring were broken into three categories: low threat if  $\Delta\theta_e \leq 15$  K; moderate threat if  $\Delta\theta_e < 25$  K; high threat if  $\Delta\theta_e \geq 25$  K.

Figure 23 depicts the normal distribution of  $\Delta\theta_e$  with the critical values for each of the three threat categories annotated.



**Figure 23. Distribution of  $\Delta\theta_e$  with the Critical Temperatures Annotated.**

One of the most readily available and informative tools available to the operational forecaster is the thermodynamic diagram. Two types of thermodynamic diagrams were investigated. The skew-T, log-p diagram has been a favorite tool among forecasters and researchers for many years. The skew-T data are available twice a day from each location where upper air soundings are performed. Highlighting the specific features on skew-T's that have been associated with environments conducive to microbursts will allow forecasters to focus on the days when microburst potential is greater. To determine these features a mean vertical sounding was computed. Using this mean sounding a skew-T, log-p diagram was constructed and is presented as figure 24. There are four key features to note on the skew-T: the shallow nearly saturated layer in the boundary layer, the subcloud dry layer present below 850 hPa, capped by a moist layer near 650 hPa, and the dry pocket in the mid levels. This dry pocket is the source of the rapid evaporation and melting, a major mechanism in the formation of wet microbursts.



**Figure 24. Mean Skew-T, Log-p Diagram for Environment Conducive to Microbursts.**

While the skew-T, log-p can provide a wealth of information, it fails to capitalize on the importance of  $\Delta\theta_e$  to the formation of microbursts. For this reason researchers studying microbursts have developed and used a  $\theta_e$  diagram, here after referred to as  $\theta_e$  plot. This diagram features  $\theta_e$  as the abscissa and pressure as the ordinate. The  $\theta_e$  plot highlights the presence of a mid level dry pocket, the most important thermodynamic variable to microburst formation. Using a  $\theta_e$  plot a forecaster can quickly gauge the vertical depth and magnitude of  $\Delta\theta_e$ . Computing a  $\theta_e$  plot for the day in question and comparing it to one associated with microbursts will aid a forecaster in determining the likelihood of microbursts for the day in question. To meet this goal a mean  $\theta_e$  plot was computed using the 39 soundings and is depicted in figure 25.



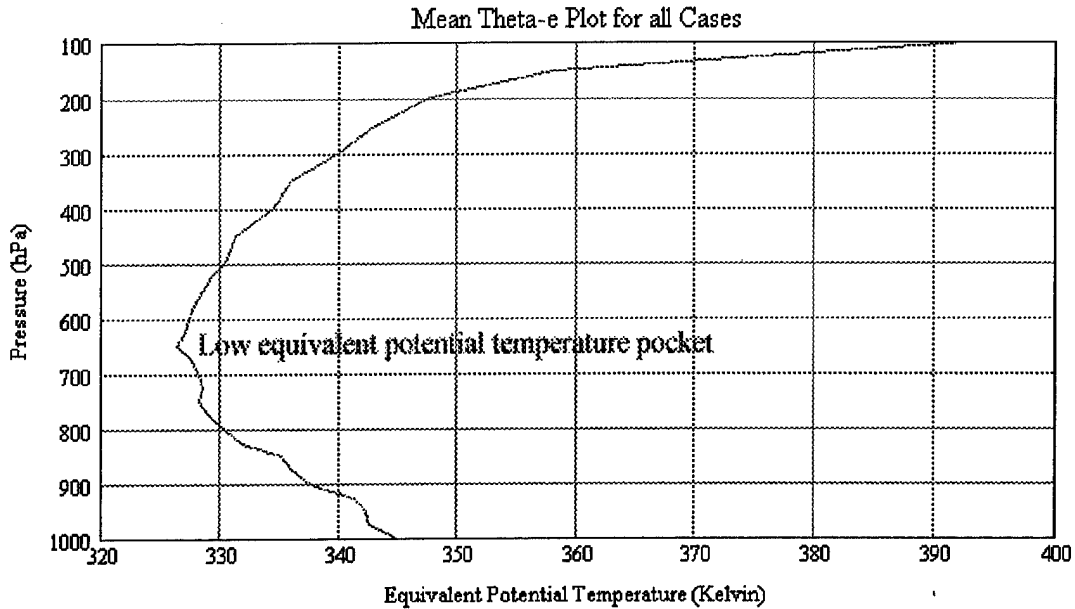


**Figure 25. Mean  $\theta_e$  Plot for all 39 Upper Air Soundings.**

**4.7.2 Predicting the Microburst Intensity.** The second phase in developing a microburst forecasting technique is to determine a means of predicting the intensity of the outflow. Six predictive equations were selected for comparison. Four of the equations came from the literature review; these equations were VIL/TOP, WINDEX, Wolfson's, and Rose's. The other two were the thermodynamic and radar regression equations, (37) and (39) respectively. Each of the 6 equations were applied to the applicable microburst events. Once the predicted velocities were computed the root mean square error and mean absolute error were computed for each equation. A second means of comparison was to construct forecast vs. observed plots depicted in figures 26 - 28. Table 13 presents a case by case synopsis of the predicted outflow velocity for each equation and the observed wind speed.

**Table 13. Predicted and Observed Microburst Velocities**

ICAO Date	VIL/TOP (m s <sup>-1</sup> )	WINDEX (m s <sup>-1</sup> )	Wolfson's (m s <sup>-1</sup> )	Rose's (m s <sup>-1</sup> )	V <sub>thermo</sub> (m s <sup>-1</sup> )	V <sub>radar</sub> (m s <sup>-1</sup> )	Observed (m s <sup>-1</sup> )
BHM 8/4/95	27.3	14.8	23.3	33.8	20.5	23.0	22.6
BHM 6/16/97	25.3					20.7	20.6
ATL 7/10/94		1.3		31.0	20.3		19.5
BIX 7/17/94		21.4		26.2	19.9		18
BIX 7/22/94		62.1		28.1	19.3		18.5
CBM 6/29/94		47.4		26.5	21.5		19.5
CBM 6/30/94		24.8		27.1	21.0		18.5
CBM 7/25/94		31.7		25.3	31.3		31.9
CSG 6/29/94				34.9	20.3		18.5
GWO 7/15/94		25.6		28.3	20.2		20.6
MEI 7/1/94		42.8		28.6	20.2		29.3
MEI 7/24/94				24.0	19.9		21.1
CHS 6/28/95		59.4		23.7	20.2		18
CSG 6/2/95		39.3		34.5	19.5		21.6
CSG 6/11/95		21.2		25.6	17.6		18.5
MGM 8/15/95		49.7		24.7	22.3		23.6
MXF 8/20/95		64.6		26.8	19.0		18.5
NIP 7/7/95				24.3	19.8		20.6
NIP 8/19/95	10.5	26.7	7.3	22.2	23.0	18.2	18
ATL 8/24/96	31.4		12.6	26.8	19.8	19.8	18
CSG 6/24/96		13.1		26.9	20.1		27.8
HSV 7/8/96		38.6		27.8	19.6		19
MCN 7/8/96	22.3	9.5	18.3	30.4	20.5	21.6	18.5
MCN 7/17/96				28.4	19.3		18
NSE 6/13/96	17.3	37.1	2.7	25.1	21.3	18.8	18
WRB 8/23/96				27.136	19.885		21.1
CHS 6/14/97	18.9	26.1	20.8	27.1	18.1	22.7	19.5
CHS 6/3/97	30.6	23.7	17.3	27.4	18.5	19.7	18
CHS 6/18/97		24.4		28.3	20.0		18.5
CHS 6/27/97	32.6	22.0	23.7	25.6	19.9	19.8	22.6
GWO 6/28/97	21.5	59.6	40.8	20.6	21.4	27.0	31.9
HSV 6/13/97		36.9		25.8	20.0		18.5
MCN 6/18/97				31.2	19.2		18
MCN 6/25/97				26.6	19.		18.5
MEI 6/23/97	23.7	22.0	16.0	26.1	20.8	19.4	23.1
MEI 7/11/97	19.3	9.6	28.8	20.6	21.0	20.0	18
NIP 6/14/97		35.7		32.9	19.5		18.5
NSE 6/13/97	30.4	31.1	25.3	28.9	20.3	19.7	18.5
NZC 6/22/97	23.3		13.6	29.3	20.2	23.7	18
VLD 6/27/97				24.7	21.1		20.6
WRB 8/3/95	20.4					19.9	28.8

The root mean square error and mean absolute error was computed as

$$\text{RMSE} = \left( \frac{1}{n} \sum_{i=1}^n (\text{forecast} - \text{observed})^2 \right)^{1/2} \quad (43)$$

$$\text{MAE} = \frac{1}{n} \sum_{i=1}^n |\text{forecast} - \text{observed}| \quad (44)$$

Using these formulas the RMSE and MAE for each of the six predictive equations was computed, the results of which are summarized in Table 14.

**Table 14. RMSE and MAE Table for the Six Intensity Prediction Equations**

	VIL/TOP	WINDEX	Wolfson's	Rose's	V <sub>thermo</sub>	V <sub>radar</sub>
RMSE (m s <sup>-1</sup> )	7.8	19.2	7.3	8.7	3.1	3.6
MAE (m s <sup>-1</sup> )	6.4	14.6	5.6	7.8	2.2	2.7

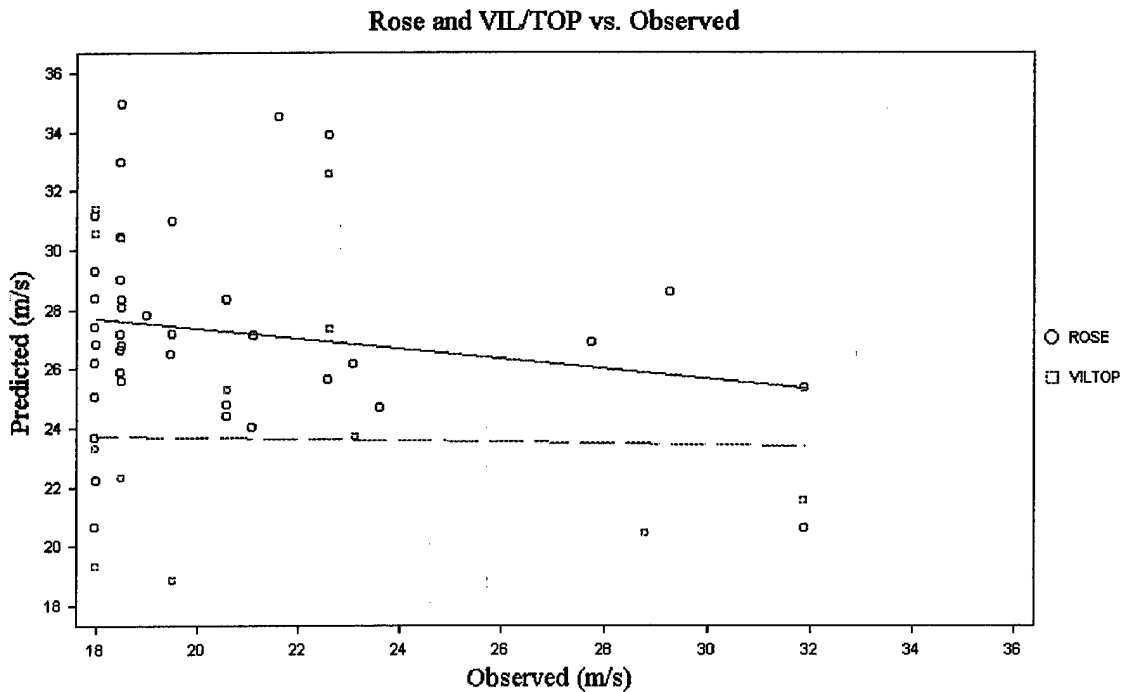


**Figure 26. Scatter Plot of Rose's , solid line, and VIL/TOP, dashed line, Equations vs. Observed Wind Speed.**

Thermo and Radar Regression vs. Observed

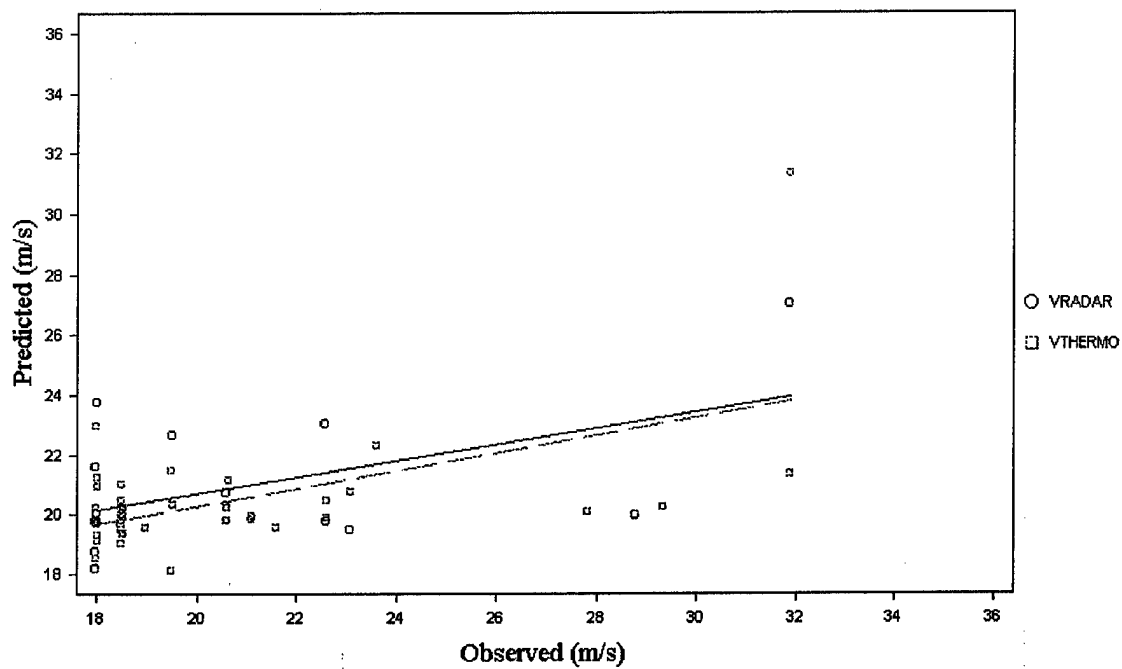
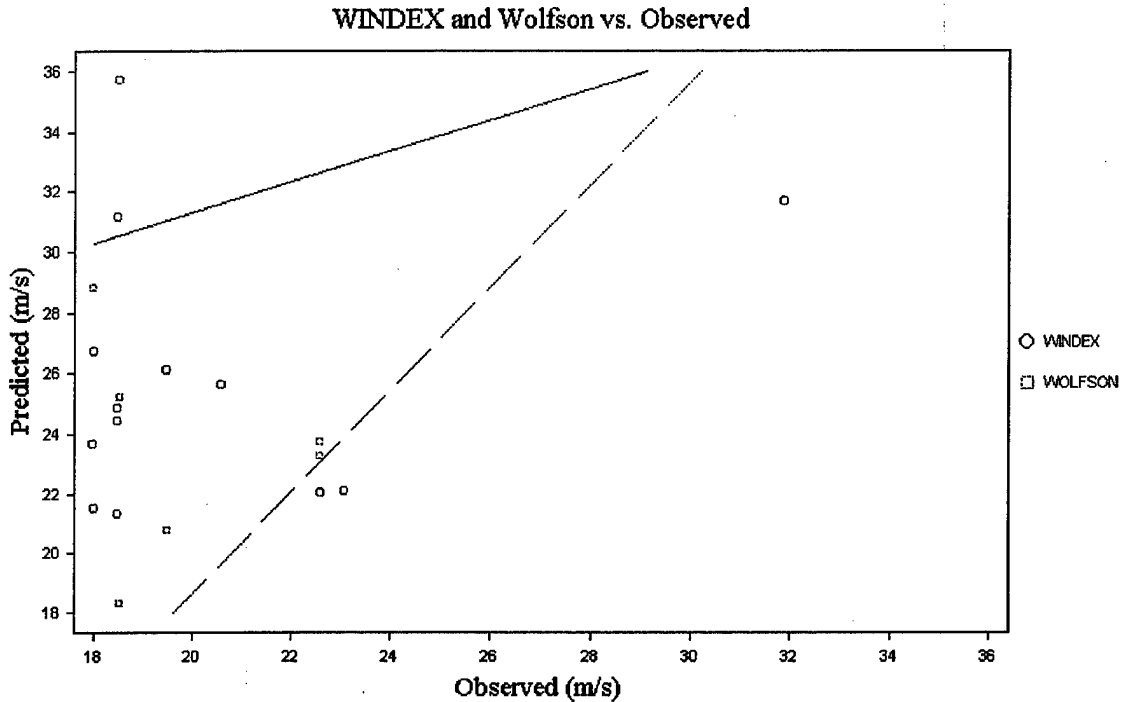


Figure 27. Scatter Plot of Regression Equations vs. Observed Wind Speed,  $V_{\text{radar}}$  is solid line and  $V_{\text{thermo}}$  is dashed line.



**Figure 28. Scatter Plot of WINDEX, solid line, and Wolfson's, dashed line, Equations vs.**

**Observed Wind Speed.**

Based upon the results of the RMSE and MAE calculations and scatter plots two predictive equations were selected for inclusion into the proposed forecasting technique. These equations were Rose's and VIL/TOP equations. Wolfson's equation performed slightly better than VIL/TOP; however, given the lifespan of a typical microburst the VIL/TOP equation was selected based upon expediency.

**4.7.3 Identifying Radar Precursors.** Based upon previous microburst studies and the radar imagery studied during this research 8 precursor radar signatures were selected for inclusion into the forecast technique. These precursor signatures were max dBZ > 50 dBZ, core descending > 100 m min<sup>-1</sup>, maximum mid level convergence between 2 and 4.5 km, mid level convergence > 3.5 E-03 s<sup>-1</sup>, the presence of rotation near the cloud base, storm top divergence > 3.5 E-03 s<sup>-1</sup>, the presence of a reflectivity notch, and the presence of a reflectivity weak echo trench. Table 15

below summarizes the occurrence of these precursors for the 15 cases studied. Figures 29 - 33 present examples of these precursor radar signatures encountered during the data collection.

**Table 15. Occurrence Rate of the 8 Selected Radar Precursor Signatures**

$\geq 50$ dBZ	14/15
Descent Rate $> 100$ m $\text{min}^{-1}$	12/15
Maximum mid level Convergence Between 2 and 4.5 km	8/14
Convergence $> 3.5 \text{ E-}03$ $\text{s}^{-1}$	7/14
Rotation Near Cloud Base	9/10
Storm Top Divergence $> 3.5 \text{ E-}03$ $\text{s}^{-1}$	5/13
Reflectivity Notch	6/15
Weak Echo Trench	6/15

**4.7.3.1 Radar Signature Examples.** Figure 29 depicts a composite, 4-panel cross-section through a microburst producing storm near Meridian, Mississippi on 23 Jun 97. The image was recorded by the Jackson, Mississippi RDA, 147 km away. The vertical axis of each panel is in 1000's feet and the horizontal axis is in nautical miles. The time of each image, in UTC, is listed in the lower right corner of the respective image. The storm's central core, with a reflectivity  $\geq 50$  dBZ, is depicted in white. Surrounding the central core are descending radar reflectivity values depicted in differing shades of gray. The first panel depicts the central core at its maximum vertical extent at 1744 UTC. The second panel depicts the core beginning its descent towards the surface at 1750 UTC. In the third panel, 1756 UTC, it is clearly evident the core has descended several thousand feet during a 6 minute interval; note the signal loss below 14 kft due to beam blockage and attenuation. Most noticeable in the fourth panel is the absence of the central core, as it has descended below the radar beam by 1802 UTC. This cell produced a microburst outflow of  $23.1 \text{ m s}^{-1}$ .

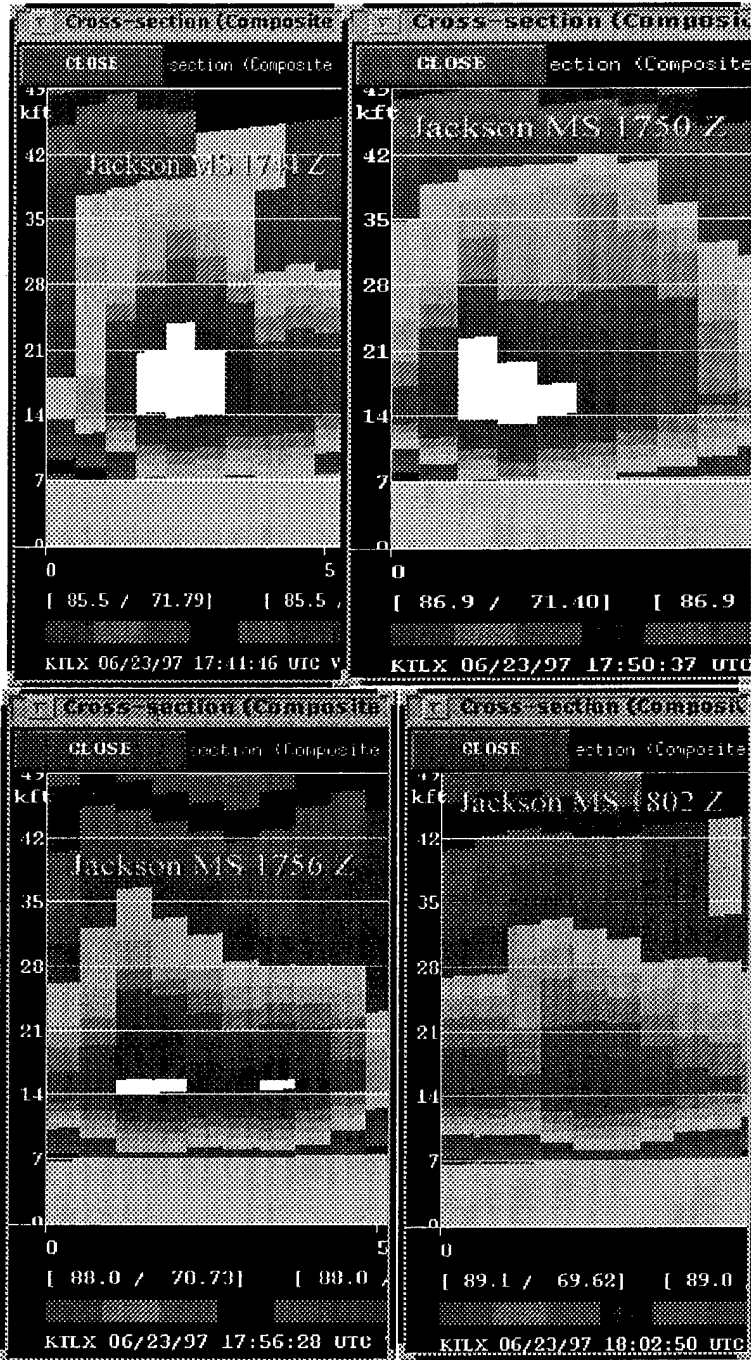


**Figure 29. 4-Panel Display of a Rapidly Descending Reflectivity Core Associated with the 6/23/97 Microburst at Meridian, Mississippi.**

Figure 30 depicts a composite, 3-panel cross-section through a microburst impacting the surface near Robbins AFB, Georgia on 3 Aug 95. The image was recorded by the Robbins AFB RDA, 29.8 km away. The vertical axis of each panel is in 1000's feet and the horizontal axis is in nautical miles. The time of each image, in UTC, is listed in the lower right corner of the respective image. The storm's central core is depicted as a light gray shade located near the 12 nmi point in the first panel. Surrounding the central core are descending radar reflectivity values depicted in differing shades of gray. The first panel depicts the 1945 UTC cross-section, the core has impacted the surface and the outline of the expanding outflow is becoming discernible on the right side of the image. Panel two shows the 1950 UTC image. The core is no longer present; however, the effects of the outflow are seen as uplifting swirls of higher reflectivity values near the 8 nmi and 11 nmi points. The third panel, taken at 1955 UTC, shows possible new convection forming near the 4 nmi point as a consequence of the rapid outflow from the microburst. The reader is referred to Figures 1 and 5 for schematic representations of a microburst.



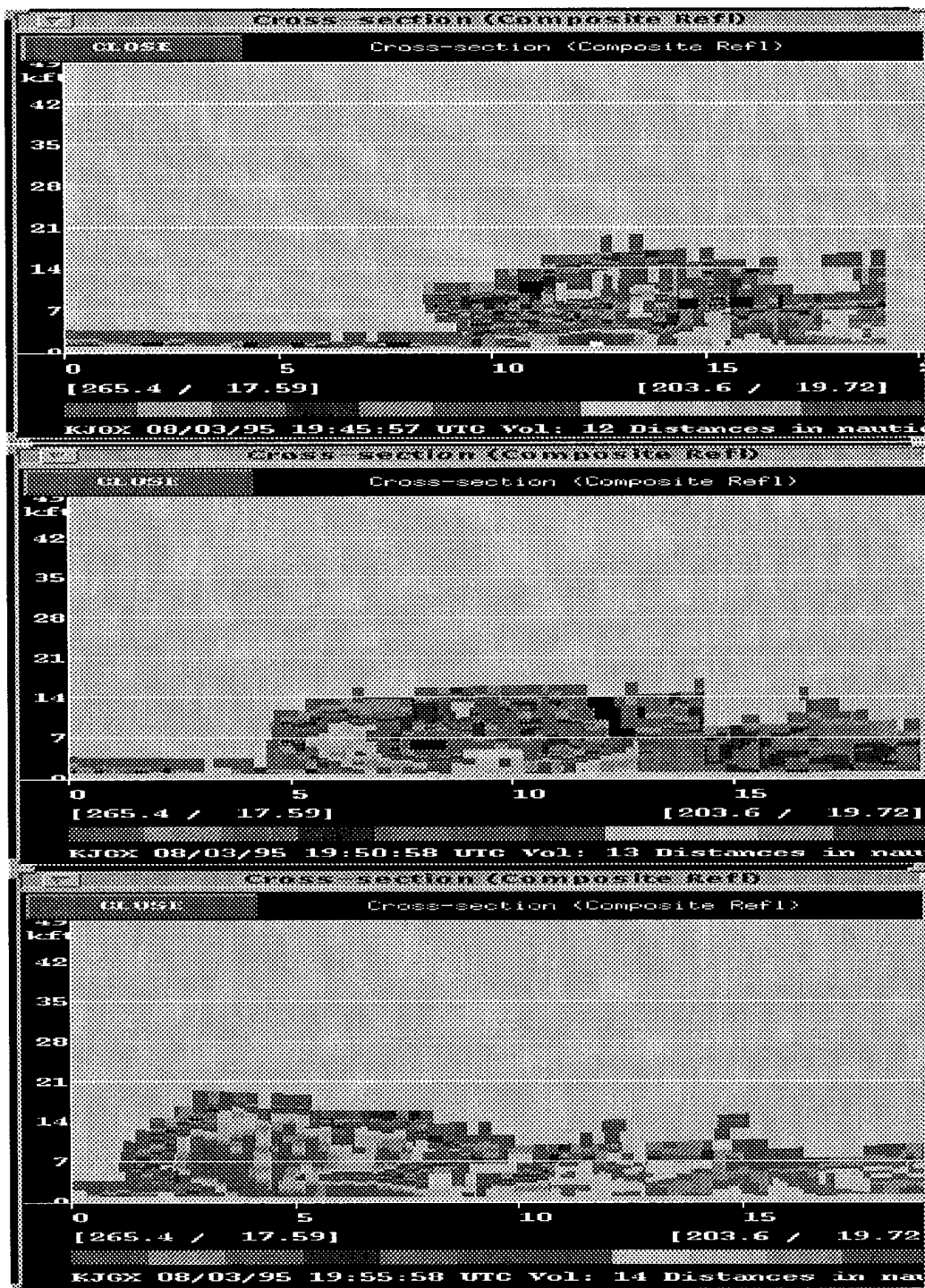
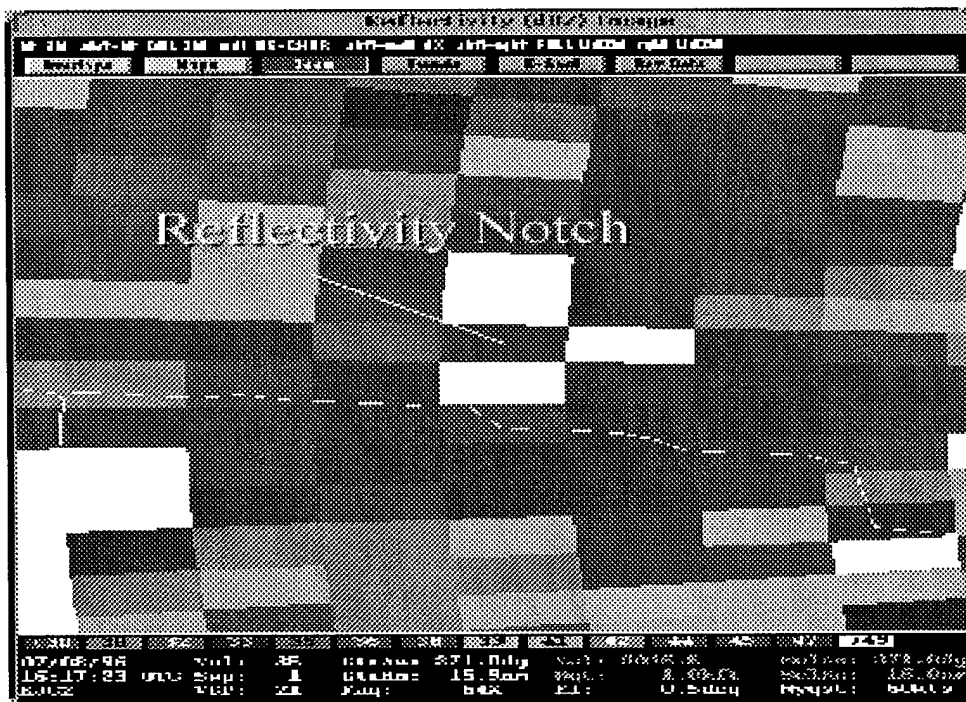


Figure 30. 3-Panel Display Depicting a Microburst Impacting the Surface Near Robbins AFB

GA on 8/3/95 with Observed Outflow Velocity of  $28.8 \text{ m s}^{-1}$ .

Figure 31 depicts a  $0.5^\circ$  horizontal slice of a microburst producing storm near Macon, Georgia. The image was taken at 1616 UTC on 8 Jul 96 from the Robbins AFB RDA located 31.9 km away. The storm core,  $\geq 49$  dBZ, is depicted in white. Within the core is a lower reflectivity notch penetrating from the left side of the image. This reflectivity notch indicates low  $\theta_e$  air being entrained into the storm core, and thus serves as a possible precursor to a microburst. Lower reflectivity levels are depicted as differing shades of gray.



**Figure 31. Reflectivity Notch in Storm Producing Microburst of  $18.5 \text{ m s}^{-1}$  Near Macon GA.**

Figure 32 depicts a strongly divergent velocity field associated with a near surface microburst near Jacksonville, Florida at 2158 UTC on 22 Jun 97. The figure is from the  $0.5^\circ$  elevation scan and depicts the radial velocity field near 600 feet (180 m) AGL. The lighter gray shade surrounded by darker gray shades directly above the cell identifier, boxed number 65, indicates inbound radial velocities of 16 kts ( $8.25 \text{ m s}^{-1}$ ). The lighter gray shade area to the lower

left of the cell identifier indicates outbound radial velocities of 18 kts ( $9.2 \text{ m s}^{-1}$ ). When viewed from a color NEXRAD screen the inbound velocities appear as shades of green and the outbound velocities appear as shades of red.

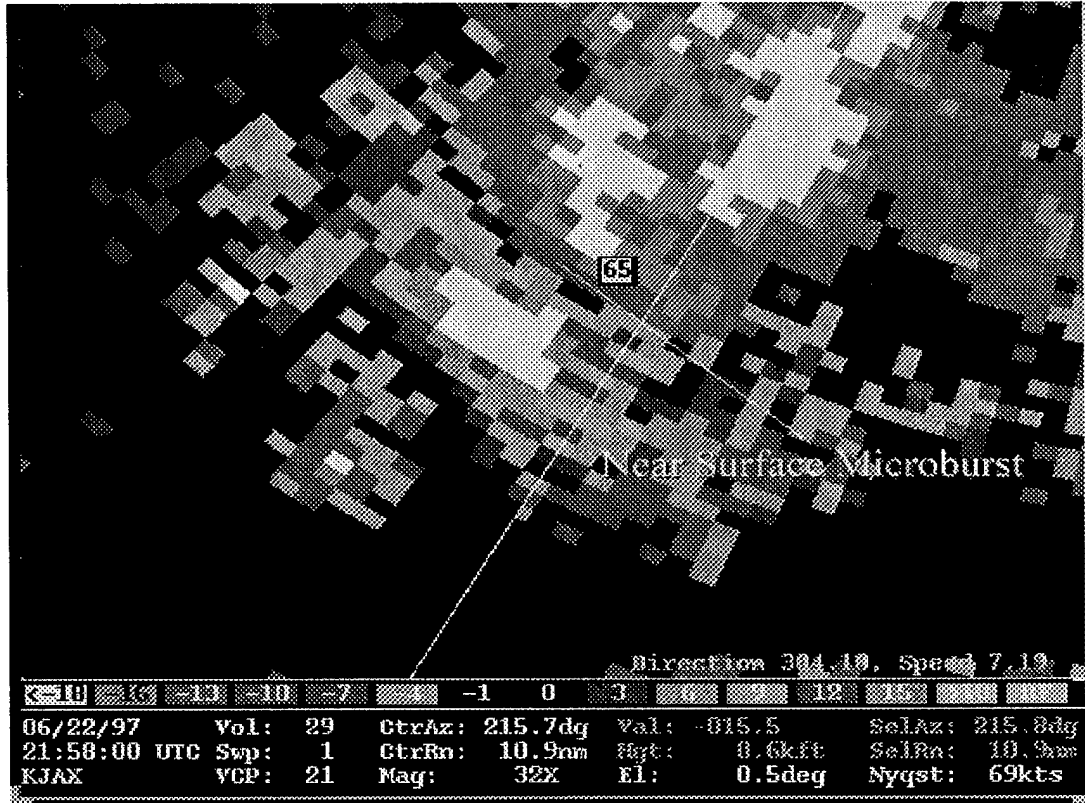


**Figure 32. Divergent Radar Signature Associated with Observed Microburst near Jacksonville FL Producing an Outflow of  $18 \text{ m s}^{-1}$ .**

Figure 33 depicts a weak echo reflectivity trench associated with a microburst producing storm near Atlanta, Georgia on 24 Aug 96. As with previous cross-sections the vertical axis is in 1000's of feet and the horizontal axis is in nautical miles. The dark gray shaded area represents the central part of the storm with a very distinct reflectivity trench centered near 19 kft (5790 m). This reflectivity trench appeared as the central core was descending and the microburst was forming. The reflectivity trench was caused by the influx of lower  $\theta_e$  air into a region of higher

moisture content, leading to rapid evaporation and lower reflectivity, manifesting as the weak echo trench.

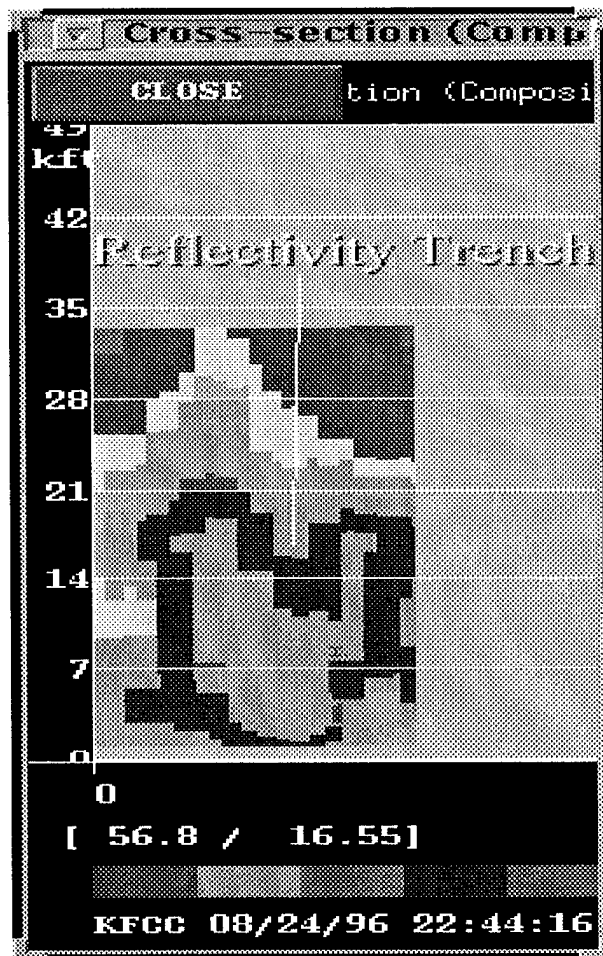


**Figure 33. Weak Echo Trench Associated with Storm Producing an  $18 \text{ m s}^{-1}$  Microburst Near Atlanta GA on 8/24/96.**

4.7.3.2 Radar Precursor Leadtimes. Following the analysis of the 15 radar cases the leadtimes for the first occurring, second occurring, and third occurring precursor signatures were computed using the radar worksheet (see Appendix E). The leadtime was defined as the time difference (minutes) between the identification of the precursor and observed maximum outflow from the microburst. The leadtimes for each precursor were subjected to a Wilk-Shapiro/Rankit

plot and each was determined to be normally distributed. The descriptive statistics for the leadtimes are presented in Table 16 below.

**Table 16. Descriptive Statistics for Precursor Leadtimes**

Statistic (minutes)	1 <sup>st</sup> Precursor	2 <sup>nd</sup> Precursor	3 <sup>rd</sup> Precursor
Mean	24.9	18.4	11.1
Median	24.0	18.0	12.0
Standard Deviation	8.3	7.1	8.3
Minimum	10.0	9.0	1.0
Maximum	41.0	30.0	25.0

While the occurrence of any single precursor is not unique to microburst producing storms, the combination of these precursors increase the probability of a microburst event. Accounting for this fact, the occurrence of the first precursor is not sufficient to provide an operational warning without a high false alarm rate.

4.7.4 Summary of Microburst Forecasting Technique. The proposed forecasting technique includes three phases. First, identify the threat. Second, predict the intensity of the outflow. Third, search for known radar precursor signatures. The combination of these three phases will allow operational forecasters to forewarn aviation personnel of microbursts allowing correct safety measures to be implemented.

Identifying the threat entails classifying the threat for the day in question. Use the latest upper air sounding for the observation site most representative for the area of operations to compute  $\Delta\theta_e$ . Based upon the computed value determine the microburst potential threat as low, moderate, or high using the criteria outlined in Section 4.7.1. Once the microburst potential for the

day has been determined, flight personnel could be briefed of the threat during routine flight weather briefings.

The next step is to predict the intensity of microbursts occurring during the day. An early estimated maximum outflow velocity should be determined using Rose's equation and equation (37), the thermodynamic regression equation. These two predictive equations will give the forecaster a baseline velocity estimate for microburst activity during the day. As convective activity builds through the day these velocity estimates should be refined using VIL/TOP and equation (39), radar regression equations.

The last step is to identify the occurrence of microburst precursor signatures. Since the development of a single precursor is not sufficient for a microburst, and to reduce the chance of a false alarm, warnings for microbursts should not be issued until the second precursor signature is identified. These steps are outlined in the diagram below.

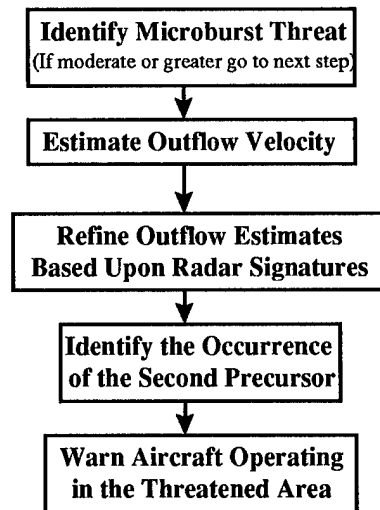


**Figure 34. Schematic Steps of Proposed Microburst Forecasting Technique.**

## V. Conclusions and Recommendations

### 5.1 Overview

Chapter 5 reviews the previous chapters and presents the author's recommendations for future research. Contained in the review are the problem statement and description of the phenomenon studied, a review of the methodology employed, and the technique proposed to improve wet microburst forecasting. A brief discussion of possible error sources is also presented. The last segment of this chapter discusses future research into wet microburst forecasting.

### 5.2 Microburst and Problem Statement Review

Microbursts are intense downbursts from thunderstorms that affect an area  $< 4$  km and have a lifespan  $< 10$  minutes. Wet microbursts are associated with generally heavy precipitation and are found in the eastern and southeastern part of the country. Microbursts are capable of producing winds of  $75 \text{ m s}^{-1}$  and inducing considerable damage at the surface. The greatest threat from microbursts is to low flying aircraft, where the rapid fluctuations in horizontal and vertical airflow create tremendous shear zones. Microbursts have been determined to be the causal factor behind at least three major aircraft accidents resulting in hundreds of fatalities. Due to the short lifespan of microbursts they often seem to strike without warning and pose a serious challenge to operational forecasters trying to provide resource protection to aviation and ground assets. Is there a way to reduce the threat wet microbursts pose to Air Force personnel and assets operating in the southeastern United States? Using upper air soundings, predictive equations, and NEXRAD products wet microbursts can be nowcasted 10 to 20 minutes before maximum velocities are experienced.

### 5.3 Review of Methodology

The methodology employed during this research entailed four phases. First, identify possible microburst events for the timeframe and geographic region specified. This was done by modifying a set of six simultaneous screening criteria applied to surface observations for the area of interest. Further screening was accomplished by removing all highlighted events that were associated with a significant synoptic feature such as fronts, tropical storms, or low pressure systems. The last screening employed ensured all remaining incidents occurred within a specified distance from NEXRAD RDA's to maximize the features to be studied. The second phase was to collect upper air and radar data for the cases remaining following the screening process. Archive level II and upper air soundings for the locations and times closest to the location where the microburst occurred were requested from the Air Force Combat Climatology Center. Once the requested data was received it was subjected to the third phase, data collection. Using the WATADS software and other software the radar and upper air data was analyzed for 28 variables. The analysis was recorded onto worksheets for further study and statistical analysis. The last phase was to perform a statistical analysis on the collected data. The statistical analysis included determining the descriptive statistics, distribution, and correlations of each variable. Once the statistical analysis of the variables was completed an objective analysis of proposed techniques was completed resulting in a proposed step-by-step technique to forecast wet microbursts in the southeastern United States.

### 5.4 Forecasting Technique

The proposed forecasting technique includes three steps. First, identify the threat of microbursts occurring. Second, estimate the maximum outflow velocity to be expected for the day in question. Third, maintain an active watch on the NEXRAD PUP display for the highlighted precursor radar signatures.



Identifying the threat of microbursts for a given period is best accomplished by examining the most representative upper air sounding. Using the upper air sounding a skew-T, log-P diagram and  $\theta_e$  plot are to be constructed and the  $\Delta\theta_e$  value to be computed. From these diagrams, the potential for microbursts can be deduced and further actions taken if warranted.

Predicting the outflow velocity is best accomplished by using two predictive equations. Rose's equation provided a good initial estimate of the outflow velocity to be expected based strictly on thermodynamic variables derived from the upper air sounding; however, equation (37) should not be used operationally until it has been tested and verified on a separate sample. The VIL/TOP equation provided a refined estimate for the maximum outflow velocity based on radar returns.

The final stage is to watch the NEXRAD for the precursor radar signatures highlighted in chapter 4. The occurrence of the second precursor provides a clear estimate of where the microburst is likely to occur, and based on this information the necessary personnel should be quickly notified of the threat.

### 5.5 Possible Sources of Variance

There are three main sources that may have contributed to variance in the data collection and data analysis. The three error sources were spatial density of surface observing locations, sample size, and radar volume scan rate. The density of observation sites and radar scan rate may have affected data collection; the sample size, especially for radar analysis, may have been an error source during data analysis.

As outlined in table 3, the average spacing between observation locations for this research was on order of 100 km. This density of observing sites is adequate for observing synoptic, or masoscale, features but is generally too coarse for observing mesoscale and misoscale events unless they occur within close proximity of the observing site. During previous field projects established to study microbursts the density of observing locations was on order of 2 km. This

density provided much better resolution of smaller scale features. It is the author's opinion that a much greater number of microbursts occurred during the period of study than the 41 explored in this research and were simply missed due to the coarse resolution of the observation network.

In convective precipitation mode the WSR-88D completes one volume scan every 5 minutes. While the radar is interrogating the upper portion of a storm the microburst may be well along in its development below the radar beam, or may have been captured by the radar beam, but has not yet been relayed to the operator. The lifespan of a microburst is approximately 10 minutes and a volume scan every 5 minutes does not provide the most ideal temporal scale for evaluating such a short lived event. Between volume scans features may have developed and dissipated without knowledge of the operator and thus may be considered a source of error.

The third possible error source is the sample size. The radar sample size was only 15 events, and while this is comparable to other studies it is far from ideal and is thus a possible error source. A sample of 30 or more events with radar imagery would provide a more reliable statistical analysis. The sample size of 39 events for upper air analysis proved adequate, but could also be improved upon with a larger sample size.

### 5.6 Recommendations

The author has three significant recommendations for future ventures. First, expand the sample size of events under study. Now that the NEXRAD network has had an additional year to collect data there are more microburst events with archive level II data available for investigation. Also, a sample of null events should be included for study to compare thunderstorms that are suspected to have produced microbursts to those that did not. This would allow for better quantitative comparisons of the variables studied and would prove very useful in refining the forecasting technique. Additionally, the two regression models highlighted in this study are descriptive in nature and have not been applied to microburst events outside of this sample.

Refinement of these models based upon other microbursts would no doubt improve these models' performances.

The second recommendation is to develop a PC based program that would prompt the user for key thermodynamic and/or radar variables, use the four predictive equations and provide the user with estimates of maximum outflow velocities. This program should be distributed to all weather units supporting operations in the southeastern United States.

The third recommendation is, develop an AWDS based script that will compute and plot  $\theta_e$  profiles for a given sounding. This would provide an operational forecaster with an additional visual tool for forecasting the threat of microbursts for a given day.

This research has pointed out that while microbursts are violent, short lived phenomena, they can be nowcasted as early as 20 minutes under ideal conditions using upper air soundings and NEXRAD data. However, an operational forecaster can not restrict attention to only microbursts, but must also focus on countless other tasks during the challenges of severe weather, and leadtimes for microbursts will most likely fall short of the ideal time requirements. Automation of microburst precursor recognition may help maximize warning leadtime. Until then, recognizing environments most favorable to microbursts and communicating this threat to aviators will go far in preventing another Eastern flight 66 or similar tragedy.

## Appendix A: Acronyms

AETC: Air Education and Training Command

AETC AOS/AOW: Air Education and Training Command's weather directorate

AFCCC: Air Force Combat Climatology Center

AFIT: Air Force Institute of Technology

AGL: Above Ground Level

BRN: Bulk Richardson Number

CAPE: Convective Available Potential Energy

CLAWS: Classify, Locate and Avoid Wind Shear

COHMEX: Cooperative Huntsville Meteorological Experiment

CONUS: Continental United States

dB: decibels, 10 times the log base 10 of the ratio of two quantities with the same units

dBZ: radar reflectivity factor measured in dB and normalized by  $1 \text{ mm}^6 \text{ m}^{-3}$

DDPDA: Damaging Downburst Prediction and Detection Algorithm

hPa: Hectopascal

JAWS: Joint Airport Weather Studies

LI: Lifted Index

MAE: Mean Absolute Error

MIST: Microburst and Severe Thunderstorm

NCDC: National Climatic Data Center

NIMROD: Northern Illinois Meteorological Research on Downbursts

NEXRAD: Next Generation Radar, also known as WSR-88D

NSSL: National Severe Storms Laboratory

OSF: Operational Support Facility

**PAM: Portable Automated Mesonet**

**PUP: Principle User Position**

**RADS: Radar Algorithm and Display System**

**RDA: Radar Data Acquisition**

**RMSE: Root Mean Square Error**

**SMRP: Satellite and Mesometeorology Research Project**

**TDWR: Terminal Doppler Weather Radar**

**UTC: Universal Time Coordinate, also known as Zulu time**

**VIL: Vertically Integrated Liquid**

**WATADS: Weather Algorithm Testing and Display System**

**WINDEX: Wind Index**

**WSR-88D: Weather Surveillance Radar 88 Doppler, also known as NEXRAD**

### Appendix B: Wakimoto Screening Criteria

Wakimoto and Fujita applied the following screening criteria to determine the occurrence of a microburst using the mesoscale observation network during projects NIMROD, JAWS, and MIST.

1. Wind Peak  $\geq 10 \text{ m s}^{-1}$
2. Wind Peak  $\geq W_+ + 5 \text{ m s}^{-1}$
3. Wind Peak  $\geq W_- + 5 \text{ m s}^{-1}$
4. Wind Peak  $\geq 125\%$  of  $W_+$
5. Wind Peak  $\geq 125\%$  of  $W_-$
6.  $W_+ \leq 150\%$  of  $W_-$

where

$W_+$  is the average wind for the 5 minute period starting 7 minutes before to 2 minutes before the wind peak.

$W_-$  is the average wind for the 5 minute period starting 2 minutes after to 7 minutes after the wind peak.

Appendix C: Example Weather Maps

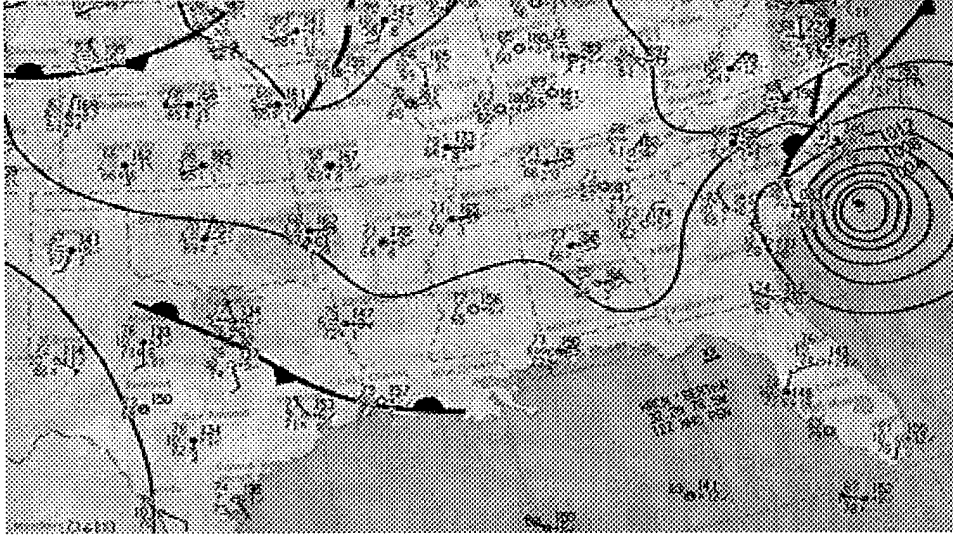


**Figure 35. Microburst in Charleston Discounted Due to Hurricane Bertha.**

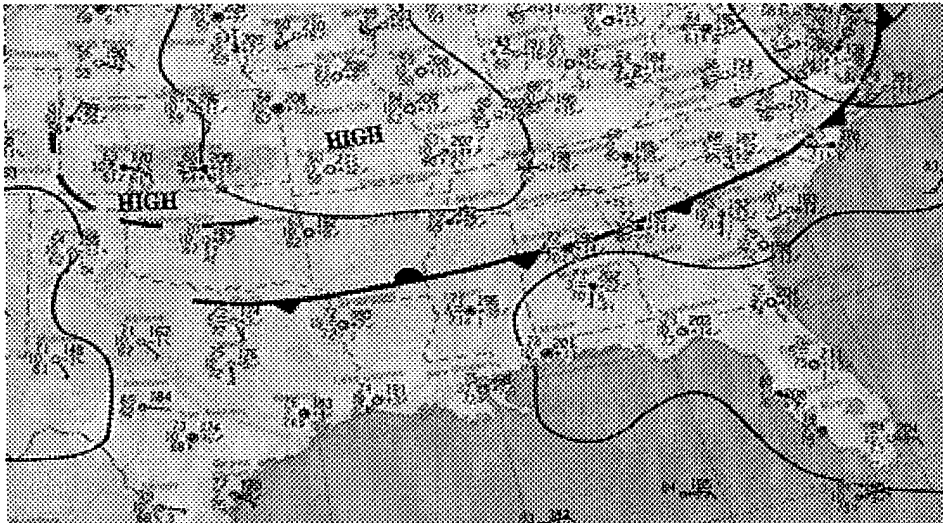


**Figure 36. Microburst in Birmingham Discounted Due to Cold Front.**

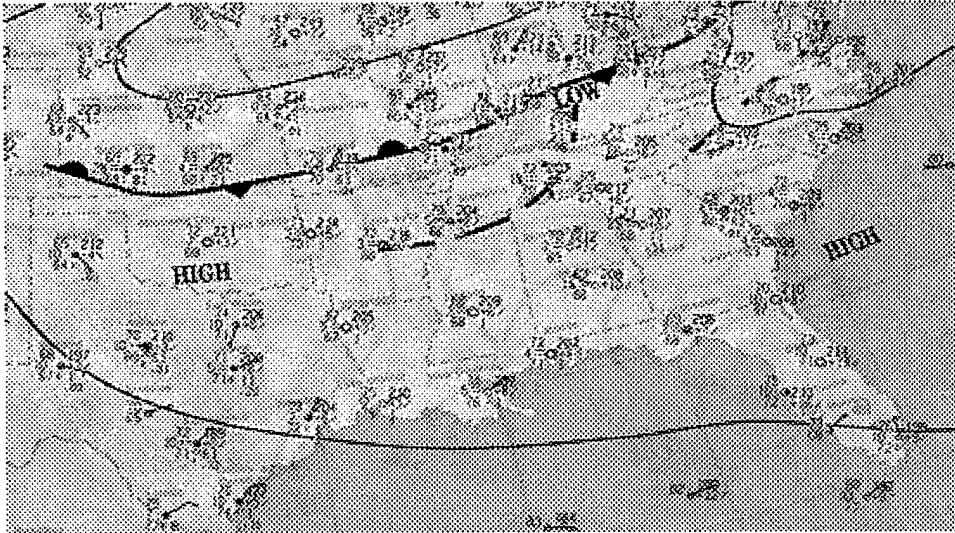


**Figure 37. Surface Map Depicting No Synoptic Features in the Southeast and Favorable to  
Airmass Thunderstorms.**



## Appendix D: Fortran Program READ

\*23456789012345678901234567890123456789012345678901234567890123456789012

\*

\* CAPT J. BRYAN MACKEY, GM-98M

\* Air Force Institute of Technology

\*

\* This is the program read, written in FORTRAN 77. This program reads

\* in raw upper air sounding code formatted so that the first line of

\* data contains the following: numeric ICAO designator, year, month,

\* date, time (UTC), type of sounding, and number of levels sampled.

\* Each line after the first line contains the following information:

\* pressure (mb), height (meters), temperature (Kelvin), dew point

\* depression (Kelvin), wind direction (magnetic degrees), and wind speed

\* (meters per second), for only one sampled level. Once the data is

\* read in pressure, temperature, dew point depression, and wind speed

\* are converted to real numbers. Following this conversion pressure,

\* temperature, wind direction, wind speed, and height are checked to

\* see if those data are available for that particular level. If the

\* data are not available then an average value is entered. Using these

\* variables the following are computed for each level: vapor pressure,

\* mixing ratio, potential temperature, and equivalent potential

\* temperature. Computations of equivalent potential temperature are made

\* using the definition from the Glossary of Meteorology. An output file

\* is then created labeled as xxxXXXXXXaaout.txt, where xxx is the 3 letter

\* station identifier where the sounding took place, XXXXXX is the year,

\* month, date of the sounding and aa is the hour of the sounding.

\*

\* Units of constants and variables used.

\* pnot, the standard pressure = 1000 mb

\* R, the gas constant for dry air = 287 J/kg K

\* cp, the specific heat of dry air at constant pressure = 1004 J/kg K

\* latent, the latent heat of vaporization of water at 0 C = 2.5E6 J/kg

\* pres(count) and rpres(count), pressure at specified level = mb

\* hgt(count), height of pressure level = meters

\* dwdep(count) and rdwdep(count), dew point depression at specified

\* level = K

\* temp(count) and rtemp(count), temperature at specified level = K

\* wspd(count) and rwspd(count), wind speed at specified level = m/s

\* wdir(count), wind direction at specified level = degrees

\* vapor(count), vapor pressure at specified level = mb

\* mixrat(count), mixing ratio at specified level = kg/kg

\* theta(count), potential temperature at specified level = K

\* thetae(count), equivalent potential temperature at specified level = K

\* tdd(count), dew point temperature at specified level = K

\*

program read

real a, b, c, d, l, m, n, o, p, pnot, R, cp, latent

```

parameter (maxlvl=90, a=23.832241, b=5.02808, c=1.3816E-7)
parameter (d=11.334, l=0.0303998, m=8.1328E-3, n=3.49149)
parameter (o=1302.884, p=2949.076, pnot=1000.0, R=287.0)
parameter (cp=1004.0, latent=2.5E6)
character*13 infile
character*11 outfile
character*2 yr,mo,dy,hr
character*3 staid
character*19 inputfile
character*20 outputfile
integer icao, year, month, date, time, pibol, levels, count
integer pind(maxlvl), pres(maxlvl), hind(maxlvl), hgt(maxlvl)
integer temp(maxlvl), dwdep(maxlvl), wdir(maxlvl), wspd(maxlvl)
real rpres(maxlvl), rtemp(maxlvl), rdwdep(maxlvl), rwspd(maxlvl)
real vapor(maxlvl), mixrat(maxlvl), theta(maxlvl), thetae(maxlvl)
real tdd(maxlvl)
10 format (i6,3i2,i4,i3,i5)
15 format (i1,i7,i1,i7,4i4)
20 format (f6.1,1x,i5,1x,f5.1,1x,f5.1,1x,f4.1,1x,i3,1x,f4.1,1x,f5.2,1x,
  $f7.4,1x,f5.1,1x,f5.1)
25 format (i6,3x,i2,1x,i2,1x,i2,1x,i4,1x,i3)
30 format (a3)
35 format (a10)
40 format (a2)
*
* Prompt the user to enter the station id and year, month, date, and
* time of the sounding. This is used to name the input and output
* files.
*
  write (*,*) 'Enter the three letter station identifier'
  read (*,fmt=30) staid
  write (*,*) 'Enter the two digit year of the sounding'
  read (*,fmt=40) yr
  write (*,*) 'Enter the two digit month of the sounding'
  read (*,fmt=40) mo
  write (*,*) 'Enter the two digit date of the sounding'
  read (*,fmt=40) dy
  write (*,*) 'Enter the two digit hour of the sounding'
  read (*,fmt=40) hr
  infile=staid//ua//yr//mo//dy//hr
  inputfile='.///infile//.txt'
  outfile=staid//yr//mo//dy//hr
  outputfile='.///outfile//out.txt'
  open (100,file=inputfile,status='old')
  open (110,file=outputfile,status='unknown')
*
* Read in the first line of data containing the ICAO, DTG, sounding
* type, and number of data levels in the sounding.
*

```

```

    read (100,10) icao,year,month,date,time,pibol,levels
*
* Initialize all arrays to zero.
*
    do 200 count=1,maxlvl
        pind(count)=0
        pres(count)=0
        hind(count)=0
        hgt(count)=0
        temp(count)=0
        dwdep(count)=0
        wdir(count)=0
        wspd(count)=0
        rpres(count)=0.0
        rtemp(count)=0.0
        rdwdep(count)=0.0
        rwspd(count)=0.0
        tdd(count)=0.0
        vapor(count)=0.0
        mixrat(count)=0.0
        theta(count)=0.0
        thetae(count)=0.0
    200 continue
        levels=levels-2
*
* Read in the rest of the data from the levels available.
*
    do 220 count=1,levels
        read (unit=100,fmt=15) pind(count),pres(count), hind(count),
$      hgt(count),temp(count),dwdep(count),wdir(count),
$      wspd(count)
        if (((pind(count).eq.1).or.(pind(count).eq.2)).or.
$(pind(count).eq.9).or.(pind(count).eq.0))) then
            else
                write(*,*) 'Data file is not formatted correctly,
$please check the file for format.'
            endif
    220 continue
*
* Convert pressure, temperature, dew point depression, and wind speed
* to real values.
*
    do 230 count=1,levels
        rpres(count)=float(pres(count))*0.1
        rtemp(count)=float(temp(count))*0.1
        rdwdep(count)=float(dwdep(count))*0.1
        rwspd(count)=float(wspd(count))*0.1
    230 continue
*

```

\* Replace all unknown variables, those labeled as 9999, with an average  
 \* value using the subroutine smooth. Compute the saturation vapor pressure  
 \* using the Goff-Gratch formula and mixing ratio for each level. Next,  
 \* compute the potential temperature and equivalent potential temperature.  
 \* Lastly, write the output to the designated xxxXXXXXXaout.txt  
 \* file.

```

*
do 240 count=1,levels
  if (rtemp(count).gt.900.0) then
    call smooth(rtemp(count-1), rtemp(count), rtemp(count+1),
$ rtemp(count+2), rtemp(count+3), rtemp(count+4), rtemp(count+5))
  endif
  if (rdwdep(count).gt.900.0) then
    call smooth(rdwdep(count-1), rdwdep(count), rdwdep(count+1),
$ rdwdep(count+2), rdwdep(count+3), rdwdep(count+4),
$ rdwdep(count+5))
  endif
  if (float(wdir(count)).gt.900.0) then
    wdir(count)=wdir(count-1)
  endif
  if (rwspd(count).gt.900.0) then
    call smooth(rwspd(count-1), rwspd(count), rwspd(count+1),
$ rwspd(count+2), rwspd(count+3), rwspd(count+4), rwspd(count+5))
  endif
  tdd(count)=rtemp(count)-rdwdep(count)

```

\*  
 \* Use Goff-Gratch equation to solve for vapor pressure at each level.

```

*
  vapor(count)=10**(a-b*log10(tdd(count))-
$c*10**(d-l*tdd(count))+m*10**(n-o/tdd(count))-p/tdd(count))

```

\*  
 \* Solve for mixing ratio at each level.

```

*
  mixrat(count)=0.622*(vapor(count)/(rpres(count)-vapor(count)))

```

\*  
 \* Solve for potential temperature and equivalent potential temperature.

```

*
  theta(count)=rtemp(count)*(pnot/rpres(count))**(R/cp)
  thetae(count)=theta(count)*exp((latent*mixrat(count))/
$(cp*rtemp(count)))
  write (unit=110,fmt=20) rpres(count),hgt(count),rtemp(count),
$ tdd(count),rdwdep(count),wdir(count),rwspd(count),
$ vapor(count),mixrat(count), theta(count), thetae(count)
240 continue
  write (*,*) 'The following file has been written ',outputfile
  stop
end

```

\*  
 \* Once the output file has been created it will be converted to a DOS

\* file with the pm extension using the unix2dos command as follows:

\* unix2dos xxxXXXXXXaaout.txt filename.pm.

\*

\*

\*23456789012345678901234567890123456789012345678901234567890123456789012

\*

\* This subroutine, called smooth, is used to correct for missing  
\* temperature, dew point depression and wind speed values. This is  
\* accomplished by taking the closest known values for the respective  
\* variables and averaging these two to determine an estimate for the  
\* unknown value.

\*

```
subroutine smooth(prev, currnt, first, second, third, fourth,  
$fifth)
```

```
real prev,currnt,first,second,third,fourth,fifth
```

```
real top,bottom,mean
```

```
bottom=prev
```

```
if (first .lt. 900.0) then
```

```
    top=first
```

```
elseif (second .lt. 900.0) then
```

```
    top=second
```

```
elseif (third .lt. 900.0) then
```

```
    top=third
```

```
elseif (fourth .lt. 900.0) then
```

```
    top=fourth
```

```
else
```

```
    top=fifth
```

```
endif
```

```
if (top .gt. 500.0) then
```

```
write (*,*) 'Too many unknown values.'
```

```
endif
```

```
mean=(top+bottom)/2.0
```

```
currnt=mean
```

```
return
```

```
end
```

## Appendix E: Radar Worksheet

### Radar Observations

Time (Z)/ Date/ ICAO/ RDA	21:21 8/4/95 BHM (BMX)	22:30 6/16/97 BHM (BMX)
Max dBZ (dBZ)	58	57
Time of maximum dBZ (Z)	21:11	22:21
Max height central core (meters)	3657	4572
Time of core maximum height (Z)	21:16	22:26
Descent rate core (m min <sup>-1</sup> )	61	244
Time of core impact (Z)	21:16	22:31
Height of max CONV (meters)	2621	2164
Time of max conv (Z)	21:11	22:16
Max in CONV velocity (m s <sup>-1</sup> )	8.2	8.2
Max out CONV velocity (m s <sup>-1</sup> )	7.7	2.1
CONVERGENCE (s <sup>-1</sup> )	8.44E-03	5.47E-03
Core dist from ICAO (kilometers)	1.1	3.6
ICAO to RDA distance (km)	45.2	45.2
Rotation near cloud base/Time	Yes/21:11	Yes/22:26
Max in ROT velocity (m s <sup>-1</sup> )	2.6	4.1
Max out ROT velocity (m s <sup>-1</sup> )	7.7	1.5
Storm top Divergence (s <sup>-1</sup> )	7.29E-03	None
Reflectivity notch	No	Yes
Height of reflectivity notch (m)	NA	1372
Time of reflectivity notch (Z)	NA	22:21
Max echo TOP (100's ft)	360	430
Max echo top time (Z)	21:06	22:21
Max VIL (kg m <sup>-3</sup> )	23	27
Time of max VIL (Z)	21:11	22:21
Central core aspect ratio	3:8	1:3
Weak echo trench	Yes	No
Height of echo trench (m)	3657	NA
Time of echo trench (Z)	21:16	NA

Time (Z)/ Date/ ICAO/ RDA	19:00 6/14/97 CHS (CLX)	23:45 6/27/97 CHS (CLX)
Max dBZ (dBZ)	54	62
Time of maximum dBZ (Z)	18:21	23:16
Max height central core (meters)	5181	7315
Time of core maximum height (Z)	18:36	23:16
Descent rate core (m min <sup>-1</sup> )	137	250
Time of core impact (Z)	18:46	23:27
Height of max CONV (meters)	3048	4877
Time of max conv (Z)	18:36	23:21
Max in CONV velocity (m s <sup>-1</sup> )	4.1	7.7
Max out CONV velocity (m s <sup>-1</sup> )	3.6	7.2
CONVERGENCE (s <sup>-1</sup> )	1.64E-03	5.28E-03
Core dist from ICAO (kilometers)	30.2	22.4
ICAO to RDA distance (km)	123	123
Rotation near cloud base/Time	Yes (Anticyclonic)/18:31	Yes/23:21
Max in ROT velocity (m s <sup>-1</sup> )	9.3	7.7
Max out ROT velocity (m s <sup>-1</sup> )	2.1	3.6
Storm top Divergence (s <sup>-1</sup> )	2.20E-03	3.13E-03
Reflectivity notch	No	Yes
Height of reflectivity notch (m)	NA	4938
Time of reflectivity notch (Z)	NA	23:27
Max echo TOP (100's ft)	399	490
Max echo top time (Z)	18:31	23:16
Max VIL (kg m <sup>-3</sup> )	12	45
Time of max VIL (Z)	18:21	22:32
Central core aspect ratio	2:6	6:15
Weak echo trench	Yes	No
Height of echo trench (m)	4877	NA
Time of echo trench (Z)	18:41	NA

Time (Z)/ Date/ ICAO/ RDA	23:00 6/3/97 CHS (CLX)	23:03 8/24/96 ATL (FFC)
Max dBZ (dBZ)	60	62
Time of maximum dBZ (Z)	22:30	22:32
Max height central core (meters)	7010	8839
Time of core maximum height (Z)	22:25	22:32
Descent rate core (m min <sup>-1</sup> )	162	177
Time of core impact (Z)	22:55	22:50
Height of max CONV (meters)	3749	1494
Time of max conv (Z)	22:30	22:38
Max in CONV velocity (m s <sup>-1</sup> )	4.6	2.1
Max out CONV velocity (m s <sup>-1</sup> )	4.1	2.6
CONVERGENCE (s <sup>-1</sup> )	4.62E-03	1.66E-03
Core dist from ICAO (kilometers)	8.3	4.5
ICAO to RDA distance (km)	123	35.9
Rotation near cloud base/Time	Yes/22:19	Yes/22:32
Max in ROT velocity (m s <sup>-1</sup> )	7.7	2.1
Max out ROT velocity (m s <sup>-1</sup> )	6.2	1.5
Storm top Divergence (s <sup>-1</sup> )	3.16E-03	2.01E-03
Reflectivity notch	No	Yes
Height of reflectivity notch (m)	NA	1341
Time of reflectivity notch (Z)	NA	22:38
Max echo TOP (100's ft)	380	420
Max echo top time (Z)	2230	22:38
Max VIL (kg m <sup>-3</sup> )	39	45
Time of max VIL (Z)	22:35	22:44
Central core aspect ratio	3:5	7:13
Weak echo trench	Yes	Yes
Height of echo trench (m)	5486	4572
Time of echo trench (Z)	22:19	22:44



Time (Z)/ Date/ ICAO/RDA	18:22 6/23/97 MEI (JAN)	18:46 7/11/97 MEI (JAN)
Max dBZ (dBZ)	55	53
Time of maximum dBZ (Z)	17:50	18:25
Max height central core (meters)	7010	8534
Time of core maximum height (Z)	17:50	18:30
Descent rate core (m min <sup>-1</sup> )	204	320
Time of core impact (Z)	18:14	18:45
Height of max CONV (meters)	NA	1859
Time of max conv (Z)	NA	18:30
Max in CONV velocity (m s <sup>-1</sup> )	NA	5.7
Max out CONV velocity (m s <sup>-1</sup> )	NA	4.1
CONVERGENCE (s <sup>-1</sup> )	NA	2.97E-03
Core dist from ICAO (kilometers)	12.9	21.5
ICAO to RDA distance (km)	146.7	146.7
Rotation near cloud base/Time	NA	NA
Max in ROT velocity (m s <sup>-1</sup> )	NA	NA
Max out ROT velocity (m s <sup>-1</sup> )	NA	NA
Storm top Divergence (s <sup>-1</sup> )	8.44E-03	4.22E-03
Reflectivity notch	Yes	No
Height of reflectivity notch (m)	4663	NA
Time of reflectivity notch (Z)	17:50	NA
Max echo TOP (100's ft)	500	460
Max echo top time (Z)	17:56	18:35
Max VIL (kg m <sup>-2</sup> )	25	17
Time of max VIL (Z)	18:06	1835
Central core aspect ratio	3:5	3:7
Weak echo trench	Yes	No
Height of echo trench (m)	4500	NA
Time of echo trench (Z)	18:02	NA

Time (Z)/ Date/ ICAO/ RDA	01:00 6/28/97 GWO (JAN)	22:14 8/19/95 NIP (JAX)
Max dBZ (dBZ)	61	47
Time of maximum dBZ (Z)	0:46	21:50
Max height central core (meters)	9754	2743
Time of core maximum height (Z)	0:46	21:50
Descent rate core (m min <sup>-1</sup> )	191	66
Time of core impact (Z)	0:58	22:02
Height of max CONV (meters)	2134	5120
Time of max conv (Z)	0:41	22:02
Max in CONV velocity (m s <sup>-1</sup> )	4.1	2.1
Max out CONV velocity (m s <sup>-1</sup> )	2.6	2.6
CONVERGENCE (s <sup>-1</sup> )	4.74E-03	2.00E-03
Core dist from ICAO (kilometers)	3.2	4.5
ICAO to RDA distance (km)	131.1	61.7
Rotation near cloud base/Time	NA	No
Max in ROT velocity (m s <sup>-1</sup> )	NA	NA
Max out ROT velocity (m s <sup>-1</sup> )	NA	NA
Storm top Divergence (s <sup>-1</sup> )	2.60E-03	2.03E-03
Reflectivity notch	No	No
Height of reflectivity notch (m)	NA	NA
Time of reflectivity notch (Z)	NA	NA
Max echo TOP (100's ft)	460	377
Max echo top time (Z)	0:46	21:56
Max VIL (kg m <sup>-2</sup> )	22	5
Time of max VIL (Z)	0:35	21:56
Central core aspect ratio	6:14	4:5
Weak echo trench	No	No
Height of echo trench (m)	NA	NA
Time of echo trench (Z)	NA	NA

Time (Z)/ Date/ ICAO/RDA	22:00 6/22/97 NZC (JAX)	16:16 7/8/96 MCN (JGX)
Max dBZ (dBZ)	59	55
Time of maximum dBZ (Z)	21:52	15:53
Max height central core (meters)	6400	3962
Time of core maximum height (Z)	21:46	15:53
Descent rate core (m min <sup>-1</sup> )	85	140
Time of core impact (Z)	21:56	15:59
Height of max CONV (meters)	884	2012
Time of max conv (Z)	21:40	16:11
Max in CONV velocity (m s <sup>-1</sup> )	3.1	1
Max out CONV velocity (m s <sup>-1</sup> )	5.1	4.1
CONVERGENCE (s <sup>-1</sup> )	4.36E-03	2.17E-03
Core dist from ICAO (kilometers)	10.7	5
ICAO to RDA distance (km)	30.3	31.9
Rotation near cloud base/Time	Yes/21:40	Yes/15:59
Max in ROT velocity (m s <sup>-1</sup> )	3.1	2.5
Max out ROT velocity (m s <sup>-1</sup> )	5.1	3.1
Storm top Divergence (s <sup>-1</sup> )	5.74E-03	1.65E-03
Reflectivity notch	No	Yes
Height of reflectivity notch (m)	NA	1737
Time of reflectivity notch (Z)	NA	16:05
Max echo TOP (100's ft)	360	315
Max echo top time (Z)	21:46	16:05
Max VIL (kg m <sup>-2</sup> )	24	18
Time of max VIL (Z)	21:46	15:59
Central core aspect ratio	1:2	4:9
Weak echo trench	Yes	No
Height of echo trench (m)	5486	NA
Time of echo trench (Z)	21:40	NA

Time (Z)/ Date/ ICAO/RDA	20:00 8/3/95 WRB (JGX)	19:00 6/13/96 NSE (MOB)
Max dBZ (dBZ)	53	50
Time of maximum dBZ (Z)	19:35	18:39
Max height central core (meters)	2743	2134
Time of core maximum height (Z)	19:35	18:39
Descent rate core (m min <sup>-1</sup> )	168	165
Time of core impact (Z)	19:40	18:45
Height of max CONV (meters)	2012	3719
Time of max conv (Z)	19:50	18:39
Max in CONV velocity (m s <sup>-1</sup> )	7.7	3.1
Max out CONV velocity (m s <sup>-1</sup> )	2.1	2.1
CONVERGENCE (s <sup>-1</sup> )	5.21E-03	1.84E-03
Core dist from ICAO (kilometers)	2.8	21.9
ICAO to RDA distance (km)	29.8	142.4
Rotation near cloud base/Time	Yes/15:59	NA
Max in ROT velocity (m s <sup>-1</sup> )	2.6	NA
Max out ROT velocity (m s <sup>-1</sup> )	10.3	NA
Storm top Divergence (s <sup>-1</sup> )	3.82E-03	NA Range Folding
Reflectivity notch	No	No
Height of reflectivity notch (m)	NA	NA
Time of reflectivity notch (Z)	NA	NA
Max echo TOP (100's ft)	232	430
Max echo top time (Z)	20:00	18:39
Max VIL (kg m <sup>-3</sup> )	17	12
Time of max VIL (Z)	19:50	18:39
Central core aspect ratio	3:4	1:1
Weak echo trench	No	No
Height of echo trench (m)	NA	NA
Time of echo trench (Z)	NA	NA

Time (Z)/ Date/ ICAO/ RDA	20:00 6/13/97 NSE (MOB)
Max dBZ (dBZ)	59
Time of maximum dBZ (Z)	19:38
Max height central core (meters)	7620
Time of core maximum height (Z)	19:28
Descent rate core (m min <sup>-1</sup> )	183
Time of core impact (Z)	19:58
Height of max CONV (meters)	1900
Time of max conv (Z)	19:33
Max in CONV velocity (m s <sup>-1</sup> )	2.6
Max out CONV velocity (m s <sup>-1</sup> )	6.7
CONVERGENCE (s <sup>-1</sup> )	2.47E-03
Core dist from ICAO (kilometers)	19
ICAO to RDA distance (km)	142.4
Rotation near cloud base/Time	NA
Max in ROT velocity (m s <sup>-1</sup> )	NA
Max out ROT velocity (m s <sup>-1</sup> )	NA
Storm top Divergence (s <sup>-1</sup> )	NA
Reflectivity notch	Yes
Height of reflectivity notch (m)	4968
Time of reflectivity notch (Z)	19:43
Max echo TOP (100's ft)	360
Max echo top time (Z)	19:38
Max VIL (kg m <sup>-3</sup> )	36
Time of max VIL (Z)	19:38
Central core aspect ratio	8:11
Weak echo trench	No
Height of echo trench (m)	NA
Time of echo trench (Z)	NA

Appendix F: Upper Air Worksheet

	23:33 7/10/94 ATL	18:31 7/17/94 BIX	16:25 7/22/94 BIX
Sounding Time/Location	AHN 1200Z	LIX 1200Z	LIX 1200Z
Height of Melting level (meters)	4260	4500	3350
Theta-e min (Kelvin)	321.7	320.9	310
Height of Theta-e min (meters)	2134	4404	3658
Delta Theta-e (Kelvin)	18	23.3	45.6
CAPE (J/kg)	113.4	1115.3	1866.4
BRN	3.75	312.34	341.59
Lifted Index	0.6	-3.6	-3.1
Depth of shear layer (meters)	1829	610	914
Sounding to ICAO (kilometers)	123	130	130
Top shear less bottom $V_d$ (m/s)	9.8	5.6	8.2
Shear layer wind avg $V_{avg}$ (m/s)	8.4	3.7	5.6
Lapse rate to 0° isotherm (deg/km)	5.13	4.68	8.1
Ql Mean mix ratio lowest 1km (g/kg)	13.7	16.2	17.3
Qm Mix ratio at zero isotherm (g/kg)	5	2	3.4
L Max mix ratio (g/kg)	16.7	17.6	21
Height of transition level (meters)	1470	859	610

	14:36 6/29/94 CBM	20:00 6/30/94 CBM	13:00 7/25/94 CBM
Sounding Time/Location	JAN 1200Z	JAN 1200Z	JAN 1200Z
Height of Melting level (meters)	4000	4400	4230
Theta-e min (Kelvin)	324.6	314.3	326.6
Height of Theta-e min (meters)	3658	2438	2134
Delta Theta-e (Kelvin)	34.6	37.1	22.4
CAPE (J/kg)	3225.4	1825.5	2852.2
BRN	327.49	43.67	18495.02
Lifted Index	-7.9	-2.6	-5.1
Depth of shear layer (meters)	312	914	305
Sounding to ICAO (kilometers)	233	233	233
Top shear less bottom $V_a$ (m/s)	8.8	6.1	2.9
Shear layer wind avg $V_{avg}$ (m/s)	5.8	4.3	7.2
Lapse rate to $0^\circ$ isotherm (deg/km)	6.58	4.69	5.77
Ql Mean mix ratio lowest 1km (g/kg)	19	16.6	16.2
Qm Mix ratio at zero isotherm (g/kg)	4.9	1.5	5
L Max mix ratio (g/kg)	20.6	18.6	17.7
Height of transition level (meters)	312	610	610

	19:28 6/29/94 CSG	21:00 7/15/94 GWO	20:38 7/1/94 MEI
Sounding Time/Location	AHN 1200Z	JAN 1200Z	JAN 1200Z
Height of Melting level (meters)	4200	3900	4150
Theta-e min (Kelvin)	319.7	314.6	315.9
Height of Theta-e min (meters)	4267	1483	3658
Delta Theta-e (Kelvin)	27.9	32.6	31.4
CAPE (J/kg)	2693.4	307.3	2633
BRN	27.35	13.85	165.65
Lifted Index	-7.9	-1.4	-8.4
Depth of shear layer (meters)	4267	610	1846
Sounding to ICAO (kilometers)	239	131.1	196
Top shear less bottom $V_d$ (m/s)	14	9.3	7.2
Shear layer wind avg $V_{avg}$ (m/s)	9.4	8.4	4
Lapse rate to 0° isotherm (deg/km)	4.23	5.86	5.88
Ql Mean mix ratio lowest 1km (g/kg)	16.7	14.4	15.9
Qm Mix ratio at zero isotherm (g/kg)	2.7	6	1.4
L Max mix ratio (g/kg)	17.7	17.9	18
Height of transition level (meters)	914	622	1420



	22:30 7/24/94 MEI	21:21 8/4/95 BHM	3:16 6/28/95 CHS
Sounding Time/Location	JAN 1200Z	BMX 1200Z	CHS 0000Z
Height of Melting level (meters)	4700	4800	4300
Theta-e min (Kelvin)	319.4	333.3	321.1
Height of Theta-e min (meters)	3913	3672	4291
Delta Theta-e (Kelvin)	27	17.8	33.5
CAPE (J/kg)	1849.7	150.8	2707.2
BRN	74.24	0.69	67.9
Lifted Index	-2.5	1.5	-6.5
Depth of shear layer (meters)	305	1527	305
Sounding to ICAO (kilometers)	196	43	6
Top shear less bottom $V_d$ (m/s)	3.6	15.2	0.6
Shear layer wind avg $V_{avg}$ (m/s)	1.6	17.6	6.3
Lapse rate to 0° isotherm (deg/km)	4.75	5.34	7.08
Ql Mean mix ratio lowest 1km (g/kg)	15	16.3	17.1
Qm Mix ratio at zero isotherm (g/kg)	3.2	6.5	2.2
L Max mix ratio (g/kg)	18	18.9	19.4
Height of transition level (meters)	610	1799	610

	21:00 6/2/95 CSG	22:37 6/11/95 CSG	23:00 8/15/95 MGM
Sounding Time/Location	FFC 1200Z	FFC 1200Z	BMX 1200Z
Height of Melting level (meters)	3900	4400	5000
Theta-e min (Kelvin)	321.7	321.9	323.6
Height of Theta-e min (meters)	4688	6096	3641
Delta Theta-e (Kelvin)	21.3	14.4	50.7
CAPE (J/kg)	2689.9	561.2	4272.1
BRN	28.35	32.52	189.42
Lifted Index	-6.8	-0.7	-7.1
Depth of shear layer (meters)	3148	610	305
Sounding to ICAO (kilometers)	137	137	106
Top shear less bottom $V_d$ (m/s)	13.4	6.7	3.6
Shear layer wind avg $V_{avg}$ (m/s)	11.8	4.2	3.4
Lapse rate to $0^\circ$ isotherm (deg/km)	6.37	5.55	5.97
Ql Mean mix ratio lowest 1km (g/kg)	15.3	13.1	20.5
Qm Mix ratio at zero isotherm (g/kg)	5	4.9	3.2
L Max mix ratio (g/kg)	16.1	15	25.7
Height of transition level (meters)	1219	1219	610

	4:00 8/20/95 MXF	20:20 7/7/95 NIP	22:14 8/19/95 NIP
Sounding Time/Location	BMX 0000Z	JAX 1200Z	JAX 1200Z
Height of Melting level (meters)	4900	4700	4900
Theta-e min (Kelvin)	327	320.7	333
Height of Theta-e min (meters)	4176	3855	3200
Delta Theta-e (Kelvin)	26.4	30.9	23.1
CAPE (J/kg)	692.5	1873.9	2491
BRN	302.58	220.09	200.43
Lifted Index	-3	-5.6	-5.7
Depth of shear layer (meters)	1839	305	123
Sounding to ICAO (kilometers)	89	61	61
Top shear less bottom $V_a$ (m/s)	2.6	4.5	0.5
Shear layer wind avg $V_{avg}$ (m/s)	4.1	1.9	1.3
Lapse rate to 0° isotherm (deg/km)	7.44	4.65	5.11
Ql Mean mix ratio lowest 1km (g/kg)	13.7	14.8	19.3
Qm Mix ratio at zero isotherm (g/kg)	2.5	2.6	4.8
L Max mix ratio (g/kg)	16.1	19.7	20.8
Height of transition level (meters)	1227	387	810

	23:03 8/24/96 ATL	20:16 6/24/96 CSG	3:56 7/8/96 HSV
Sounding Time/Location	FFC 1200Z	FFC 1200Z	BMX 0000Z
Height of Melting level (meters)	4300	4300	4630
Theta-e min (Kelvin)	326.6	327.7	332.7
Height of Theta-e min (meters)	3197	4905	4406
Delta Theta-e (Kelvin)	10.5	21	29.7
CAPE (J/kg)	608.3	2609.7	484.9
BRN	302.89	66.16	7.91
Lifted Index	-1.6	-7.5	-3.2
Depth of shear layer (meters)	2134	610	610
Sounding to ICAO (kilometers)	35	137	240.1
Top shear less bottom $V_d$ (m/s)	3.1	8.2	6.8
Shear layer wind avg $V_{avg}$ (m/s)	3	4.1	8.5
Lapse rate to 0° isotherm (deg/km)	4.65	5.01	5.93
Ql Mean mix ratio lowest 1km (g/kg)	12.6	16.5	16.9
Qm Mix ratio at zero isotherm (g/kg)	4.5	5	4.6
L Max mix ratio (g/kg)	14.6	17.5	22.8
Height of transition level (meters)	503	981	1219

	16:16 7/8/96 MCN	20:21 7/17/96 MCN	19:00 6/13/96 NSE
Sounding Time/Location	FFC 1200Z	FFC 1200Z	JAX 1200Z
Height of Melting level (meters)	4600	4600	3800
Theta-e min (Kelvin)	330.2	323	318.2
Height of Theta-e min (meters)	2952	4936	3675
Delta Theta-e (Kelvin)	9.3	23.8	29.4
CAPE (J/kg)	81.3	1033.4	2197.7
BRN	1.66	171.69	4338.46
Lifted Index	3.3	-2.2	-4.4
Depth of shear layer (meters)	1219	2449	305
Sounding to ICAO (kilometers)	146	146	589
Top shear less bottom $V_d$ (m/s)	11.4	5.1	4.6
Shear layer wind avg $V_{avg}$ (m/s)	8.7	3.9	3.8
Lapse rate to 0° isotherm (deg/km)	5.28	4.33	6.01
Ql Mean mix ratio lowest 1km (g/kg)	14.1	15.8	15.2
Qm Mix ratio at zero isotherm (g/kg)	5.6	3.5	3.4
L Max mix ratio (g/kg)	15.6	17.2	18.7
Height of transition level (meters)	1001	683	163

	21:22 8/23/96 WRB	23:07 6/3/97 CHS	19:00 6/14/97 CHS
Sounding Time/Location	FFC 1200Z	CHS 1200Z	CHS 1200Z
Height of Melting level (meters)	4500	3100	4000
Theta-e min (Kelvin)	321.6	315	320.8
Height of Theta-e min (meters)	3000	3560	4782
Delta Theta-e (Kelvin)	16.3	9.7	21.5
CAPE (J/kg)	505.4	1334.6	470.3
BRN	108.95	52.87	32.91
Lifted Index	-2.1	-5.1	-1.7
Depth of shear layer (meters)	1594	749	305
Sounding to ICAO (kilometers)	154	6	6
Top shear less bottom $V_d$ (m/s)	4	6.7	11.4
Shear layer wind avg $V_{avg}$ (m/s)	3.8	5.6	7
Lapse rate to $0^\circ$ isotherm (deg/km)	4.2	6.08	5.71
Ql Mean mix ratio lowest 1km (g/kg)	13.2	11.3	13.6
Qm Mix ratio at zero isotherm (g/kg)	4.1	5.3	4.7
L Max mix ratio (g/kg)	15.7	12.7	17.1
Height of transition level (meters)	456	914	675

	0:31 6/18/97 CHS	23:50 6/27/97 CHS	1:19 6/28/97 GWO
Sounding Time/Location	CHS 1200Z	CHS 1200Z	JAN 0000Z
Height of Melting level (meters)	4100	4100	4400
Theta-e min (Kelvin)	324.1	326.9	328.3
Height of Theta-e min (meters)	4167	3898	2173
Delta Theta-e (Kelvin)	18	12.6	25.5
CAPE (J/kg)	1777.9	1203.1	417.6
BRN	24.43	88.07	58.1
Lifted Index	-4.2	-3.3	-1.1
Depth of shear layer (meters)	305	305	141
Sounding to ICAO (kilometers)	6	6	131
Top shear less bottom $V_d$ (m/s)	15.5	5.2	0
Shear layer wind avg $V_{avg}$ (m/s)	9.9	5.3	1.3
Lapse rate to 0° isotherm (deg/km)	5.57	5.57	7.5
Ql Mean mix ratio lowest 1km (g/kg)	15.6	14.5	16.8
Qm Mix ratio at zero isotherm (g/kg)	5.4	5.4	5.4
L Max mix ratio (g/kg)	17.1	16.4	18.2
Height of transition level (meters)	347	830	831

	21:00 6/13/97 HSV	16:53 6/18/97 MCN	22:17 6/25/97 MCN
Sounding Time/Location	BMX 1200Z	FFC 1200Z	FFC 1200Z
Height of Melting level (meters)	4100	4300	4300
Theta-e min (Kelvin)	316.4	316.7	325.3
Height of Theta-e min (meters)	2455	3062	3207
Delta Theta-e (Kelvin)	26.8	21.9	18.5
CAPE (J/kg)	0	167.4	424
BRN	0	0.5	11.49
Lifted Index	-2.7	1.4	-1.4
Depth of shear layer (meters)	305	914	1219
Sounding to ICAO (kilometers)	240	146	146
Top shear less bottom $V_d$ (m/s)	7.7	14.9	4.1
Shear layer wind avg $V_{avg}$ (m/s)	4.2	12.2	3.4
Lapse rate to 0° isotherm (deg/km)	5.71	4.79	4.77
Ql Mean mix ratio lowest 1km (g/kg)	14.9	12.9	14.3
Qm Mix ratio at zero isotherm (g/kg)	2.1	5.7	4.7
L Max mix ratio (g/kg)	17.6	15.2	16.4
Height of transition level (meters)	1052	783	1133



	18:22 6/23/97 MEI	18:46 7/11/97 MEI	15:10 6/14/97 NIP
Sounding Time/Location	JAN 1200Z	JAN 1200Z	JAX 1200Z
Height of Melting level (meters)	4200	4600	4200
Theta-e min (Kelvin)	314.3	317.8	318.2
Height of Theta-e min (meters)	2173	3785	3550
Delta Theta-e (Kelvin)	32.2	30.8	27.8
CAPE (J/kg)	1288.5	2862.8	45.6
BRN	161.31	216.42	1.38
Lifted Index	-6.1	-6.3	-2.1
Depth of shear layer (meters)	930	928	1858
Sounding to ICAO (kilometers)	196	196	61
Top shear less bottom $V_a$ (m/s)	5.1	0	11.8
Shear layer wind avg $V_{avg}$ (m/s)	2.6	2	14
Lapse rate to $0^\circ$ isotherm (deg/km)	5.57	5.07	5.68
Q1 Mean mix ratio lowest 1km (g/kg)	15.6	16.9	15.9
Qm Mix ratio at zero isotherm (g/kg)	6	5.9	3
L Max mix ratio (g/kg)	18.1	18	18.4
Height of transition level (meters)	621	1247	797

	20:00 6/13/97 NSE	22:00 6/22/97 NZC	19:11 6/27/97 VLD
Sounding Time/Location	JAX 1200Z	JAX 1200Z	TLH 1200Z
Height of Melting level (meters)	4100	4500	4500
Theta-e min (Kelvin)	319.3	319.1	322.5
Height of Theta-e min (meters)	2756	2462	2323
Delta Theta-e (Kelvin)	22.9	27.5	24.5
CAPE (J/kg)	519.5	600.2	837.4
BRN	36.52	337.92	39.72
Lifted Index	-1.3	-2.3	-2.8
Depth of shear layer (meters)	776	3896	305
Sounding to ICAO (kilometers)	589.5	30.3	129
Top shear less bottom $V_d$ (m/s)	10.3	4.6	5.1
Shear layer wind avg $V_{avg}$ (m/s)	8	4.2	2.5
Lapse rate to 0° isotherm (deg/km)	5.57	4.63	4.72
Ql Mean mix ratio lowest 1km (g/kg)	15.4	14.2	15.8
Qm Mix ratio at zero isotherm (g/kg)	3.5	3.6	4.3
L Max mix ratio (g/kg)	17.6	18.1	18.1
Height of transition level (meters)	1855	617	319

	17:00 6/18/97 CHS
Sounding Time/Location	CHS 0000Z
Height of Melting level (meters)	4500
Theta-e min (Kelvin)	327.9
Height of Theta-e min (meters)	5161
Delta Theta-e (Kelvin)	25.2
CAPE (J/kg)	
BRN	
Lifted Index	
Depth of shear layer (meters)	305
Sounding to ICAO (kilometers)	6.4
Top shear less bottom $V_d$ (m/s)	3.1
Shear layer wind avg $V_{avg}$ (m/s)	6
Lapse rate to 0° isotherm (deg/km)	5.3
Ql Mean mix ratio lowest 1km (g/kg)	17.3
Qm Mix ratio at zero isotherm (g/kg)	2.2
L Max mix ratio (g/kg)	19.9
Height of transition level (meters)	914

## Bibliography

- Atkins, Nolan T. and Roger M. Wakimoto. "Wet Microburst Activity Over the Southeastern United States: Implications for Forecasting," Weather and Forecasting, 6: 470-482 (December 1991).
- Bertin, John J. and Michael L. Smith. Aerodynamics for Engineers (Second Edition). Englewoods Cliffs, New Jersey: Prentice Hall, 1989.
- Bringi, V. N., Thomas A. Seliga, and Kultegin Aydin. "Hail Detection with a Differential Reflectivity Radar," Science, 225: 1145-1147 (14 September 1984).
- Devore, Jay L. Probability and Statistics for Engineering and the Sciences (Fourth Edition). Cincinnati: Duxbury Press, 1995.
- Eilts, Johnson, and others. "Damaging Downburst Prediction and Detection Algorithm for the WSR-88D," Proceedings of the 18th Conference on Severe Local Storms. 541-546. Boston: American Meteorological Society, 1996.
- Eilts, Michael D. and Susan K. Oakland. "Convergence Aloft as a Precursor to Microbursts," Proceedings of the 24<sup>th</sup> Conference on Radar Meteorology, P9.8. 190-193. American Meteorological Society, 1989.
- Fujita, Theodore T. "Tornadoes and Downbursts in the Context of Generalized Planetary Scales," Journal of the Atmospheric Sciences, 38: 1511-1534 (August 1981).
- The Downburst Microburst and Macroburst. Chicago: University of Chicago Press, 1985.
- Isaminger, M. A. A Preliminary Study of Precursors to Huntsville Microbursts. Lincoln Laboratory Project report: ATC-153, 1988 (AD-A200914).
- Jackson, Paul (Ed.). Jane's All the World's Aircraft, 1995. Alexandria, Virginia: Jane's Information Group Inc., 1995.
- Kingsmill, David E. and Roger M. Wakimoto. "Kinematic, Dynamic, and Thermodynamic Analysis of a Weakly Sheared Severe Thunderstorm over Northern Alabama," Monthly Weather Review, 119: 262-297 (February 1991).
- McCann, Donald W. "WINDEX-A New Index for Forecasting Microburst Potential," Weather and Forecasting, 9: 532-541 (December 1994).
- National Oceanic and Atmospheric Administration. Daily Weather Maps. 1 June 1994 - 31 Aug 1994, 1 June 1995 - 31 Aug 1995, 1 June 1996 - 31 Aug 1996, 1 June 1997 - 31 Aug 1997. Washington: Department of Commerce, 1994-1997.
- National Weather Service, Operations Training Branch. Principles of Weather Radar. OTB Module 1. Norman, Oklahoma: Operational Support Facility, July 1990.

- Ray, Peter S. (Ed.). Mesoscale Meteorology and Forecasting. (Third Edition). Boston: American Meteorological Society, 1993.
- Rinehart, Ronald E. Radar for Meteorologist. (Second Edition). Grand Forks: Knight Printing Company, 1991.
- Roberts, Rita D. and James W. Wilson. "A Proposed Microburst Nowcasting Procedure Using Single-Doppler Radar," Journal of Applied Meteorology, 28: 285-303 (April 1989).
- Rose, Mark A. "Downburst," National Weather Digest, 21:11-17 (September 1996).
- Smith, Travis. National Severe Storms Laboratory, Norman OK. Personal Correspondence. 9 October 1997.
- Srivastava, R. C. "A Model of Intense Downdrafts Driven by the Melting and Evaporation of Precipitation," Journal of the Atmospheric Sciences, 44: 1752-1773 (July 1987).
- Stewart, Stacy R. "Wet Microbursts-Predicting Peak Wind Gusts Associated with Summertime Pulse-Type Thunderstorms," Proceedings of the 18<sup>th</sup> Conference on Severe Local Storms. 324-327. Boston: American Meteorological Society, 1996.
- Wakimoto, Roger M. "Forecasting Dry Microburst Activity Over the High Plains," Monthly Weather Review, 113: 1131-1143 (July 1985).
- and V. N. Bringi. "Dual-Polarization Observations of Microbursts Associated with Intense Convection: the 20 July Storm During the MIST Project," Monthly Weather review, 116: 1521-1539 (August 1988).
- Wilks, Daniel S. Statistical Methods in the Atmospheric Sciences. Boston: Academic Press, 1995.
- Wilson, James W., Rita D. Roberts, Cathy Kessinger, and John McCarthy. "Microburst Wind Structure and Evaluation of Doppler Radar for Airport Wind Shear Detection," Journal of Climate and Applied Meteorology, 23: 898-914 (June 1984).
- Wolfson, Marilyn M. "Understanding and Predicting Microbursts," Proceedings of the 16<sup>th</sup> Conference on Severe Local Storms. 340-351. Kananaskis Park, Canada: American Meteorological Society, 1990.

Vita

Captain J. Bryan Mackey was born on [REDACTED] [REDACTED] [REDACTED]. He graduated from Gardendale High School in Gardendale, Alabama in 1986 and entered Birmingham-Southern College in Birmingham, Alabama. He graduated with a Bachelor of Science degree in Mathematics in May 1990. He received his commission on 2 June 1990 from Detachment 12, Samford University through the Air Force Reserve Officers Training Corps.

His first assignment was at Florida State University in Tallahassee, Florida where he completed the Basic Meteorology Program through the Air Force Institute of Technology Civilian Institute Program. His second assignment was at Altus AFB where he served as wing weather officer to the 340<sup>th</sup> Air Refueling Wing, 443<sup>rd</sup> Airlift Wing, and 97<sup>th</sup> Air Mobility Wing. His third assignment was at Fort Bliss AIN where he served as Regimental Staff Weather Officer to the 3<sup>rd</sup> Armored Cavalry Regiment and flight commander of the weather flight, 12<sup>th</sup> Air Support Operations Squadron. In August 1996, he entered the School of Engineering, Air Force Institute of Technology. His follow-on assignment is to the 334<sup>th</sup> Training Squadron at Keesler AFB.

Captain Mackey is married to the former Sonja Lynn Pitzer of Warner Robbins, Georgia. They have two daughters, Kalyn and Ryan.

Permanent Address: [REDACTED]  
[REDACTED]

REPORT DOCUMENTATION PAGE			Form Approved OMB No. 0704-0188
Public reporting burden for this collection of information is estimated to average 1 hour per response, including the time for reviewing instructions, searching existing data sources, gathering and maintaining the data needed, and completing and reviewing the collection of information. Send comments regarding this burden estimate or any other aspect of this collection of information, including suggestions for reducing this burden, to Washington Headquarters Services, Directorate for Information Operations and Reports, 1215 Jefferson Davis Highway, Suite 1204, Arlington, VA 22202-4302, and to the Office of Management and Budget, Paperwork Reduction Project (0704-0188), Washington, DC 20503.			
1. AGENCY USE ONLY (Leave blank)	2. REPORT DATE March 1998	3. REPORT TYPE AND DATES COVERED Master's Thesis	
4. TITLE AND SUBTITLE FORECASTING WET MICROBURSTS ASSOCIATED WITH SUMMERTIME AIRMASS THUNDERSTORMS OVER THE SOUTHEASTERN UNITED STATES		5. FUNDING NUMBERS	
6. AUTHOR(S) James Bryan Mackey, Captain, USAF			
7. PERFORMING ORGANIZATION NAME(S) AND ADDRESS(ES) Lt Col Cecilia A. Askue caskue@afit.af.mil (937) 255-3636 AFIT/ENP 2950 P Street Building 640 WPAFB OH 45433		8. PERFORMING ORGANIZATION REPORT NUMBER  AFIT/GM/ENP/98M-06	
9. SPONSORING/MONITORING AGENCY NAME(S) AND ADDRESS(ES) Lt Col Larry Becker DSN 487-3700 AETC AOS/AOW 1 F Street Ste 02 Randolph AFB TX 78150-4325		10. SPONSORING/MONITORING AGENCY REPORT NUMBER	
11. SUPPLEMENTARY NOTES			
12a. DISTRIBUTION AVAILABILITY STATEMENT Approved for public release; distribution unlimited		12b. DISTRIBUTION CODE	
13. ABSTRACT (Maximum 200 words) Microbursts are intense downbursts from thunderstorms that affect an area less than 4 km and have a lifespan less than 10 minutes. Wet microbursts are associated with heavy precipitation and are common in the eastern and southeastern part of the country. The greatest threat from microbursts is to low flying aircraft, where the rapid fluctuations in horizontal and vertical airflow create tremendous shear zones. Microbursts have been determined to be the causal factor behind at least three major aircraft accidents resulting in numerous fatalities. Due to the short lifespan of microbursts, they often strike without warning and pose a serious challenge to operational forecasters trying to protect Air Force assets. This thesis seeks to develop a technique to forecast wet microbursts using currently operational technology, including upper air soundings and WSR-88D products. The technique developed is comprised of three distinct phases. First, recognize the potential threat for given environmental conditions. Second, predict the maximum outflow velocities from microbursts using predictive equations. Third, highlight key NEXRAD radar products that demonstrate a strong potential to serve as precursors to microburst formation. Using the technique developed, warning leadtimes on the order of 10 to 20 minutes appear to be reasonable in operational applications.			
14. SUBJECT TERMS wet microbursts, thunderstorms, aviation safety, weather, weather hazards		15. NUMBER OF PAGES 141	
		16. PRICE CODE	
17. SECURITY CLASSIFICATION OF REPORT Unclassified	18. SECURITY CLASSIFICATION OF THIS PAGE Unclassified	19. SECURITY CLASSIFICATION OF ABSTRACT Unclassified	20. LIMITATION OF ABSTRACT UL